Part II

Numerical Results: Heat and Mass Transfer

Chapter 3

Heat Transfer Investigation in 2-D Gas-Solid Fluidized Beds

In this chapter[1], the heat exchanged between the gas-solid flow and a heated cylinder in a 2-D fluidized bed was investigated through the two-fluid granular temperature model. The thermal diffusion was calculated from expressions based on the kinetic theory of granular flows and on the conduction through an emulsion phase. The influence of these expressions on the hydrodynamics and on the heat transfer was studied by conducting 2-D numerical simulations in cartesian coordinates. Heat transfer coefficients obtained from both experiments and numerical simulations compare well, increasing the confidence in the model. In addition, energy dissipative parameters were studied through power spectra densities obtained from pressure drop fluctuations. [2]

[1]This chapter was submitted for publication in the International Journal for Multiphase Flow: J. L. M. A. Gomes, C. C. Pain, C. R. E. de Oliveira, A. J. H. Goddard (2003), *An Evaluation of Two-Fluid Heat Transfer Models for Gas-Solid Fluidized Beds*

[2]Some numerical results shown in this chapter were presented at the First MIT Conference on Computational Fluid and Solid Mechanics held in Cambridge, USA on June 2001 [87].

3.1 Introduction

Fluidization processes are widely used by a great assortment of industries worldwide and represent a trillion dollar industry [13, 4]. They are currently used in separation, classification, drying and mixing of particles, chemical reactions and regeneration processes. Fluidized beds play an important role in the chemical and petrochemical industries and in the production of chemicals such as ethylene, propylene, HDPE, LDPE, LLDPE and benzene. They are also used in power generation from the combustion of coal [14, 15] or biomass gasification as reported by Kehlenbeck *et al.* [16] and by Kinoshita *et al.* [17].

Fluidized beds are perhaps best known for their use in fluid catalytic cracking (FCC) processes, where complex hydrocarbons are broken into simpler molecules in order to increase the quality and quantity of lighter, more desirable products and decrease the amount of residuals. In such processes, the chemical structure of heavier hydrocarbons feedstock is rearranged into lighter fractions, such as gasoline, kerosene, petrochemical feedstock and others, by the action of finely divided catalyst, which is fluidized by the oil vapors. FCC reactions are, indeed, endothermic; they create products with higher heat contents than the reactants and they absorb heat from the environment. However, the spent catalyst can be regenerated through exothermic fluidization processes with air. Thus, the investigation of heat transfer mechanisms in gas-solid flows has received a great deal of attention from the scientific community [29, 8] as the parameters that govern the heat exchange should be optimized. This has provided an extra motivation for the development of several commercial and academic computational fluid dynamics (CFD) codes.

Although the use of fluidized beds in industrial applications dates from the early 20's, the development of zeolites as a more active and selective catalyst for FCC processes in the 60's, boosted the use of bubbling and circulated fluidized beds in order to improve the performance of these processes. Although the hydrodynamics of gas-solid fluidized beds had been exhaustively studied by many researchers, only in the last 10 years could computational resources be fully applied, to the development of numerical techniques that would allow the modelling of such complex systems.

In the literature review performed by Lim *et al.* [13] and Bi *et al.* [88], the hydro-

dynamics related to the granular flow has been extensively studied by a number of researchers, including some works [5, 38, 41, 8] focusing on bubbling regime, dilute flows and kinetic theory. In addition, the thermal energy generation and diffusion throughout the bed has been widely researched, both experimentally and theoretically. Yates [89] produced a noteworthy review of the most important works concerning the influence of temperature and pressure on the hydrodynamics of gas-solid fluidized beds. Lettieri *et al.* [90, 91] investigated the influence of high temperature profiles on FCC particles during a fluidization process. In addition, they studied bed expansion by using a drag force correlation proposed by Foscolo & Gibilaro [92]. Molerus *et al.* [61] investigated the global heat transfer due to convective mechanisms. They proposed a set of empirical correlations for the global heat transfer coefficient as a function of the Archimedes number, and for the radiative heat transfer coefficient in granular flows, i.e., when the temperature rises beyond 700 ^{o}C. Wirth [12] investigated experimentally the heat transfer between the walls and dilute flow. Sundaresan & Clark [62] measured the heat transfer coefficient to granular flows from a single cylinder and from a bank of heated cylinders. They investigated the presence of a stagnant zone in the top region of the cylinders due to the low superficial velocities. Gunn [56] measured the interphase heat transfer in fixed and fluidized beds and suggested an empirical correlation to evaluate the Nusselt number in such beds.

The numerical modelling of the thermal energy transport equation has not received the same attention as the study of either the modelling of the momentum and mass balances or the theoretical and experimental issues related to heat transfer. Nevertheless, a few works related to the modelling of heat transfer in circulating and bubbling fluidized beds have been performed by a number of researchers. Kuipers *et al.* [63] and Syamlal & Gidaspow [86] investigated numerically the heat transferred from a heated wall into the bed, and compared some of the results with experiments and with the penetration theory. In addition, the influence of the bubble wakes on thermal energy transfer was also studied. In both works, the influence of particle collisions on the heat transfer, and in particular on the diffusion coefficient were neglected. However, Schmidt and Renz [34, 35] used correlations derived from the kinetic theory to calculate the effective thermal conductivity. These correlations were developed by Natarajan & Hunt [68] (see also [66, 64]) using

the analogy of random motion of gas molecules and inelastic particle collisions in dense granular flows. Schmidt and Renz simulated a lab-scale fluidized bed, in the bubbling regime, with a heated cylinder. They performed a few numerical simulations, in a commercial code, and calculated the heat transfer coefficients. Their results were compared with experimental results due to Sundaresan & Clark [62]. In addition, some simulations using a standard correlation for the effective thermal conductivity, as used by Kuipers *et al.* [63], were also performed and the results were compared with those obtained using a kinetic-based correlation.

In this work, the two-fluid model was used to describe the fluid flow in gas-solid fluidized beds. In order to investigate the influence of the effective conductivity model on the hydrodynamics, several 2-D simulations were performed using three models: a classical [63, 86] model and two models based on kinetic theory [68, 66]. The heat transfer coefficients obtained from these models were compared with experimental results. In addition, the influence of the kinetic energy dissipative parameters on the hydrodynamics was also investigated, by performing a set of numerical simulations and analyzing the power spectra of voidage fluctuations in several locations of the domain.

3.2 Existing Heat Transfer Models

Several models have been proposed in the literature to explain different aspects of the heat transfer mechanisms in gas-solid and in liquid fluidized beds. Some of them are briefly described below:

(1) The limiting laminar layer model [93]: this model assumes that the core of the bed is isothermal and offers negligible thermal resistance while the main resistance limiting the rate of heat transfer between the bed and the heat source is in a fluid film near the hot surface. Thus, the particles act as turbulence promoters which erode the film and reduce its resistive effects (see also [94] for further details). Following this model, Wasan & Ahluwalia [95] assumed that the solid particles were stationary and equally spaced and that heat was transferred through the film and then spread by fluid convection into the bulk of the bed. They compared their

model with experimental works and found deviations of up to 44%.

(2) Two resistance film model: Wasmund & Smith [59] suggested a modified laminar layer model in which the particle convective transfer is due to radial motion of particles into the laminar layer. According to them, this mechanism is responsible for 50-60% of the total heat transferred and the remainder was from fluid convective transfer.

(3) Unsteady state heat transfer model: Mickley & Fairbanks [60] developed a model (also called 'renewal model') of heat transfer which assumed that at any time there is unsteady transfer within the fluidized bed close to heat source. This assumption can be divided into contributions due to solid/solid, solid/surface, gas/solid and gas/surface transfer. Hence, packets of particles were assumed to have uniform thermal properties through the fluidized bed. George & Smalley [96] measured the variations in local heat transfer coefficient within and adjacent to a rising bubble. They concluded that the heat transfer took place mainly through the fluid to the particle with the maximum rate in the vicinity of the contact part.

(4) Simplified model: Botterill & Williams *et al.* [97] proposed a model which was based on the unsteady state conduction of heat to spherical particles adjacent to the transfer surface. As the effective conductivity of the particle phase is larger than the effective conductivity of the gas phase, the convective transfer through the gas is neglected. Therefore, the particle and gas, whose temperatures were initially the same, approached the heated surface where a continuous thin layer of pure fluid is in contact with the particle and the thermal source.

(5) Particle replacement model: Gabor [98] proposed that heat was absorbed by the particles based on string of spheres of infinite length normal to the heat transfer surface. Gelperin and Einstein [5] suggested that the heat is transferred from the heated surface by packets of solid particles by gas bubbles and by gas passing between the packet and the surface.

Due to the lack of theoretical knowledge to describe heat transfer mechanisms in fluidized beds, several empirical correlations have been developed from the above models to calculate the local heat transfer coefficients. The results obtained from these expressions present deviations of up to 40% from experiments, as reported in [22, 61, 54]. Based on model (3), Mickley *et al.* [60, 99] proposed an expression for the instantaneous heat transfer coefficient at the surface of a packet which rested on a heated surface during a period of time. This expression, however, neglects the conductivity and voidage gradients in the heated surface and in the main body of the packet. Kunii & Levenspiel [4] modified this expression and took into account the bubble and the emulsion contributions to the thermal diffusion:

$$H_T = h_{wf} + h_{ws} \tag{3.1}$$

where

$$h_{wf} = \frac{6\kappa_f}{d_s} \tag{3.2}$$

$$h_{ws} = \frac{1}{\dfrac{1}{h_{emul}^{(f)}} + \dfrac{1}{h_{emul}^{(pack)}}} \tag{3.3}$$

with

$$h_{emul}^{(f)} = 2\frac{\kappa_{ew}^o}{d_s} + 0.05 C_f \rho_f \frac{u_f}{\varepsilon_f} \tag{3.4}$$

$$h_{emul}^{(pack)} = 1.13\sqrt{\frac{\kappa_e^o \rho_s \left(1-\varepsilon_{mf}\right) C_s n_w}{1-\delta_w}} \tag{3.5}$$

$$\delta_w = 1 - \frac{1-\varepsilon_f}{1-\varepsilon_{mf}} \tag{3.6}$$

$$\kappa_{ew}^o = \varepsilon_f \kappa_f + \left(1-\varepsilon_f\right)\kappa_s \left[\frac{1}{\phi_w\left(\kappa_s/\kappa_f\right)+1/3}\right] \tag{3.7}$$

$$\kappa_e^o = \varepsilon_{mf} \kappa_f + \left(1-\varepsilon_{mf}\right)\kappa_s \left[\frac{1}{\phi_b\left(\kappa_s/\kappa_f\right)+2/3}\right] \tag{3.8}$$

n_w is the bubble frequency, ϕ is the ratio of effective thickness of gas film around a contact point to particle diameter (ϕ_b for contact between adjacent particles and ϕ_w for particle-surface contacts).

3.3 Cooling of a Gas-Solid Fluidized Bed

A numerical simulation of a two-dimensional (2-D) gas-solid fluidized bed was performed by solving the balance equations. The thermohydrodynamic variables obtained are: velocity vectors, densities and temperatures of both phases and pressure. Solid particles, initially at 100^{o}C, are fluidized by air at 20^{o}C for over 25 minutes. Assuming $Bi << 1$, i.e., temperature uniformity across the particles, the only temperature gradient to be considered is between the solid and the gas phases. Thermal sources due to chemical reactions and radiative heat transfer are neglected.

	Solid Phase	**Gas Phase**
Density ($kg.m^{-3}$)	2.66×10^{3}	ideal gas law
Thermal Conductivity ($W.m^{-1}.K^{-1}$)	1.0	2.57×10^{-2}
Heat Capacity ($J.kg^{-1}.K^{-1}$)	7.37×10^{2}	9.94×10^{2}
Particle Diameter (m)	5.00×10^{-4}	–
Dynamic Viscosity ($kg.m^{-1}.s^{-1}$)	–	9.99×10^{-9}

Table 3.1: Physical properties of the solid (glass Ballotini particles) and gas (air) phases.

The set of conservative equations described in the previous sections are solved by the means of the multiphase flow finite-element based code, *FLUIDITY* (see [78, 11, 100] for further details). The momentum equations are discretized by a non-linear Petrov-Galerkin method which is applied to each of the velocity components. Continuity, granular temperature and thermal energy balances are discretized by a high-resolution method that is globally second order accurate in space and time.

Glass beads with a diameter of 500μm (Table 3.1) are initially held in a 23.0 cm high bed at 100.0^{o}C (Figure 3.1(a)). They are fluidized by air (Table 3.1), which enters the

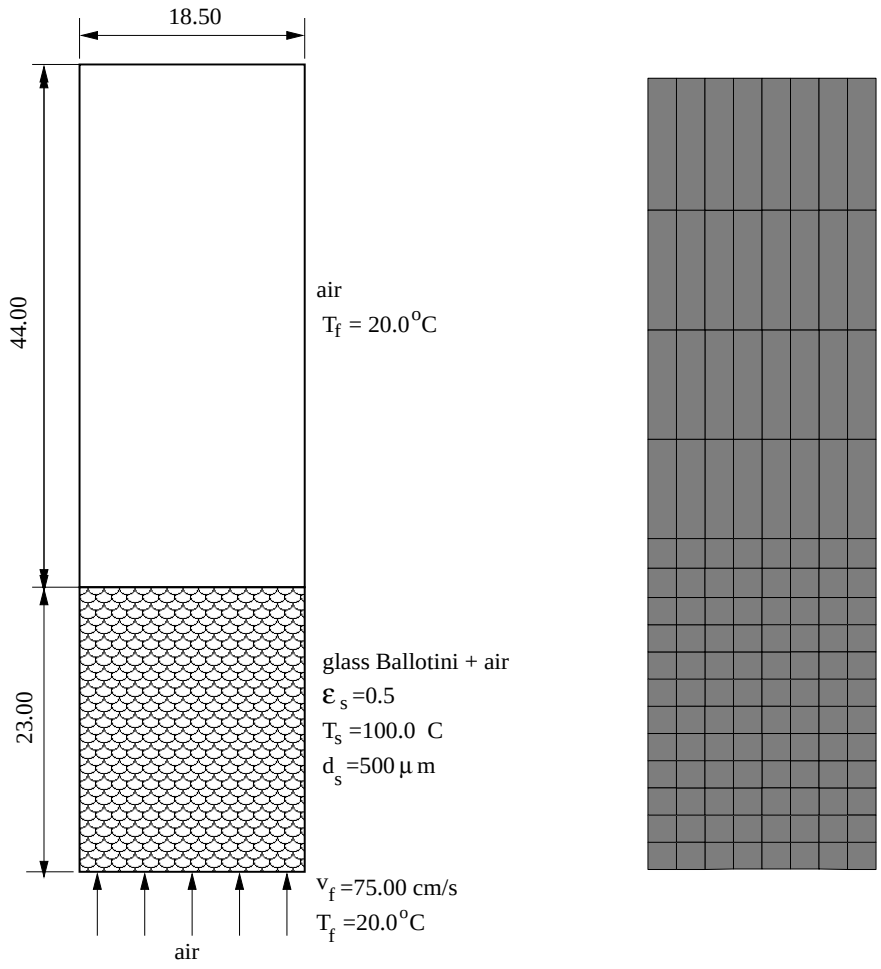

(a) Schematic (b) Mesh

Figure 3.1: (a) Schematic of the simulated fluidized bed used in this section. Glass Ballotini particles, initially loaded at 100^{o}C, are fluidized by air at room temperature and pressure conditions. The initial static bed height is set to 23.0 cm. All dimensions in cm. (b) 8×16 mesh used to discretise the domain in a 2-D cartesian geometry.

(a)	Inlet gas velocity	$\mathrm{v}_f\,(x, y=0, t)$=0.75 m.s^{-1}
(b)	Initial ε_s	0.50
(c)	Initial gas and solid phase velocities	$\mathrm{v}_s\,(x, y, t=0)$=0.0 m.s^{-1} $\mathrm{v}_f\,(x, y\neq 0, t=0)$=0.0 m.s^{-1}
(d)	Initial gas and solid temperatures	$\mathrm{T}_f\,(x, y, t=0)$=20 ^{o}C $\mathrm{T}_s\,(x, y, t=0)$=100.0 ^{o}C
(e)	Solid flow in the top	$\mathrm{v}_s\,(x, y=L, t)$=0.0 m.s^{-1}
(f)	Solid stress in the top	$\tau_s\,(x, y=L, t)$=0.0 N.m^{-2}
(g)	Particle-particle restitution coefficient	e_{pp}=0.97
(h)	Wall-particle restitution coefficient	e_{wp}=0.90
(i)	Friction coefficient	$\overline{\mu}$=0.10

Table 3.2: Initial and boundary conditions used in the numerical simulation reported in this section.

domain with an inlet velocity of 75 cm.s^{-1}, at room temperature and standard pressure. The initial and boundary conditions are summarized in Table 3.2. The initial bed porosity and the solid and fluid velocity were set to 0.50 and 0.0 m.s^{-1}, respectively. The inlet and initial fluid phase temperature was set to 20.0^{o}C. As the solid phase must stay in the domain while the fluid phase leaves it without restriction, normal flow to the solid phase was forbidden and zero shear stress conditions for both phases were applied. At the walls, shear stress was prescribed by the solution of the Blasius equation [101] with a length scale equal to the static height of the bed. Boundary conditions as described by Jenkins [80] (see also [78]) were prescribed for the wall region. In addition, a friction coefficient of 0.10, and particle-particle, wall-particle restitution coefficients of 0.97 and 0.90, respectively, were applied to the fluidized system.

The numerical simulation was performed in a 2-D cartesian geometry. Quadrilateral elements provided a bi-linear variation of velocity and piece-wise-constant variations of volume fraction, pressure and granular temperature. A 8×16 mesh was used to discretise the domain in a 2-D cartesian geometry (Figure 3.1(b)).

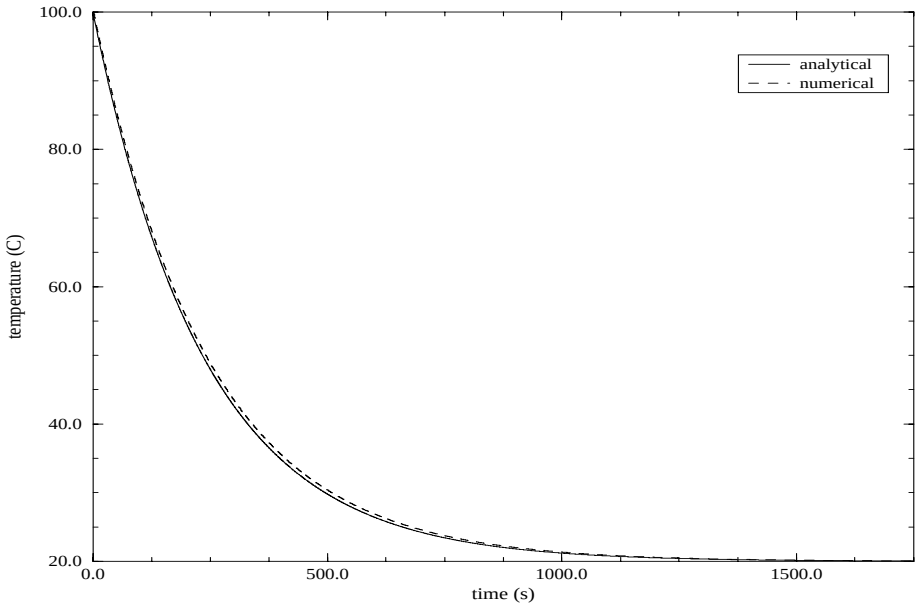

Figure 3.2: Comparison between the gas temperature obtained from the numerical simulation and from the analytical solution.

The simulation was performed over 25 minutes, and the mean gas phase temperature was calculated throughout the domain. The fluid phase temperature quickly rises from the ambient temperature to nearly 90.0^{o}C. Before the simulation reaches a quasi-steady state regime, the fluid phase temperature oscillates as a result of the intense mixing due to rising bubbles. After these initial oscillations, the temperature becomes more homogeneous and decreases slowly as fresh and cold fluid diffuses through the domain cooling the particles. Hence the bed temperature tends towards the inlet gas temperature in a long simulation. In order to evaluate the results achieved from the numerical simulation presented in this work, an analytical solution was obtained from a simplified model (for a full description, see Appendix A):

$$T = T_f^o + T^{(inl)} \exp\left(\frac{\psi \Delta t}{\eta}\right) \tag{3.9}$$

where

$$\eta = \rho_s C_s V_s + \rho_f C_f V_f \quad ; \quad \psi = \rho_f C_f v_f \overline{A}$$

As shown in Figure 3.2, the temperature obtained from the numerical simulation matches the analytical solution, improving the confidence in the numerical results presented in next session.

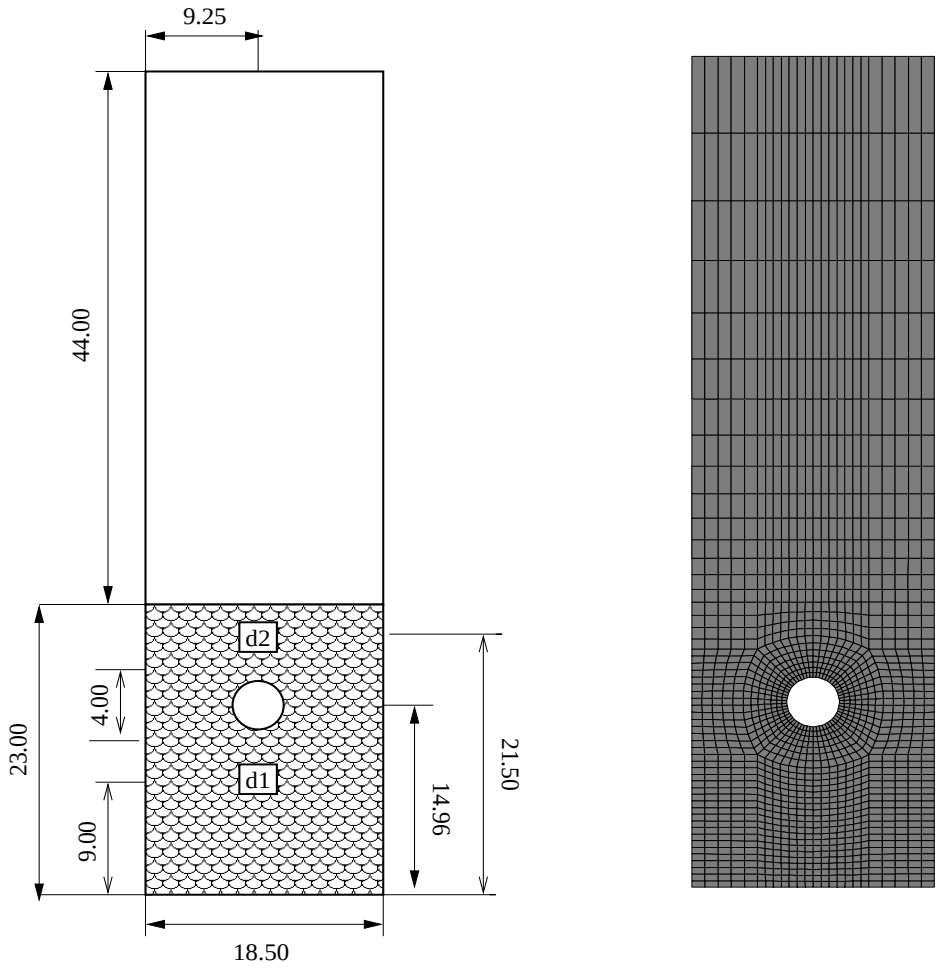

(a) Schematic (b) Mesh

Figure 3.3: (a) Schematic configuration of the simulated fluidized bed used in Section 3.4. All dimensions in cm. (b) Mesh used to discretise the domain in a 2-D cartesian geometry. There are 1599 nodes in 1492 elements.

Correlation	Simulation
Classical approach (Equation 2.25)	case 01x
Kinetic approach 1 (Equation 2.27)	case 02x
Kinetic approach 2 (Equation 2.29)	case 03x

Table 3.3: Set of simulations performed in this work using different correlations for the solid phase effective thermal conductivity calculations. x (=a, b or c) is related to the particle-particle restitution coefficient and friction coefficient described in Table 3.4

	e_{pp}	$\overline{\mu}$
case 0Ya	0.97	0.10
case 0Yb	0.97	0.05
case 0Yc	0.90	0.05
case 0Yd	0.90	0.10

Table 3.4: Restitution and friction coefficients used in the simulations presented in this work. The index $1 \leq Y \leq 3$ refers to the correlation used to obtain the effective conductivity coefficient described in Table 3.3.

3.4 Flow Past a Heated Cylinder

500μm diameter glass beads at 20^{o}C are fluidized by air at room temperature and standard pressure in a lab-scale gas-solid fluidized bed as shown in Figure 3.3(a). At 10.96 cm above the distributor a cylinder of 4.00 cm diameter is maintained at 100^{o}C. All the thermophysical properties for both phases are described in Table 3.1. The boundary conditions used in the simulations in this section are the same as those used in Section 3.3, and summarized in Table 3.2, with the exception that the initial bed temperature (for both phases) was set to 20^{o}C. To help investigate the fluidization dynamics, two detectors (Figure 3.3(a)) were placed within the domain and the resulting time series of voidage fluctuations were analyzed. Figure 3.3(b) shows the grid used to discretize the domain for this simulation.

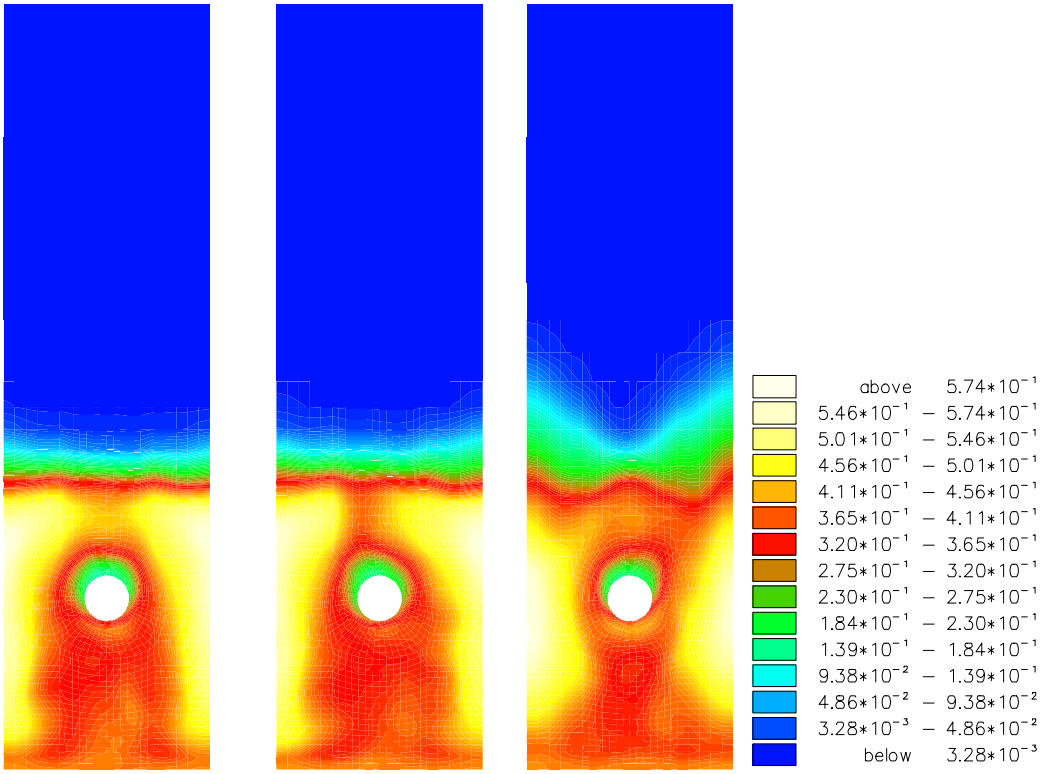

(a) case 01a (b) case 02a (c) case 03a

Figure 3.4: Flow past a heated cylinder: time-averaged solid volume fraction, calculated using three different correlations for the thermal conductive coefficient (Tables 3.3 and 3.4). Although the symmetry is not broken, there are differences in the height, in a time-average sense.

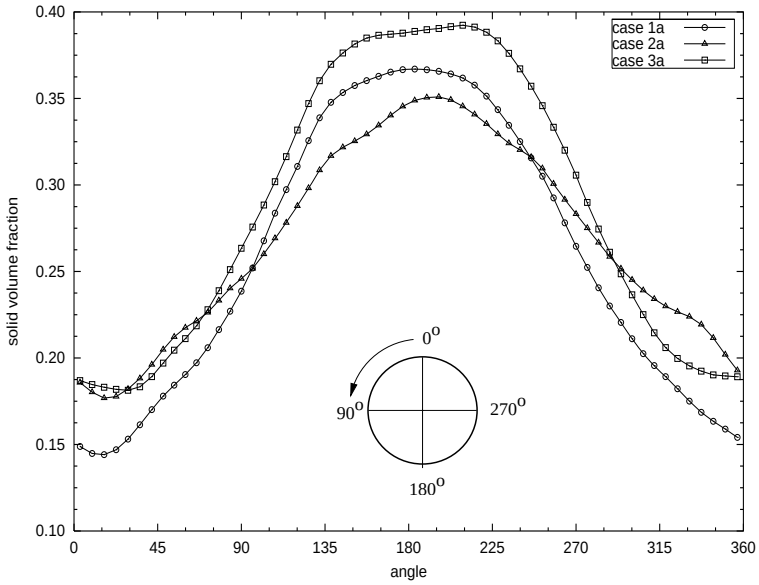

(a) solid volume fraction

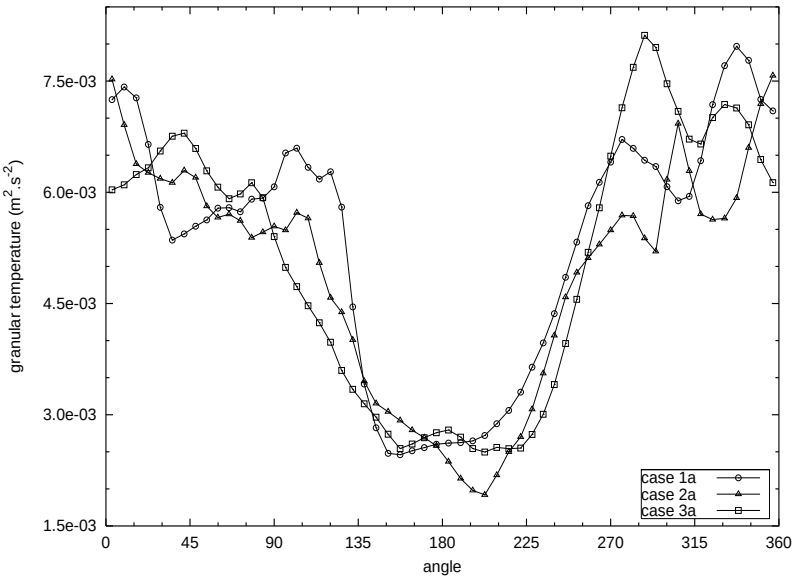

(b) granular temperature

Figure 3.5: Flow past a heated cylinder: time averaged (a) solid volume fraction and (b) granular temperature (in $m^2.s^{-2}$) around the cylinder for all correlations. The angles are measured anti-clockwise from the top of the cylinder.

3.4.1 Influence of the Solid Effective Conductivity on the Hydrodynamics

In order to investigate the influence of the solid effective conductivity on the gas-solid fluidization hydrodynamics, a set of simulations were performed in the fluidized bed described in Figure 3.3 using the correlations shown in Table 3.3. Although all simulations were performed to 25 seconds, the analysis was performed just after they reached stationarity, which was evaluated by the means of the power spectra of voidage fluctuations at several points throughout the bed [11].

The time-averaged solid volume fraction of the three simulations are shown in Figures 3.4 and 3.5(a). Although no large discrepancy between the solid volume fraction can be observed, some interesting features may be noticed:

(i) a similar solid volume fraction distribution in the region below the cylinder in cases 01a and 02a (Figures 3.4(a-b) and 3.5(a));

(ii) a larger time-averaged bed height for case 3a in comparison with the other two cases, which present a similar bed height (Figures 3.4(a-c)).

(iii) larger solid concentration just below the cylinder.

The larger time-averaged bed height observed in case 3a is due to a larger energy dissipation rate during the simulation caused by streaming effects on the effective conductivity (Equation 2.29), i.e., effects due to the random motion of particles and gas molecules which increases during the momentum transfer. This effect can also be seen in Figures 3.5(a,b), where solid volume fraction and granular temperature are plotted against angle in the vicinity of the cylinder. A lower granular temperature in a high solid volume fraction region is explained by the lower mean free path for inter-particle collisions and subsequently a lower inter-particle momentum transferred. The larger granular temperature at angles of 90^o and 270^o is due to the rising bubbles, which collide with the cylinder with a relatively higher solid concentration in their wake, and circulate around the cylinder, enhancing the shear stress in these regions.

The solid time-averaged effective thermal conductivity obtained around the cylinder

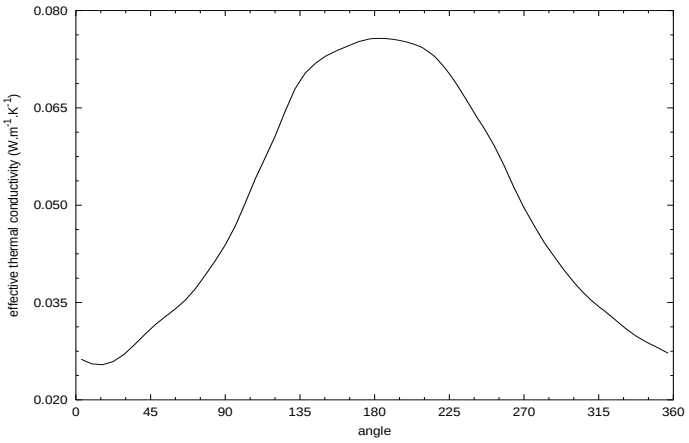

(a) case 1a (Eqn. 2.25)

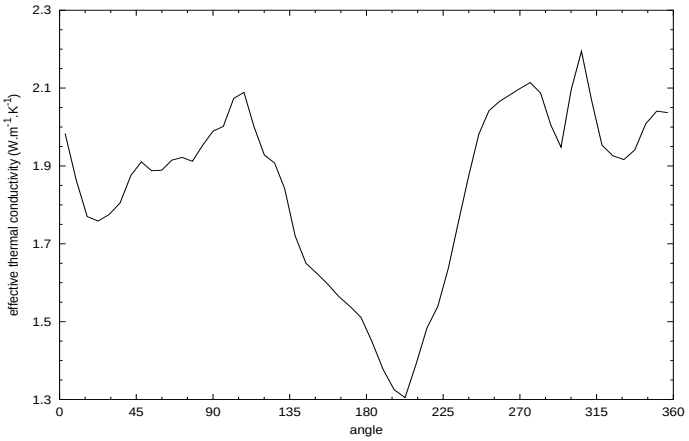

(b) case 2a (Eqn. 2.27)

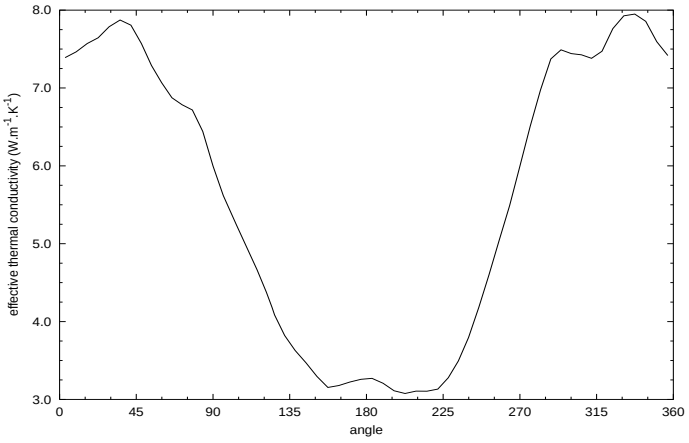

(c) case 3a (Eqn. 2.29)

Figure 3.6: Flow past a heated cylinder: time average effective conductivity (in $W.m^{-1}.K^{-1}$) measured around the cylinder for the three cases (see Table 3.3). The angles are measured anti-clockwise from the top of the cylinder.

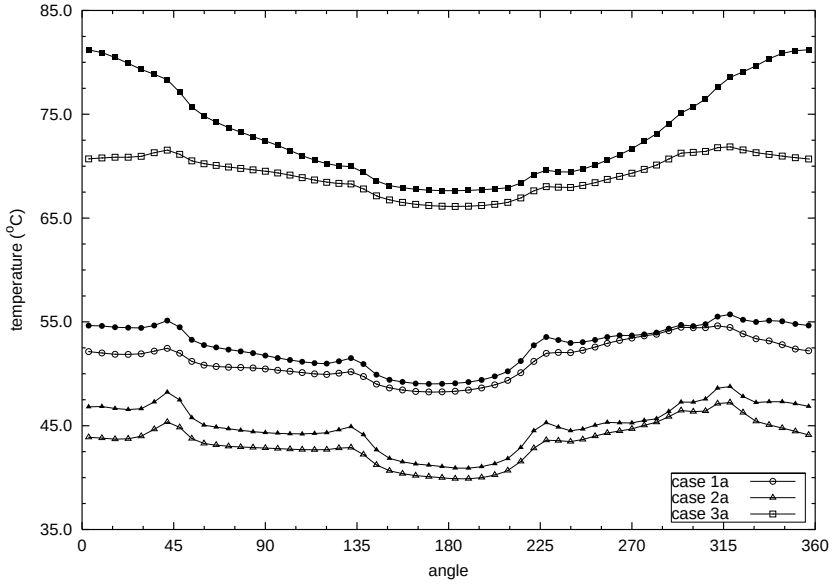

Figure 3.7: Flow past a heated cylinder: time-averaged fluid (empty symbols) and solid (filled symbols) phase temperatures measured around the cylinder for the three cases (see Table 3.3). The angles are measured anti-clockwise from the most top of the cylinder.

is shown in Figure 3.6. In the case 1a, as the effective conductivity, $\varepsilon_s \kappa_s$, is a function of the thermophysical properties of both phases and of the porosity, it merely reflects the shape of the solid volume fraction shown in Figure 3.5(a). However, the solid effective conductivity of cases 2a and 3a mirrors the granular temperature behavior, as shown in Figure 3.5(b) and described in Equations 2.27 and 2.29. Although the shape of cases 2a and 3a in Figure 3.6(b-c) is very similar, the effective conductivity coefficient obtained for case 3a is 2.5-3.0 times larger than that obtained for case 2a due to streaming effects presented in case 3a.

The time-averaged temperature of both phases around the cylinder for each case, presents a small gradient in temperature as shown in Figure 3.7. In addition, a difference in the order of 15.0^{o}C between cases 3a and 2a indicates that although the streaming and collisional modes, described in Equation 2.29, act in opposition as the porosity varies through the domain, they enhance the thermal diffusion more effectively than those described by Equations 2.25-2.28.

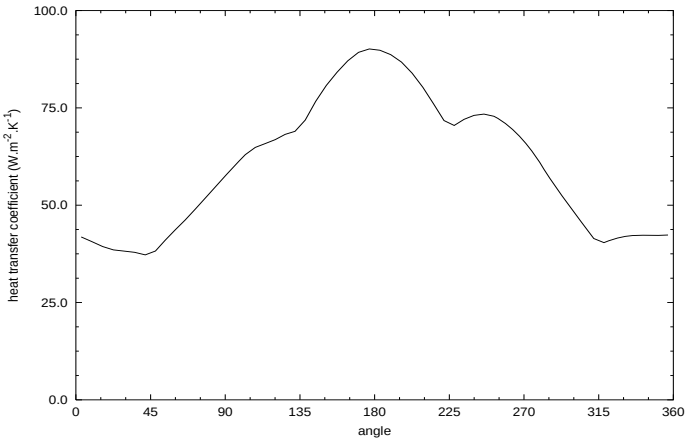

(a) case 1a (Eqn. 2.25)

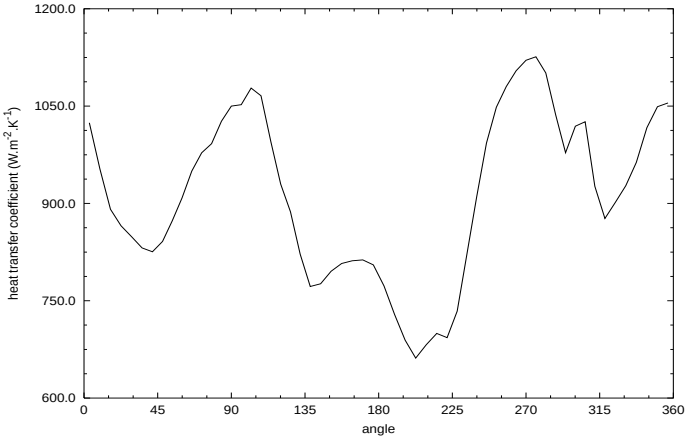

(b) case 2a (Eqn. 2.27)

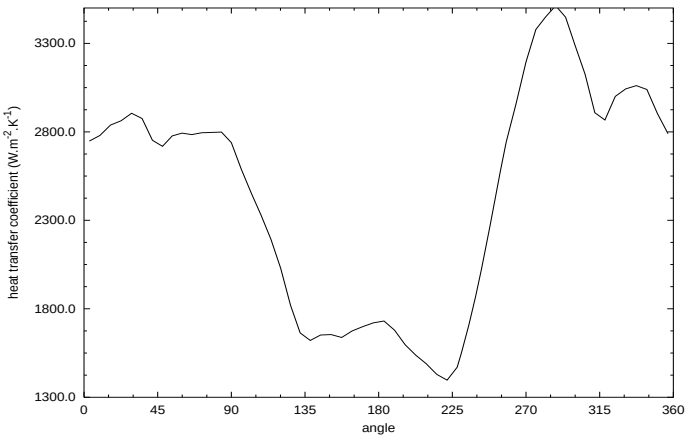

(c) case 3a (Eqn. 2.29)

Figure 3.8: Flow past a heated cylinder: time average heat transfer coefficient (in $W.m^{-2}.K^{-1}$) measured around the cylinder for the three cases (see Table 3.3). The angles are measured anti-clockwise from the top of the cylinder.

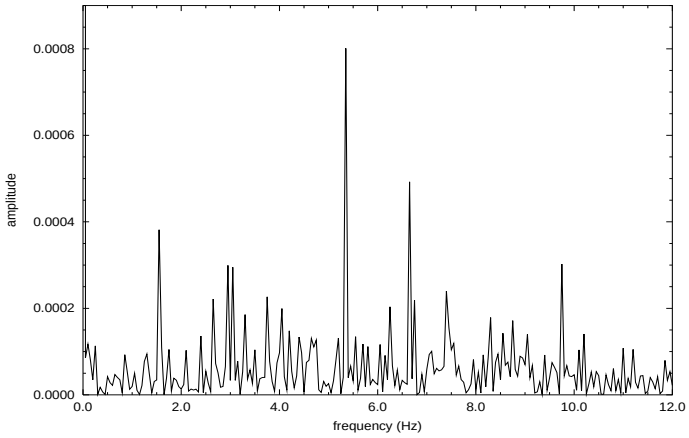

(a) case 1a (Eqn. 2.25)

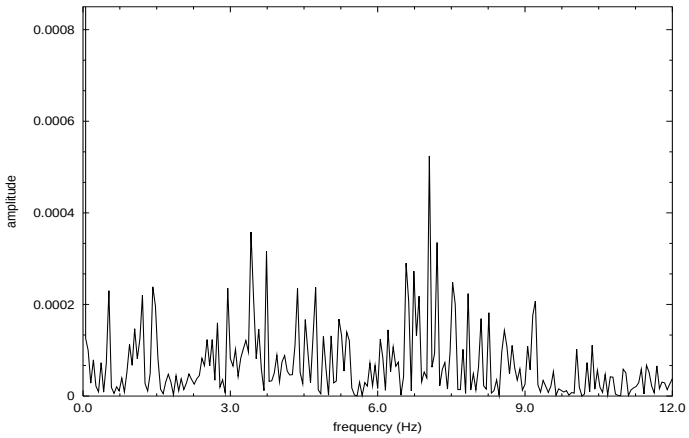

(b) case 2a (Eqn. 2.27)

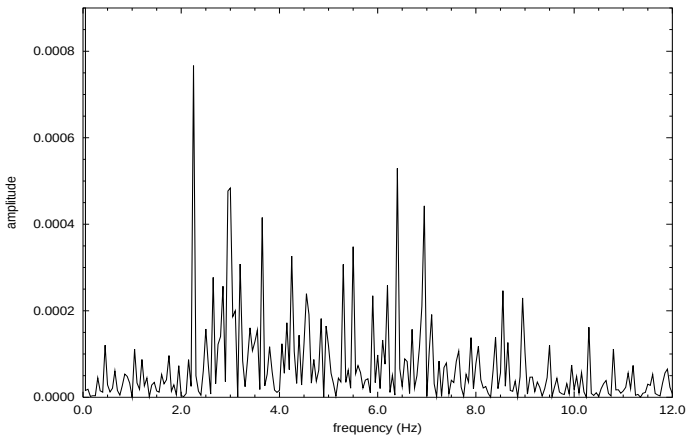

(c) case 3a (Eqn. 2.29)

Figure 3.9: Flow past a heated cylinder: power spectra density of voidage fluctuations at detector d1 (9.25cm,9.00cm).

In this work, the heat transfer coefficient is calculated based of the boundary conditions (Fourier's Law):

$$\kappa \nabla T = H_T \left(T_f - T_s \right) \tag{3.10}$$

In the performed simulation, the thermal energy source is due to the heated cylinder and the vertical walls are considered adiabatic. The heat transfer coefficient is obtained from the cylinder wall, which is held at 100^{o}C:

$$H_T = \left(\varepsilon_f \kappa_f \right) \left| \frac{\left(\frac{\partial T_f}{\partial n} \right)\Big|_w}{T_w - T_{susp}} \right| + \left(\varepsilon_s \kappa_s \right) \left| \frac{\left(\frac{\partial T_s}{\partial n} \right)\Big|_w}{T_w - T_{susp}} \right| \tag{3.11}$$

where T_{susp} is the temperature of the suspension around the cylinder. Therefore, the heat transfer coefficient was calculated from the temperature gradient between the suspension and the wall, accounting for a thermal boundary layer at the wall. The calculated time-averaged heat transfer coefficient is shown in Figure 3.8. In the limiting case, when there is no particle in the domain, the heat transferred from the thermal source to the fluid phase is assumed to be negligible (Section 2.3.8).

After the numerical simulations reached stationarity, the power spectra density of the voidage fluctuations were calculated for each of the cases investigated in this work, as shown in Figure 3.9. Such voidage fluctuations were obtained from a detector placed just below the cylinder (see $d1$ in Figure 3.3). Cases 1a, 2a and 3a present dominant frequencies of 5.5, 7.0 and 6.5 Hz, respectively. However, all the cases present a second large peak at 2.0 and 7.0 Hz. Moreover, case 3a exhibits a larger peak at 2.5 Hz that may be related either to an entirely different dynamics from that in the other test-cases, or to the formation of waves due to larger energy dissipation. Hence, the differences between the dominant frequencies exhibited for the three cases show that the overall dynamic was influenced by the correlation used to calculate the solid effective conductivity.

The long residence time of the evolving bubbles allow the crashing among them and against the cylinder. Such collisions may produce larger bubbles, however this bubbles' coalescencing phenomena can be better visualized by increasing grid resolution. Nevertheless enhancing the number of elements would make the simulation prohibitive due to the higher computational cost. The simulations showed throughout this work were per-

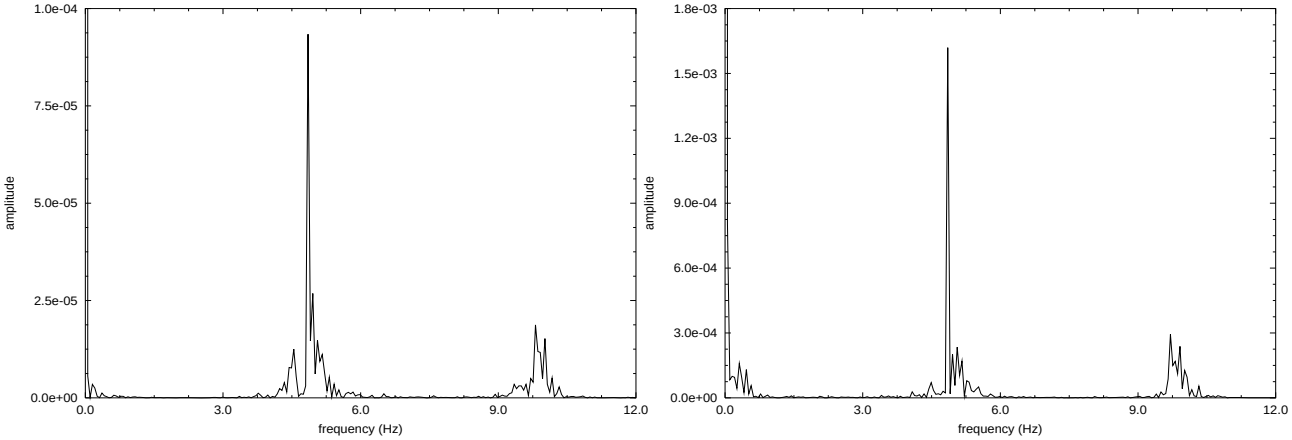

(a) coarse grid: detector 1

(b) coarse grid: detector 2

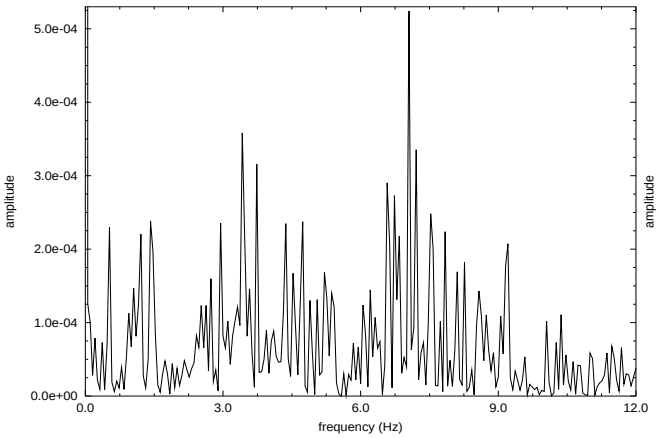

(c) current grid: detector 1

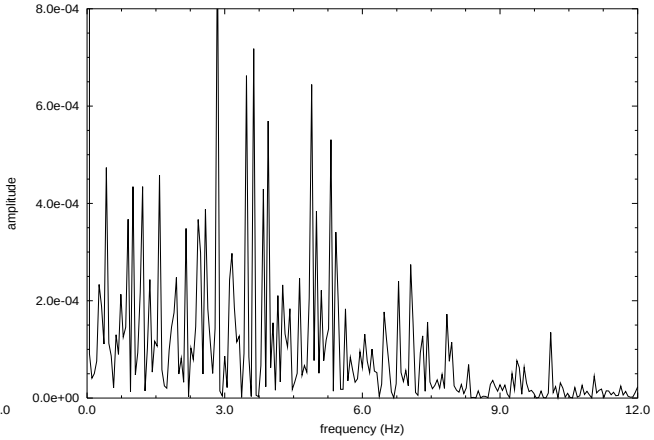

(d) current grid: detector 2

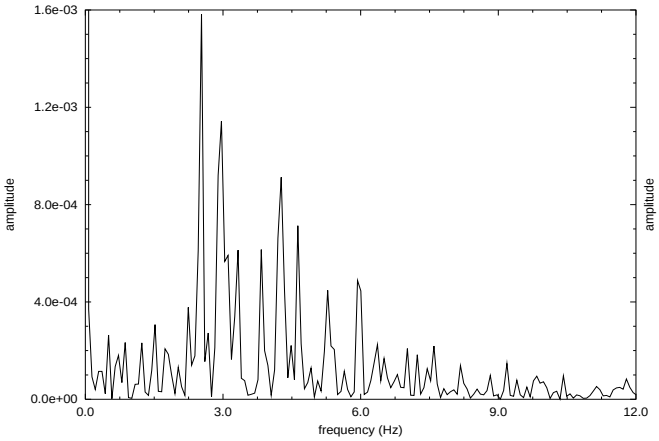

(e) fine grid: detector 1

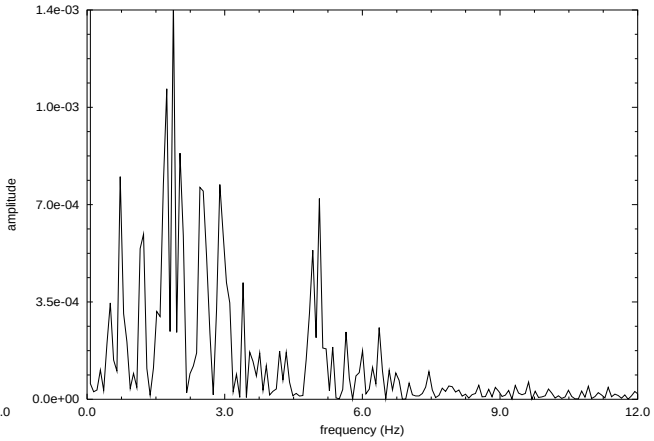

(f) fine grid: detector 2

Figure 3.10: Flow past a heated cylinder: power spectra density of voidage fluctuations at detectors d1 (9.25cm,9.00cm) and d2 (9.25cm,21.50cm) for (a) coarse mesh (428 elements), (b) current mesh (1492 elements) and (c) fine mesh (3280 elements)

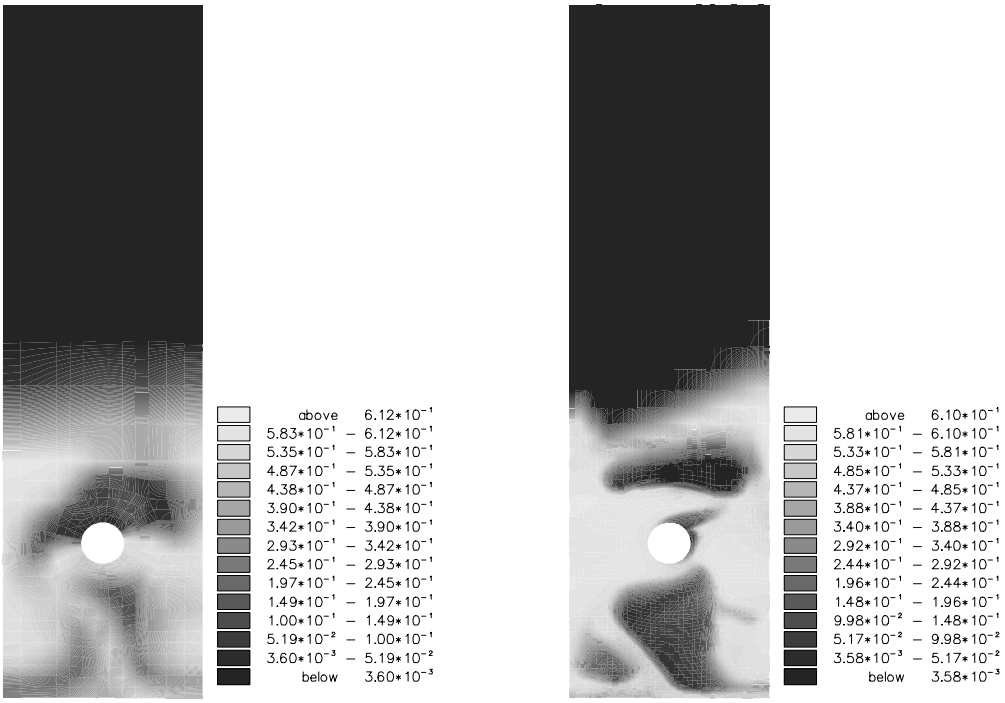

(a) coarse grid (b) current grid

(c) fine grid

Figure 3.11: Flow past a heated cylinder: solid volume fraction snapshots from simulations performed using (a) coarse (428 elements, t = 41.25 s), (b) current (1492 elements, t = 24.56 s) and (c) fine (3280 elements, t = 18.40 s) grids.

formed using 1492 quadrilateral elements, however in Figures 3.10 and 3.11, simulations using 428 and 3280 elements are also shown. In Figure 3.10, the power spectra density were calculated from voidage fluctuations obtained from detectors 1 and 2 (Figure 3.3), which are just bellow and above the cylinder, respectively. Due to the collisions between the rising bubbles and the cylinder, large bubbles are formed, therefore in the region just above the cylinder, large coalesced bubbles rise and are released in the free surface. In the coarse mesh a single peak can be observed due to the lower grid resolution which led to smearing bubbles as shown in Figure 3.11(a). However, several peaks appear in the PSD calculated from both, current and fine simulations, as shown in Figure 3.10(c-f); these peaks are related to a better grid resolution which leads to coalescence phenomena. The lower dominant frequency in the simulation performed with the fine grid is due to the larger coalescence which can be observed in Figure 3.11(c), where small bubbles are assembling to constitute larger bubbles. Similar behavior can be noticed in the simulation performed with the current resolution, Figure 3.11(b). This phenomena can also be observed through the PSD shown in Figures 3.10(c-f), where the dominant frequencies are 2.0, 4.5 and 7.0 Hz for the current simulations, and 2.5, 4.5 and 6.0 Hz for the simulation performed using a fine mesh.

Kuipers *et al.* [63] reported that the heat transfer coefficient is enhanced in the rear of the bubbles, where fresh, cold material replaces hot suspension due to the vigorous vortices formed in this region. In fact, such vortices are due to an intense mixing in the bubbles' wake which produces larger heat transfer coefficients as shown in the sequence of frames of Figure 3.12 and in the heat transfer coefficient plotting in Figure 3.13.

In Figure 3.13, as the bubbles pass by the cylinder, the heat transfer coefficient is enhanced in the wake region of these bubbles and drops again at 270^o around the cylinder. In this position, initially at a high solid volume fraction, a low H_T is obtained, however, as the bubbles splash into the obstacle carrying fresh, cold gas and solid, the heat transfer coefficient is increased (see the sequence of lines with squares, circles and triangles at this coordinate). However, as the system evolves in time and the temperature gradient is decreased, H_T falls slowly.

The intense mixing in fluidized beds enhances the heat transfer and ensures tempera-

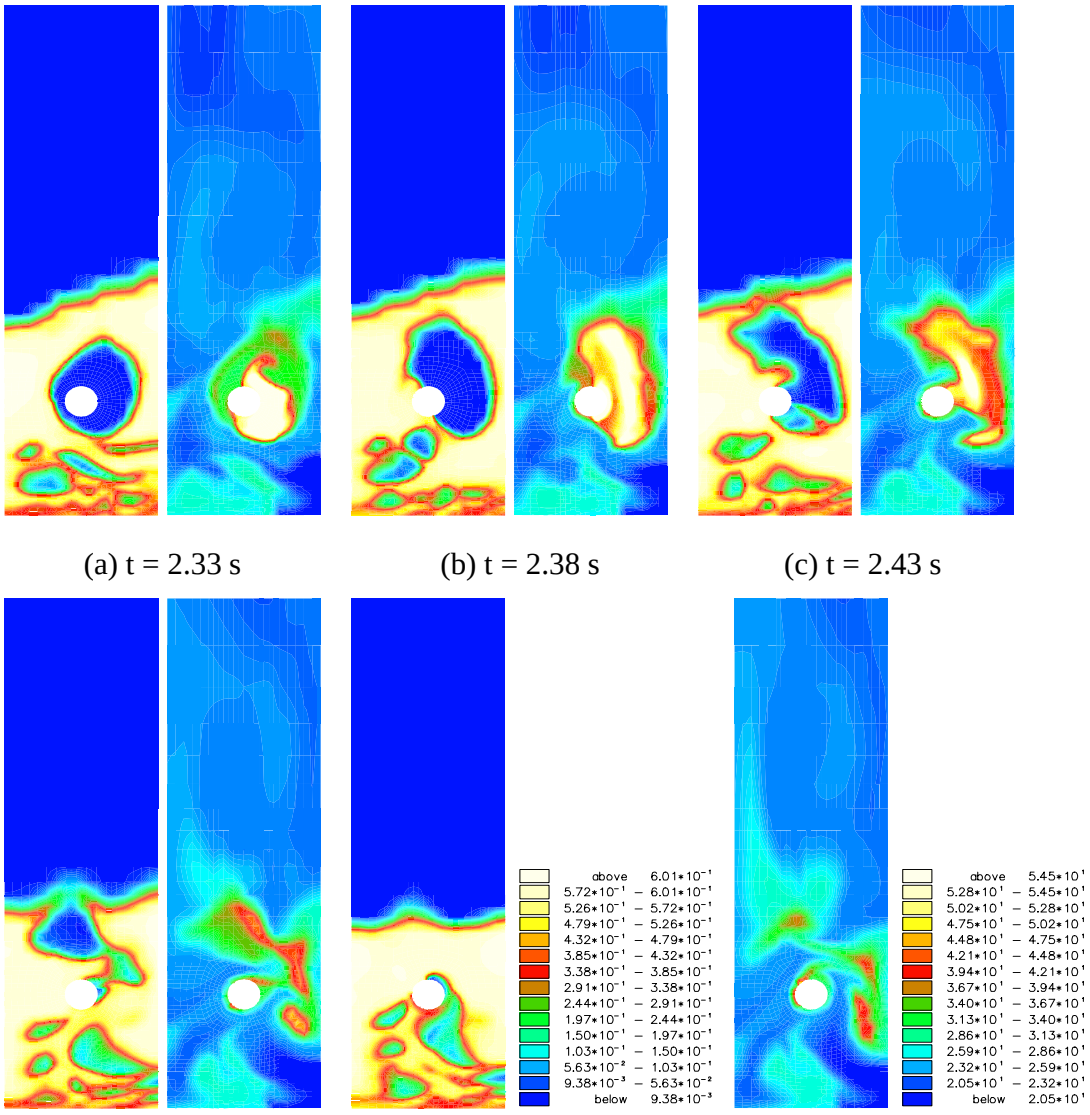

(a) t = 2.33 s (b) t = 2.38 s (c) t = 2.43 s

(d) t = 2.48 s (e) t = 2.51 s

Figure 3.12: Flow past a heated cylinder: sequence of snapshots of a rising bubble splashing into the heated cylinder: gas temperature (r.h.s.) and solid volume fraction. A snapshot was taken every 0.05 seconds.

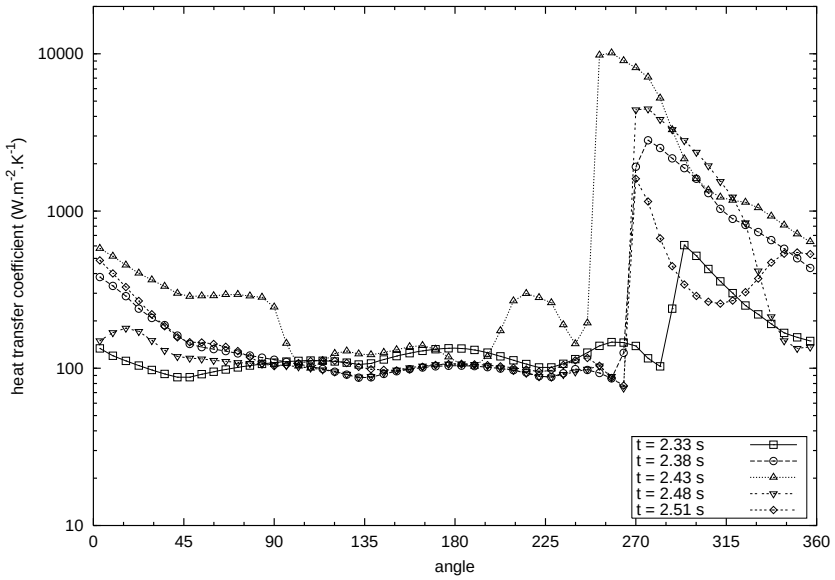

Figure 3.13: Flow past a heated cylinder: heat transfer coefficient (Equation 3.11) calculated using the solid effective conductivity from the standard approach (Equation 2.25): (a)t = 2.33 s, (b)t = 2.38 s, (c)t = 2.43 s, (d)t = 2.48 s, (e)t = 2.51 s.

ture uniformity throughout the bed as shown in Figures 3.14 (a-f). Along 25 seconds the gas temperature increases smoothly as the bubbles rise and splash into the heated cylinder and the particles fall along the wall.

Table 3.5 compares the heat transfer coefficient obtained from experimental results available in the literature and some numerical results using the standard and the kinetic 1 approach. Although some of the initial conditions and properties used for both experiments and numerical simulations, are slightly different, the overall range of calculated heat transfer coefficient obtained from experiment agrees with the numerical results. However, although the discrepancy between the numerical results using the standard and kinetic 1 (Equations 2.25 and 2.27, respectively) approaches is relatively small, the advantage of using a model that is consistent with the hydrodynamics model is strongly suggested. In addition, the total heat transfer coefficients obtained from boundary conditions (Equations 3.10-3.11) agree well with those obtained from the empirical correlation presented in [4] (Equations 3.1-3.3). Therefore the fundamental model, due to the granular temperature two-fluid approach, provides greater confidence in the global time-averaged

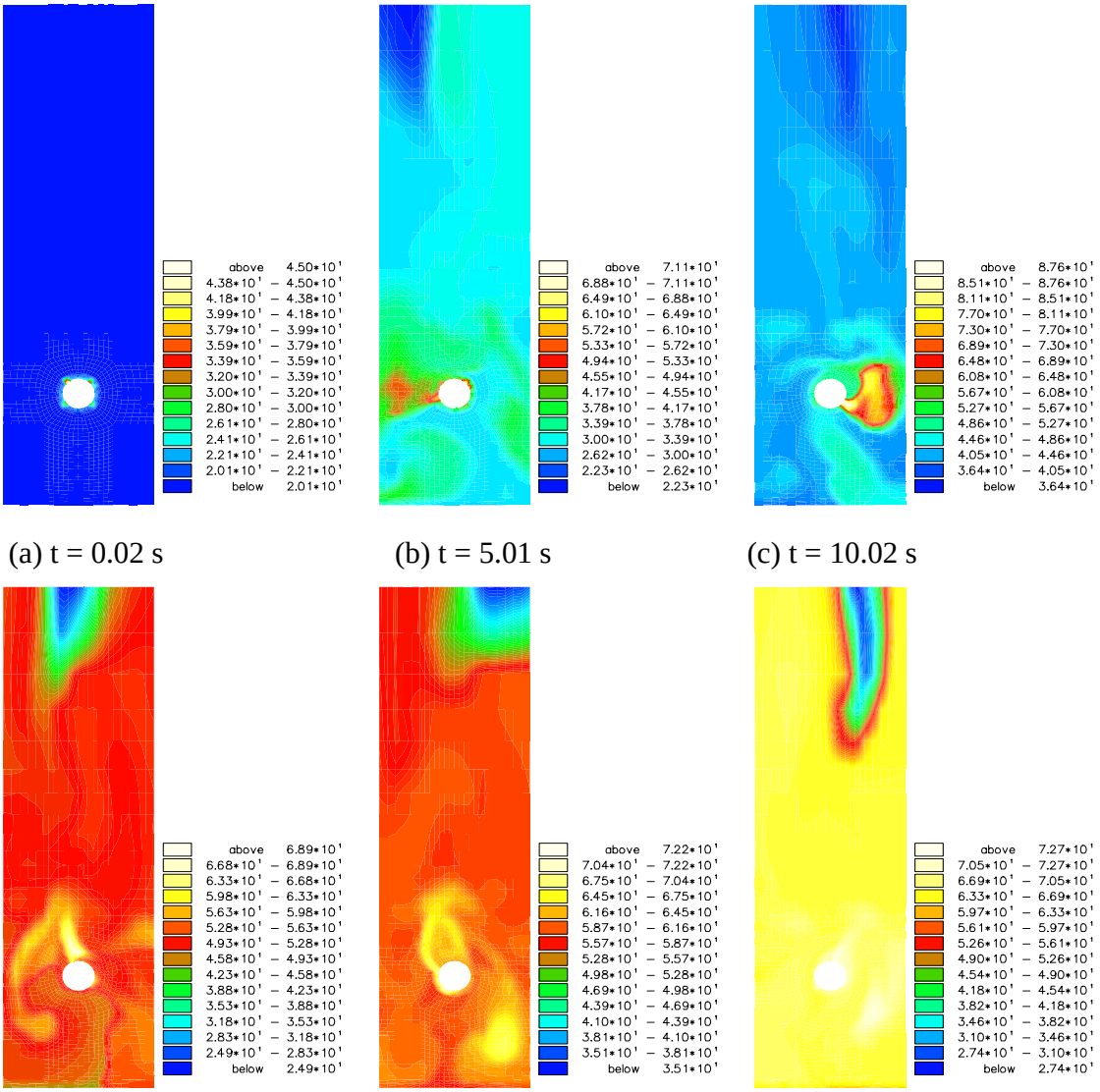

(a) t = 0.02 s (b) t = 5.01 s (c) t = 10.02 s

(d) t = 15.04 s (e) t = 20.05 s (f) t = 24.93 s

Figure 3.14: Flow past a heated cylinder: gas temperature evolving in time.

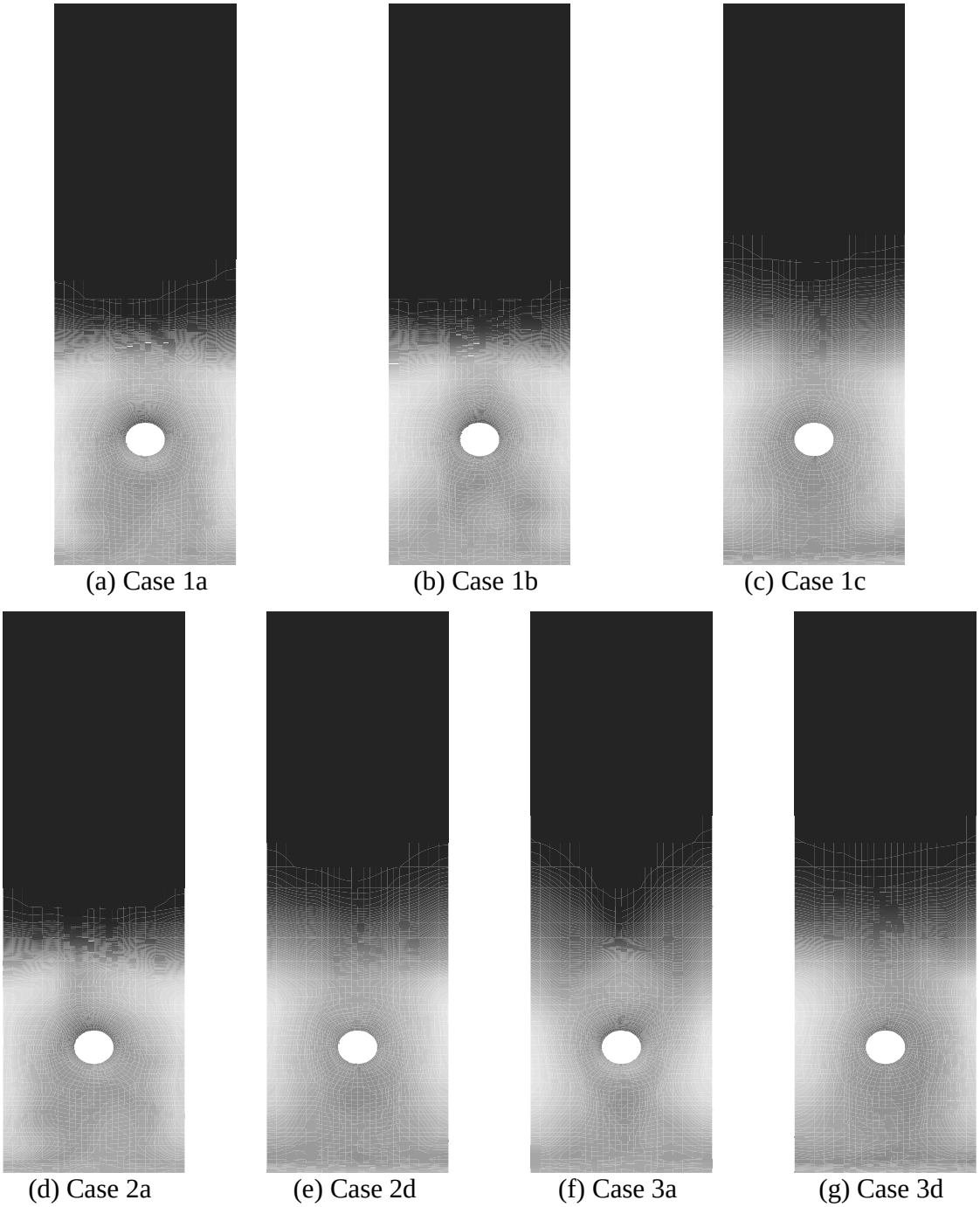

(a) Case 1a (b) Case 1b (c) Case 1c

(d) Case 2a (e) Case 2d (f) Case 3a (g) Case 3d

Figure 3.15: Flow past a heated cylinder: time-averaged solid volume fraction. Although the symmetry is maintained for all cases, there are differences in the bed height (Tables 3.3 and 3.4).

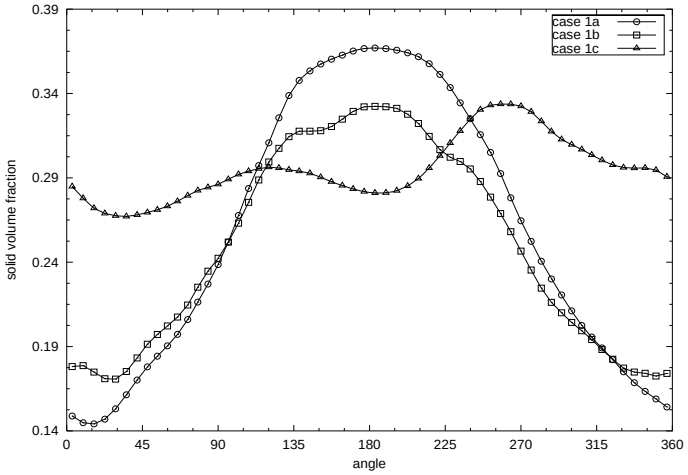

(a)

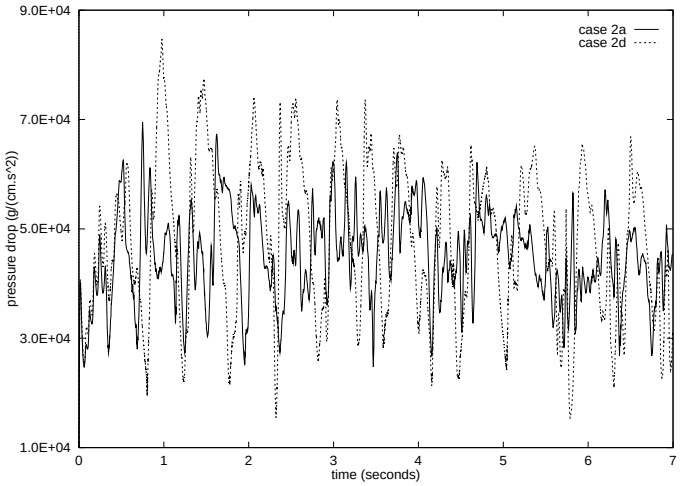

(b)

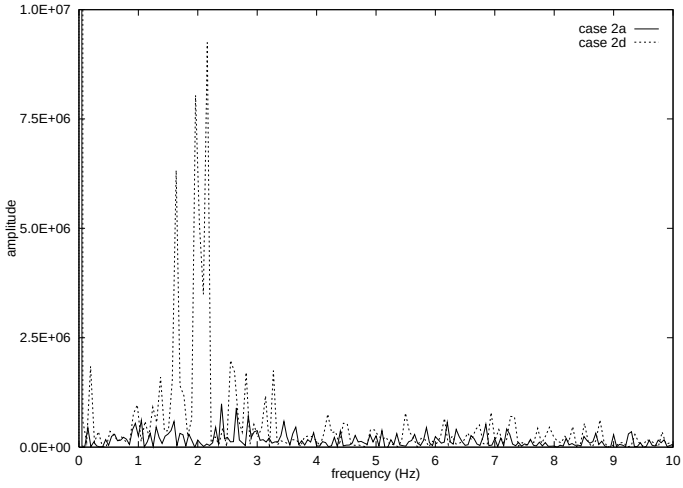

(c)

Figure 3.16: Flow past a heated cylinder: influence of the dissipation energy parameters defined in Table 3.4 (see also Table 3.3)on the (a) time-averaged solid volume fraction around the cylinder (the angle is measured anti-clockwise from the top of the cylinder), (b) on the pressure drop fluctuations of detector 1 (Figure 3.3) for the first 7 seconds of simulation and (c) on the PSD of the pressure fluctuations measured at detector 1 after stationarity was reached.

heat transfer rates than experimentally obtained correlations, as the first resolves space and time evolving flow and heat transfer properties.

Source	d_{cyl} (mm)	d_s (μm)	v_{gas} $(m.s^{-1})$	H_T $(W.m^{-2}.K^{-1})$
Sunderesan & Clark [62]	50	467	0.323	273.2-513.2
Mickley *et al.* **[99]**	6.35	40-300	0.186	50-1350
			0.086	50-525
Classical Approach (Eqn. 2.25)				
Eqn. 3.11	40	500	0.75	247.6
Eqn. 3.1	40	500	0.75	370.0
Kinetic Approach 1 (Eqn. 2.27)				
Eqn. 3.11	40	500	0.75	262.0
Eqn. 3.1	40	500	0.75	380.0

Table 3.5: Experimental and numerical heat transfer coefficients obtained from this work. Note that for the numerical results, the velocity of the gas is the inlet superficial gas velocity. Equation 3.1, described in Section 3.2, calculates the global heat transfer coefficient. Equation 3.11 calculates the local heat transfer coefficient from the boundary condition, which simulates interphase heat transfer between the surface and the environment.

3.4.2 Influence of the Restitution Coefficient on the Hydrodynamics

As granular collisions play an important role in the solution of the set of equations which govern fluidization phenomena, many researchers [72, 80, 83, 84, 102] have focused on finding realistic constitutive relations for dense flows in which the collisions are inelastic. In fact, the dissipative kinetic energy parameters, i.e, restitution and friction coefficients, exert a strong influence on the hydrodynamics of dense and dilute granular flow as reported by Goldschmidt *et al.* [103]. They investigated the behavior of some hydrodynamics parameters, such as solid pressure, granular temperature and solid viscosities, during the fluidization of 150 μm particles with a density of 2523 kg.m^{-3}. A numerical

investigation was performed by using dissipative kinetic energy parameters (e_{pp}, e_{wp} and $\overline{\mu}$) obtained from experimental results from a lab-scale gas-solid fluidized bed by Kharaz *et al.* [104].

Goldschmidt *et al.* [103] verified that as the particle-particle restitution coefficient decreases, the fluidization becomes more vigorous. Indeed, as the particle collisions become less ideal (more inelastic), more energy is dissipated, and, the particles tend to become packed in the densest regions of the bed, which leads to sharper gas volume fraction contours and larger bubbles.

In order to investigate the influence of the particle-particle restitution coefficient (e_{pp}) and the friction coefficient ($\overline{\mu}$) on the hydrodynamics, a set of simulations was performed using these coefficients with values shown in Table 3.4. Figures 3.15(a-g) show the time-averaged solid volume fraction for all cases considered in this work. Although the symmetry is maintained for all cases, some discrepancies can be observed. In the cases 1a and 1b (e_{pp}=0.97), the friction coefficient, $\overline{\mu}$, decreases from 0.10 to 0.05, and slight differences are observed throughout the domain in particularly at the top and bottom of the cylinder (Figure 3.16(a)). However, in case 1c, the bed height, in a time-averaged sense, was slightly higher than the two other cases, which was expected since the particle-particle restitution coefficient was smaller (e_{pp}=0.90) than cases 1a and 1b, i.e., the fluidization was more vigorous. In addition, the time-averaged solid volume fraction obtained around the cylinder, different from cases 1a and 1b (Figure 3.16(a)) presents a flat profile, i.e., in a time-averaged sense, a smooth solid concentration in this region ($0.27 \leq \varepsilon_s \leq 0.34$).

Figures 3.15(d-g) show the time-averaged solid volume fraction for cases 2a, 2d, 3a and 3d, using the same friction coefficient ($\overline{\mu}$=0.10) but varying the particle-particle restitution coefficient:(a)e_{pp}=0.97 and (d)e_{pp}=0.90 (Table 3.4). These values were chosen because, according to the literature, they are the most widely used in numerical simulations and represent nearly inelastic collisions [36, 32, 8, 105]. Nevertheless, quasi-elastic collisions ($0.99 \leq e_{pp} \leq 0.997$) have been used in a number of numerical simulations published in the literature [36, 8, 91]. Slight differences in the time-averaged bed height can be observed for both simulations in Figures 3.15(d-e). However the 'degree of' agitation of this system can be measured by analyzing the pressure drop fluctuations and the correspond-

ing power spectra density, as shown in Figures 3.16(b) and (c). In Figure 3.16(b), plotted during the first 7 seconds of the simulation, larger pressure fluctuations are observed for case 2d (e_{pp}=0.90), due to more vigorous bubbling resulting from greater kinetic energy dissipation [103]. Similarly, from the power spectra densities, Figure 3.16(c), larger amplitudes are observed for this case. However, the dominant frequency obtained for case 2d is smaller than case 2a, although a similar PSD profile, i.e., appearance of peaks, is observed in both cases. The PSD presented in Figure 3.16(c) is related to the last 20 seconds of simulation after stationarity was reached.

3.5 Conclusions

This work investigated the heat transfer models in monodisperse gas-solid fluidization. The numerical simulations were performed using CFD code, *FLUIDITY* which solves the two-fluid granular temperature equations using an Eulerian-Eulerian approach. Although the numerical results obtained from the standard and the kinetic approaches are very similar, the kinetic approach was preferred as it is consistent with the overall two-fluid granular temperature model. In addition, heat transfer coefficients calculated from the numerical results match well with some experimental results obtained from the literature.

In order to validate the model presented in this work, a simplified thermal energy equation was analytically solved. The exponential solution obtained from this simple model compared well with the numerical solution obtained from a long-term simulation regarding the cooling of a hot fluidized bed. The results of this simulation improved the confidence in the overall model.

Power spectra densities obtained from voidage fluctuations throughout the domain revealed that although different effective solid thermal conductivity correlations led to similar heat transfer coefficients, the dynamics were different due to the model sensitivity to energy dissipation. Indeed, energy dissipative parameters, such as friction coefficient and wall-particle and particle-particle restitution coefficients, as they play an important role in the overall fluidization behavior, were also investigated. Lower particle-particle restitution coefficients, i.e. more inelastic collisions, led to more vigorous fluidization,

as shown by the time-averaged bed height, pressure fluctuations and PSD of voidage fluctuations.

Chapter 4

Heat Transfer Mechanisms in the Wake of Bubbles

In this chapter[1], the two-fluid granular temperature model is used to investigate the heat exchanged between a heated wall and a gas-solid fluidized bed. Numerical simulations were performed in 2-D and 3-D fluidized beds using a solid phase effective thermal conductivity correlation based on granular temperature. The heat exchange in the bubbles' wake is investigated by tracking the train of bubbles which rise along the heated wall. Large heat transfer coefficients were obtained in the rear wake region of bubbles due to relatively larger granular temperature there and intense particle circulation.

[1]This chapter was submitted for publication in the International Journal of Heat and Fluid Flow: J. L. M. A. Gomes, C. C. Pain, C. R. E. de Oliveira, A. J. H. Goddard (2003), *A Two-Fluid Model Investigation of Heat Transfer in the Wake of Bubbles in Gas-Solid Fluidized Beds*

4.1 Introduction

Gas-solid fluidized beds have excellent heat transfer rates with internal surfaces due to the strong mixing. These properties make fluidized beds an attractive proposition for many industrial processes [13, 4]. They are currently used in separation, classification, drying and mixing of particles, chemical reactions and regeneration processes. In this work, the complete field descriptions, provided by the two-fluid model, were used to obtain more accurate fluidized beds heat transfer predictions than those calculated from purely experimentally-obtained correlations. The modelling has been conducted using the finite-element based CFD code FLUIDITY [78, 11, 100].

Fluidized beds are perhaps best known for their use in fluid catalytic cracking (FCC) processes, where 'heavy fractions' of oil (i.e., hydrocarbons of high molecular weight), are broken up into lower molecular weight fractions by the action of a catalyst [18]. In FCC units a large quantity of feedstock is used in fluidized bed reactors producing valuable chemicals. In the production of such chemicals, a mixing of exothermic and endothermic (mainly due to the catalyst regeneration) reactions take place, therefore gas-solid heat transfer mechanisms play an important role in the efficiency of FCCU's. Thus the optimization of the parameters used in fluidization processes has received a great deal of attention from the scientific community [29, 8].

Fluidization is defined as the process by which solid particles or liquids (either homogeneous or heterogeneous) are transformed into a fluid-like state via suspension in a fluid (gas or liquid) [4]. This work focuses on gas-solid fluidization in which the gas phase is assumed to behave as an ideal gas in thermodynamic equilibrium. In this case, as the inlet gas velocity reaches the so-called bubbling velocity (u_{mb}), bubbles start to rise through the bed, enhancing mass and heat transfer rates by the intense mixing and the increasing of the superficial contact areas. In addition, for gas-solid fluidization, granular particles move downward in the wall regions and improve the gas-particle mixing by the formation of vortices in the lower region of the bed as reported by Pain *et al.* [11] and by Wirth [12].

The two-fluid model (TFM) assumes both phases are interpenetrating continua. This requires additional closure laws to describe the rheology of the particulate phase. These

closure laws are based, in this work, on the assumptions of the kinetic theory of granular flows. Comprehensive reviews about this subject can be found in [37, 38, 40]. Ding & Gidaspow [41] developed a model to predict the granular viscosity and stress for dry flows. They introduced the concept of granular temperature as a measure of the agitation of particles. Indeed, granular temperature provides a link between kinetic theory and traditional fluid mechanics.

In the literature review performed by Lim *et al.* [13] and Bi *et al.* [88], the hydrodynamics related to the granular flow has been extensively studied by a number of researchers, including [5, 38, 41, 8] which focused on the bubbling regime, dilute flows and kinetic theory. In addition, the thermal energy generation and diffusion throughout the bed has been widely investigated, both experimentally and theoretically. Yates [89] produced a review of the most important works concerning the influence of temperature and pressure on the hydrodynamics of gas-solid fluidized beds. Molerus *et al.* [61, 57] investigated the global heat transfer due to convective mechanisms. They proposed a set of empirical correlations for the global heat transfer coefficient as a function of the Archimedes number, and for the radiative heat transfer coefficient in granular flows. Wirth [12] investigated experimentally the heat transfer between the walls and dilute flow (see also [106]). Sunderesan & Clark [62] measured the heat transfer coefficient to granular flows from a single cylinder and from a bank of heated cylinders. They investigated the presence of a stagnant zone in the top region of the cylinders due to the low superficial velocities. Gunn [56] measured the interphase heat transfer between particles and fluidizing gases in fixed and fluidized beds and suggested an empirical correlation for the Nusselt number in such beds.

Kuipers *et al.* [63] and Syamlal *et al.* [86] investigated numerically the heat transferred from a heated wall into the bed, and compared some of the results with experiments and with penetration theory. In addition, the influence of the bubble wakes on thermal energy transfer was also studied. In both works, the influence of particle collisions on the heat transfer, and in particular on the diffusion coefficient were neglected. However, Schmidt & Renz [34, 35] used correlations derived from the kinetic theory to calculate the effective thermal conductivity. These correlations were developed by Natarajan *et al.*

[68] (see also [66, 64]) using the analogy of between gas molecules collisions and inelastic collisions in dense granular flows. Schmidt and Renz simulated a lab-scale fluidized bed, working in bubbling regime, with an immersed heated cylinder. They performed a few numerical simulations and calculated the heat transfer coefficients. Their results were compared with experimental results due to Sunderesan & Clark [62]. In addition, some simulations using a standard correlation for the effective thermal conductivity, as used by Kuipers *et al.* [63], were also performed and the results were compared with those obtained using a kinetic-based correlation.

In this work, the two-fluid granular temperature model was used to investigate the heat transfer in 2-D and 3-D gas-solid fluidized beds. In order to investigate the heat exchanged between the heated surface and the bed, the following fields were calculated from the set of conservative equations: solid volume fraction, granular temperature, gas and solid phase temperatures and velocity components for each phase. The thermal conductivity of the solid phase is obtained from a granular temperature-based function and interphase heat transfer is calculated from the Gunn correlation. As the bubbles' wake plays an important role in the mixing and in the thermal diffusion, the rising bubbles were tracked and the heat transfer coefficients in the rear of the bubbles were calculated.

In Section 4.2, the heat transfer mechanisms between a heated wall and the gas-solid flow are investigated in numerical simulations conducted in 2-D fluidized beds. In this case, we focused on the study of the heat exchanged in the bubbles' wake. In addition, the voidage distribution across the emulsion shells around the bubble are carefully investigated in Section 4.3. Finally, 3-D fluidized beds, with geometry similar to those investigated in Section 4.2, are studied in Section 4.4.

4.2 2-D Numerical Simulations

In this section, a numerical investigation of the thermal energy transferred from a heated wall to the bed was performed in a gas-solid fluidized system. By tracking the rising bubbles along the wall region, the heat transfer coefficient was calculated and the contribution from the bubbles' wake investigated.

In the 2-D simulations, glass beads, with a diameter of 500 μm, are fluidized by air, which enters in the domain with an inlet velocity of 75 cm.s^{-1} and at 20^{o}C and atmospheric pressure. The simulated fluidized bed, which is shown in Figure 4.1(a), is 67.00 cm high and 18.50 cm wide. Both phases are initially at room temperature and the wall temperature is 100^{o}C. Physical properties of both phases are described at Table 3.1.

The boundary conditions can be summarized as follows: at the top of the domain, no normal flow and zero shear stress conditions were applied to the solid phase, whereas for the gas phase, zero shear stress was applied. This allows the gas to leave the domain unhindered, the solid phase, however must not leave the bed. In the vertical walls, a shear stress was prescribed, obtained from Blasius' equation [101] with a length scale equal to the static height of the bed. Wall boundary conditions for the solid phase described in [80, 78] were also used in the simulations described in this work. A summary for the boundary and initial conditions are outlined at Table 4.1.

In order to achieve a high numerical resolution in the wall region, an exponential mesh was used in this region (14.50$\leq$X$\leq$18.50 cm), whereas in the remainder of the domain a regular mesh was applied. Exponential mesh was also applied to the y-axis beginning from the free surface (Figure 4.1(b)). This simulation was performed over 25 seconds.

A number of researchers worldwide [11, 63] have reported the enhancement of the heat and mass transfer in the bubbles' wake, due to the intense mixing in this region. The rising bubbles yield a large solid particle replacement in the rear of the bubble which enhance solid circulation. Hence, fresh and 'cold' particles are dragged into the rear of the bubbles and the temperature gradient between 'cold and hot' particles is risen. Figure 4.2 shows the solid volume fraction (left-hand side) and heat transfer coefficient calculated along the heated wall. As bubbles rise in the vicinity of the wall, the heat transfer coefficient is enhanced in the rear of the bubble region, as can be clearly observed in the two large bubbles presented in Figures 4.2(a-d).

Figures 4.3 (a-d) show four snapshots, drawn at every 0.05 seconds, of the solid volume fraction distribution (left-hand side) and the gas temperature. Higher temperatures can be observed in the rear region of some of the bubbles which are rising in the vicinity of the wall. While these bubbles are rising, coalescing and breaking up, thermal energy is

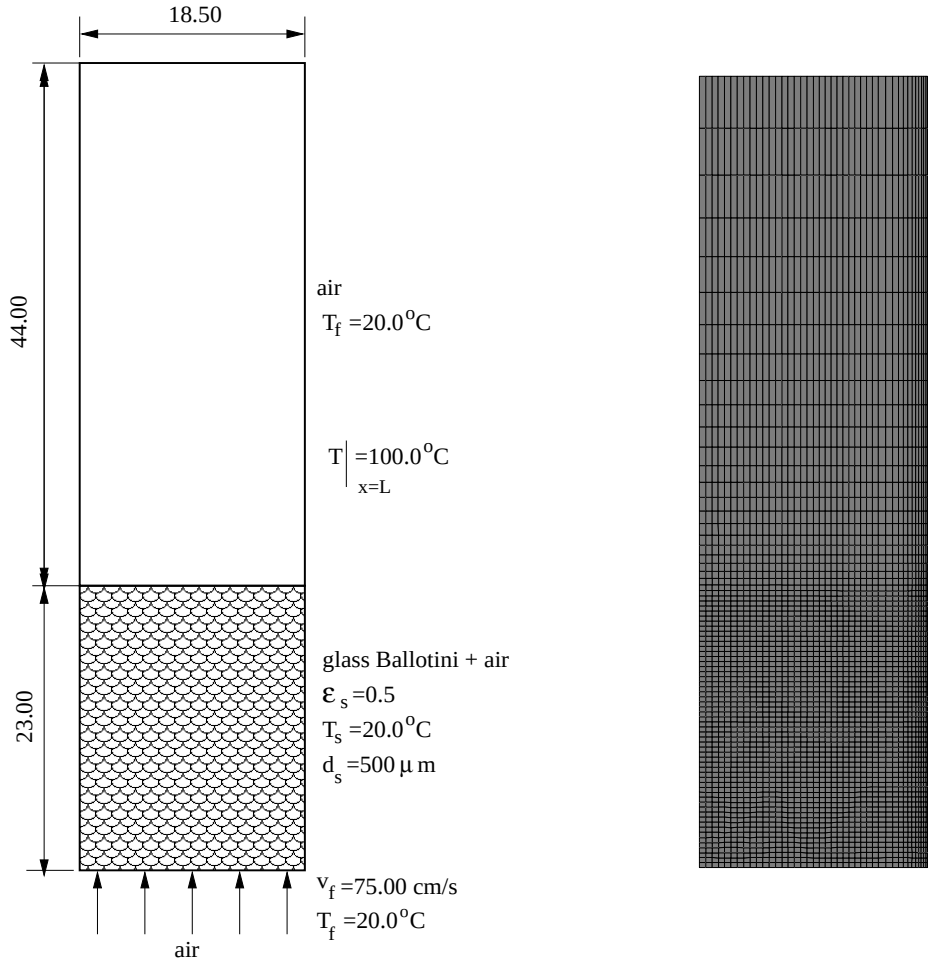

(a) Schematic (b) Mesh

Figure 4.1: (a) Schematic configuration of the simulated fluidized bed. All dimensions in cm. (b) Mesh used to discretise the domain in a 2-D cartesian geometry. There are 3360 nodes in 3239 elements. A fine mesh was applied to the r.h.s. of the domain from $14.50 \leq X \leq 18.50$ cm to resolve the heat exchange with the wall - the smallest element next to the wall is 0.09 cm wide.

(a)	Inlet gas velocity	$v_f\,(x, y = 0, t)$=0.75 m.s^{-1}
(b)	Initial ε_s	0.50
(c)	Initial gas and solid phase velocities	$v_s\,(x, y, t = 0)$=0.0 m.s^{-1} $v_f\,(x, y \neq 0, t = 0)$=0.0 m.s^{-1}
(d)	Initial gas and solid temperatures	$T_f\,(x, y, t = 0)$=20.0 ^{o}C $T_s\,(x, y, t = 0)$=20.0 ^{o}C
(e)	Solid flow in the top	$v_s\,(x, y = L, t)$=0.0 m.s^{-1}
(f)	Solid stress in the top	$\tau_s\,(x, y = L, t)$=0.0 N.m^{-2}
(g)	Particle-particle restitution coefficient	e_{pp}=0.97
(h)	Wall-particle restitution coefficient	e_{wp}=0.90
(i)	Friction coefficient	$\overline{\mu}$=0.10

Table 4.1: Initial and boundary conditions used in the numerical simulation reported in this section.

diffused through the bed, making the temperature more uniform. Moreover in the bubbles' wake, a region where fresh and 'cold' material circulates, the heat transfer coefficient is larger (Figure 4.3 (e)). By comparing the snapshots with this figure at a height between 20-25 cm, one can see that while a large bubble is rising, near the wall region, the heat transfer coefficient increases sharply and then decreases to a level similar to the first snapshot. The thermal diffusion throughout the bed is enhanced by the train of rising bubbles which produce a large particle flow reorientation near the wall, as reported by Stappen *et al.* [44]. Hence, as the solid 'cold' particles fall and flow downwards near the wall and crash with the train of rising 'hot' bubbles and particles, the heat transfer coefficient is enhanced due to the large temperature fluctuations as shown in Figure 4.4 (a). The thermal diffusion through the bed can be observed by comparing temperature time series obtained from two detectors located near the wall and at the center region , Figure 4.4(a) and (b), respectively. As the thermal source is located in the wall, larger temperature amplitudes are observed in its vicinities than in the center region. Furthermore, although the gas temperature in the wall region rose sharply in the beginning of the simulation, the

temperature at the center region was nearly constant in the first 5 seconds and increased smoothly afterwards.

The velocity vectors of both phases at 16.77 seconds (see Figure 4.3 (d)) are shown in Figures 4.5 (a-b). In these figures, particles are falling near the wall and swirling near the bottom corners as they crash against the upward gas flow (see [11]). In addition, solid circulation can be observed in the rear of some bubbles.

The main heat transfer contribution in granular flows is due to the solid phase. However, in highly packed systems, the heat transfer decreases due to the low granular temperature produced in such systems. Voidages, and bubbles in particular, enhance the heat transfer by increasing the free mean path between the particles which increases the particle collision rate. In addition, the circulation produced by bubbles replaces hot particles by cold particles.

In this work, the heat transfer coefficient is calculated based on the boundary conditions:

$$\kappa \nabla T = H_T \left(T_w - T_{susp} \right) \tag{4.1}$$

The heat transfer coefficient is obtained from the wall, which is held at 100^{o}C:

$$H_T = \left(\varepsilon_f \kappa_f \right) \left| \frac{\left(\dfrac{\partial T_f}{\partial n} \right)\Big|_w}{T_w - T_{susp}} \right| + \left(\varepsilon_s \kappa_s \right) \left| \frac{\left(\dfrac{\partial T_s}{\partial n} \right)\Big|_w}{T_w - T_{susp}} \right| \tag{4.2}$$

where T_{susp} is the temperature of the suspension along the heated surface. Generally the temperature of the fluid and solid phases are very similar, therefore the simple averaging of these temperature fields next to the wall was used to calculate T_{susp}. Therefore, the heat transfer coefficient was calculated from the temperature gradient between the suspension and the wall, accounting for a thermal boundary layer at the wall. Figures 4.6-4.7 show the solid volume fraction and heat transfer coefficient (H_T), respectively, at several detectors along the wall during 22 seconds of simulation. At a height of 1.0 cm above the distributor, Figures 4.6-4.7(a), several small bubbles are produced and strong solid volume fraction fluctuation can be observed. Such large mixing of cold gas and cold and hot particles, which descend along the wall region, increases the heat transfer coefficient to approximately 530 W.m^{-2}.K^{-1}, as shown in Figures 4.7(a) and 4.9. From 5.0 cm to

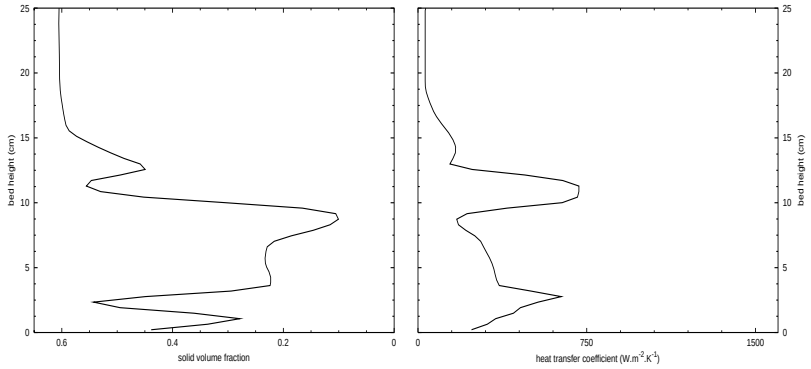

(a) t = 1.60 seconds

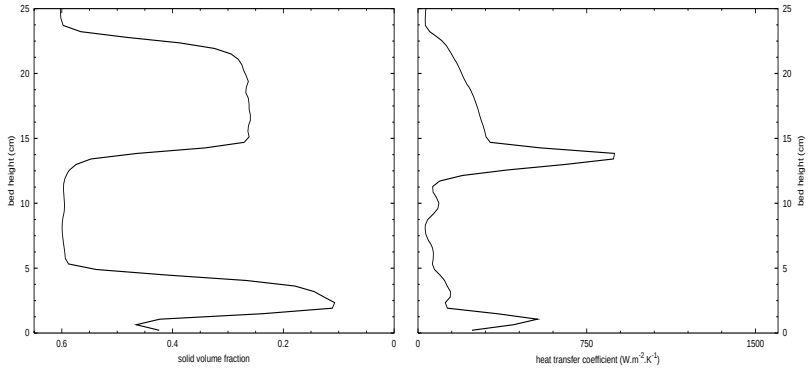

(b) t = 1.87 seconds

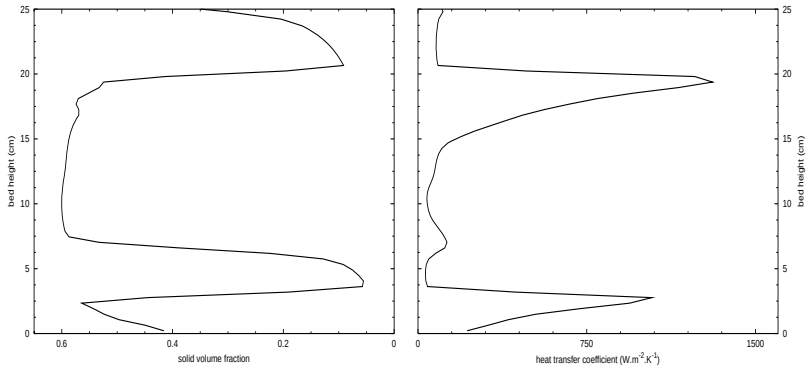

(c) t = 2.00 seconds

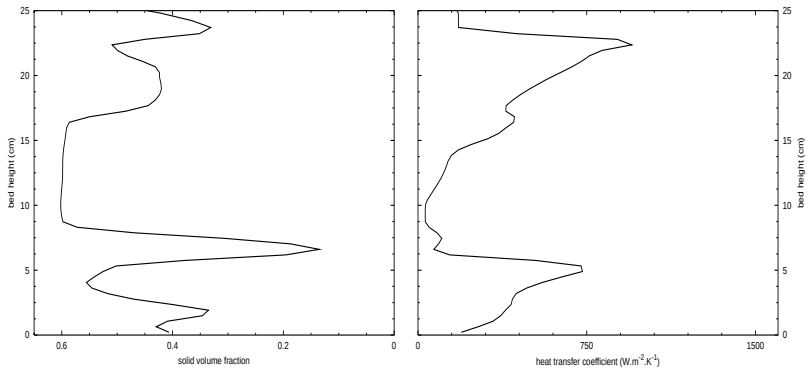

(d) t = 2.10 seconds

Figure 4.2: Flow past a heated wall: solid volume fraction (left-hand side) and heat transfer coefficient against bed height at (a) 1.60, (b) 1.87, (c) 2.00 and (d) 2.10 seconds. Note that the solid volume fraction axis increases from right to left.

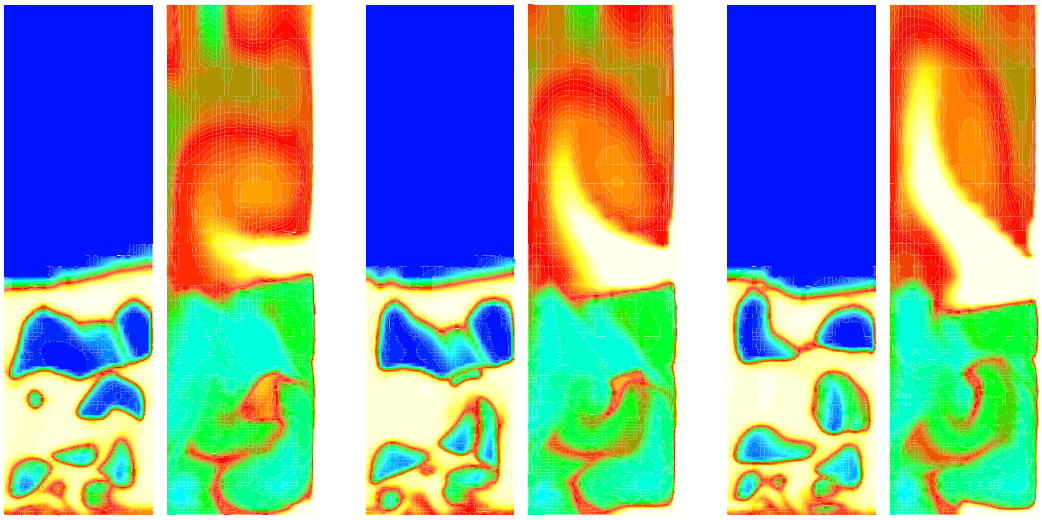

(a) t = 16.62 sec. (b) t = 16.67 sec. (c) t = 16.72 sec.

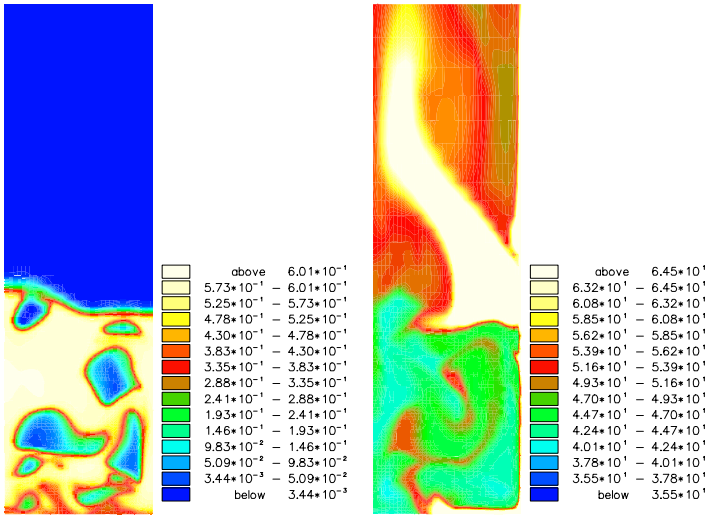

(d) t = 16.77 sec.

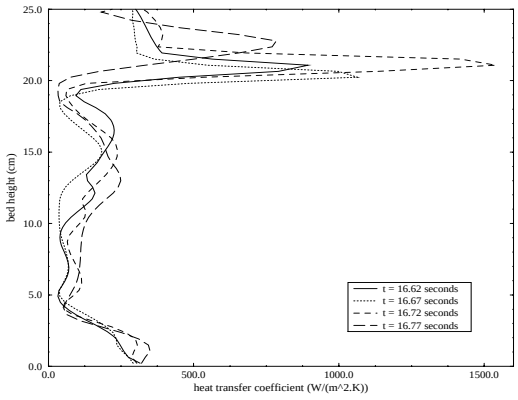

(e) heat transfer coefficients against bed height

Figure 4.3: Flow past a heated wall: solid volume fraction (right-hand side) and gas temperature at (a) 16.62, (b) 16.67, (c) 16.72 and (d) 16.77 seconds. Figure (e) shows the heat transfer coefficient at these times 25 cm along the heated wall.

17 cm above the distributor, the H_T varies from 135 to 280 W.m^{-2}.K^{-1} due to packing conditions, which produces low granular temperatures, as shown in Figures 4.8 (a,b). In larger heights, strong voidage fluctuations (Figures 4.6(d,e)) yield to larger granular temperature (Figures 4.8(c,d)) and heat transfer coefficients (Figures 4.7(d,e)). Such larger voidage fluctuations increase the distance between the particles and the momentum transferred by particle collisions. The heat transfer coefficient in this region varies from 280 to 1200 W.m^{-2}.K^{-1}. In the upper region, as the solid concentration and the granular temperature decrease and vanish (Figures 4.6(f-h) and 4.8(e,f), respectively) the heat transfer coefficient also decreases, from 360 to 2 W.m^{-2}.K^{-1}. At a height of 38.0 cm above the distributor, H$_T$ reflects solely the gas phase. The time-averaged heat transfer coefficient is 427 W.m^{-2}.K^{-1}.

In order to validate this time-averaged result, a simplified method which takes into account the thermal energy transferred through the boundary layer was applied. As the thermal energy is mainly conducted by the emulsion phase, a simplified thermal energy equation (Equations 2.5 and 2.6) for the solid phase was used to represent the thermal flux in the wall region:

$$\frac{\partial}{\partial t}\left[T_s\left(m_s C_s + m_f C_f\right)\right] - \frac{\partial}{\partial x}\kappa\frac{\partial T}{\partial x} = 0 \tag{4.3}$$

with the following boundary condition

$$\kappa\frac{\partial T}{\partial n} = H_T\left(T_w - T\right) \tag{4.4}$$

where m_k and n are the mass of phase k and normal vector outward the surface, respectively. Assuming the domain along the wall region, the time-averaged heat transfer coefficient is 517 W.m^{-2}.K^{-1}. However, the correlation reported by Kunii & Levenspiel [4] results in heat transfer coefficient equal to 379 W.m^{-2}.K^{-1}. The similarity between the results obtained from numerical simulations (Equations 4.2 and 4.3) and from a global heat transfer correlation, enhances the confidence in the overall model as it does not rely on purely empirical expressions to calculate the heat transfer coefficient. Therefore, the simplified model expressed by Equations 4.1 and 4.2 may be used to calculate the heat transfer in long-term 3-D simulations (Section 4.4).

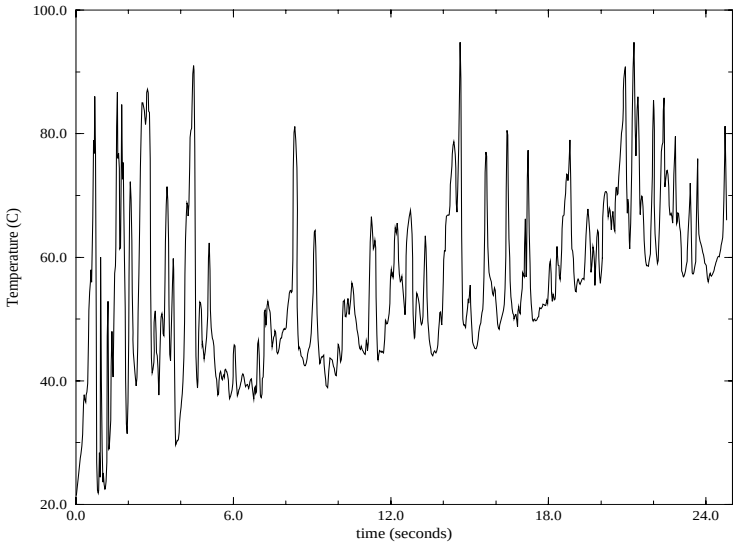

(a)

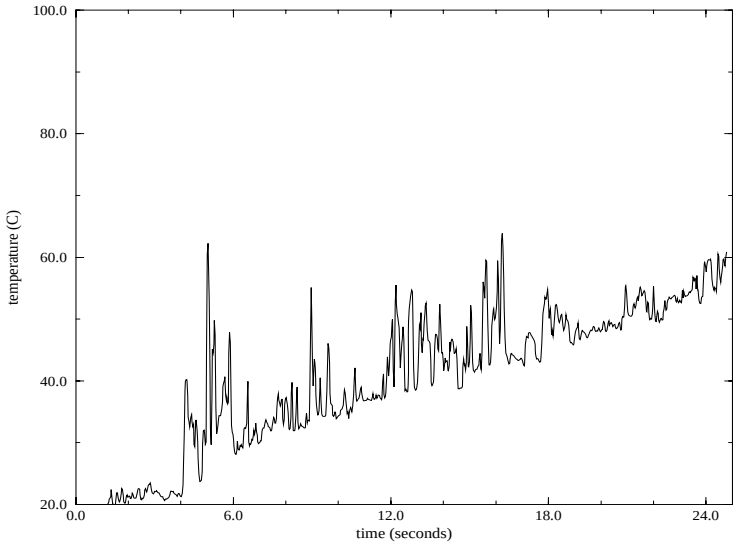

(b)

Figure 4.4: Flow past a heated wall: gas phase temperature fluctuations in a sensor located 10cm above the distributor and (a) 0.15 cm and (b) 9.25 cm away from the wall.

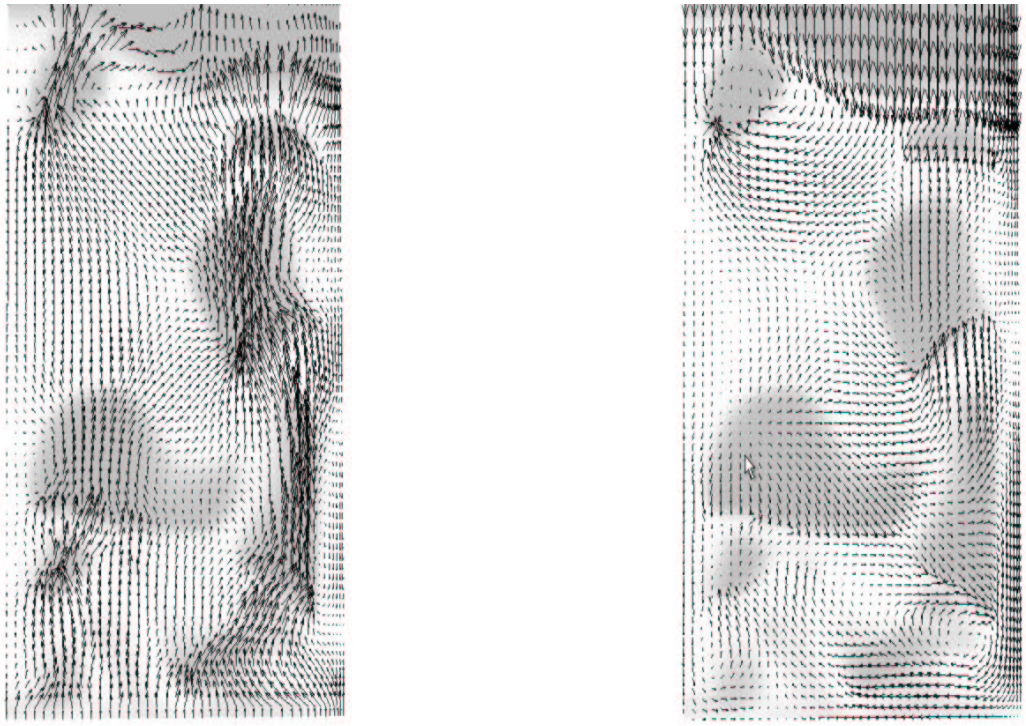

(a) gas phase (b) solid phase

Figure 4.5: Flow past a heated wall: velocity vectors of the (a) gas and (b) solid phases at 16.77 seconds (Figure 4.3(d)). The maximum velocities for the gas and the solid phase are 521 and 225 cm.s^{-1}, respectively. Only 31 cm of the height is shown.

4.3 Investigation of the Emulsion Shells Around the Bubbles

As a bubble arises enhancing the bed mixing, an emulsion shell surrounds it exchanging heat and mass with the neighborhood. Such emulsion shell has attracted a great deal of attention from the scientific community [107, 5, 81, 82, 108] as the heat and mass transfer mechanisms with the emulsion phase have not been fully understood. Pressure fluctuations of a labscale fluidized bed were used by Fan [108] to investigate the particle concentration in both, the emulsion cloud in the front region of the bubbles and in the bubbles' wake. According to them, the solid concentration in the bed is, in a statistical sense, lower than in the bubble's wake and is higher than that in the cloud. However, when two bubbles collide, the solid concentration in the wake region decreases while a emulsion cloud, which surrounds the two bubbles, expands as they coalesce.

Experiments carried by Yates *et al.* [107] using X-ray images in air-fluidized beds of powder belonging to Geldart group A and B, revealed an exponential decay curve of solids concentration across the emulsion shell. The concentration of solids decreases smoothly in the outer region of the emulsion shell and sharply in the inner region. This behavior is probably due to unsteady-state bubble formation in the distributor.

In order to study the solid concentration behavior in emulsion shells, a large bubble (Figure 4.10) was investigated. As shown in Figure 4.11(a), at the height of 15 cm above the distributor (i.e., in the center region of the large bubble), the voidage rises from 0.53, at the wall region, to 0.95, at a distance of 0.90 cm from the r.h.s. wall. However, in the bottom region of the bubble, at a height of 7.62 cm from the distributor, the voidage rises smoother than in the center region of the bubble. In fact, as this height corresponds to the bubble's wake, the voidage increases from 0.42 to 0.68, the particle collisions occur more often than inside the bubble, which can be noticed from the solid velocity and the granular temperature, Figures 4.10 (c) and 4.11(b,c). In the center of the bubble (i.e., h=15.0cm), a low number of particles may collide with lower energy, described by the granular temperature, however at the bubble's wake (i.e., h=7.62cm), particles are dragged and 'packed' at the emulsion shell. In such condition, due to a lower solid volume fraction

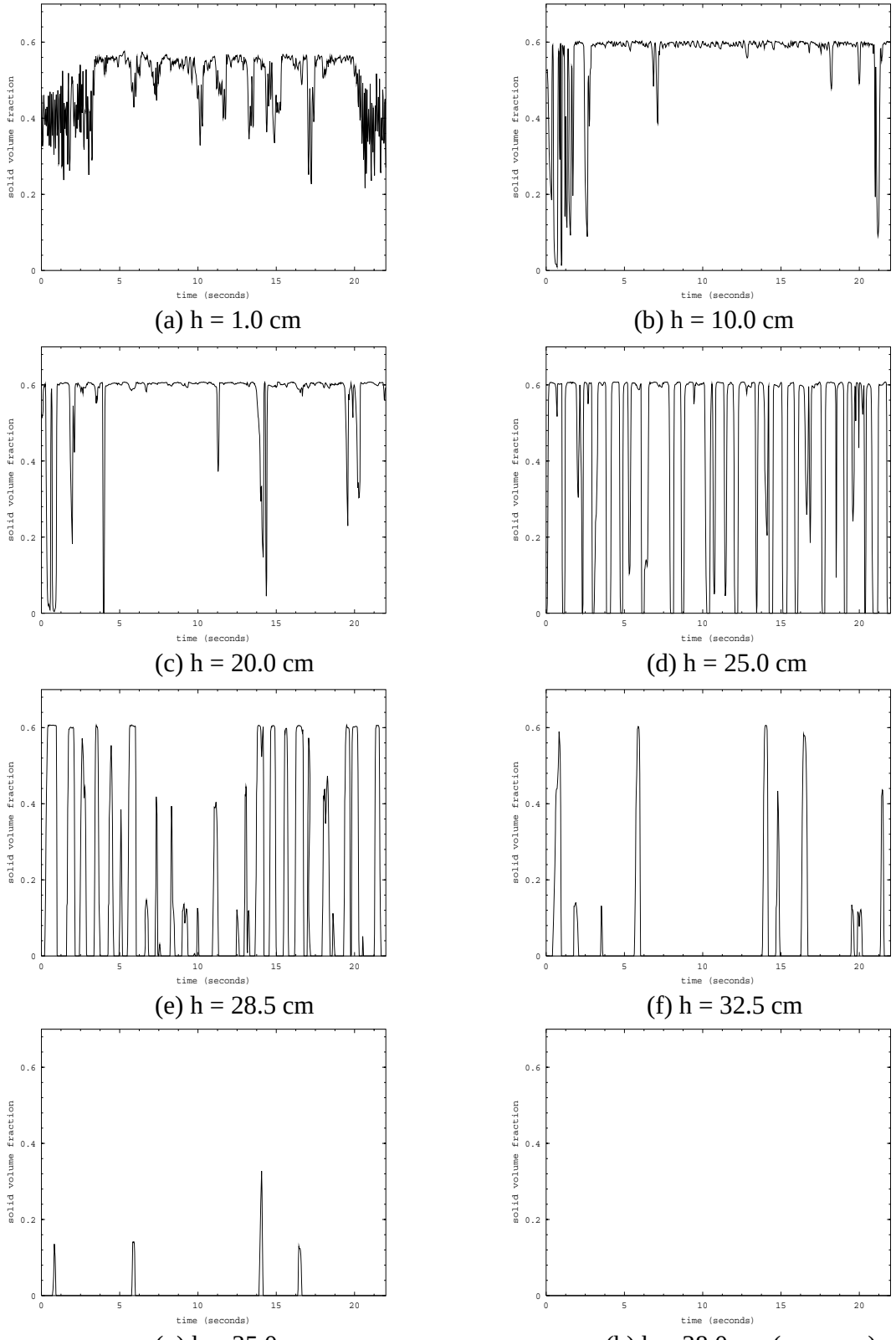

(a) h = 1.0 cm (b) h = 10.0 cm

(c) h = 20.0 cm (d) h = 25.0 cm

(e) h = 28.5 cm (f) h = 32.5 cm

(g) h = 35.0 cm (h) h = 38.0 cm (pure gas)

Figure 4.6: Flow past a heated wall: solid volume fraction fluctuations at (a) 1.0, (b) 10.0, (c) 20.0, (d) 25.0, (e) 28.5, (f) 32.5, (g) 35.0 and (h) 38.0 cm above the distributor.

(in comparison in the whole bed) and larger solid velocities, energy is released due to solid collisions as shown in Figure 4.11(c).

Figures 4.12-4.14 show voidage, granular temperature and solid velocity along the y-axis at several distances from the r.h.s. wall. At d=0.10 cm, particles are falling with a relatively large 'packing' condition, $0.40 \leq \varepsilon_s \leq 0.58$, as shown in Figures 4.12(a) and 4.14(a). As the distance from the wall is increased, the large bubble can be observed through Figures 4.12(b-e), i.e., $1.0 \leq d \leq 4.0$ cm. Inside the bubbles, rising particles collide with falling particles as shown by Figures 4.14(b-e), however due to the low solid volume fraction, the granular temperature remains low, see Figures 4.13(b-e). Buyevich *et al.* [109] studied the voidage distribution around rising bubbles and reported a relationship between granular temperature, gas pressure and solid concentration. In addition, according to them, the voidage through the emulsion shell decays monotonically from a value of unity in the bubble void region to approximately 0.50 in the emulsion phase:

$$\varepsilon_g = \varepsilon_g^\star + \left(1 - \varepsilon_g^\star\right) \exp\left[-a\left(\frac{r}{R} - 1\right)^b\right] \tag{4.5}$$

where $\varepsilon_g^\star$ is the voidage in the undisturbed bed, *R* and *r* are the bubble radius and the radial dimension, respectively; *a* and *b* are fitting parameters. Collins [110] obtained a similar equation by fitting experimental voidage with $a = \frac{1}{15}$ and $b = -3$. Buyevich [109], however, used data obtained from the fluidization of different powders belonging to groups A and B of Geldart classification. They obtained $a = 1.5$ and $b = 1$, and in the present numerical simulation, we obtained $a = 7.2$ and $b = 1.0$. Their results were, however, achieved from detectors placed at several heights through the bed and did not take into account wall effects on the rising bubbles.

4.4 3-D Numerical Simulations

A 3-D numerical simulation was performed with similar geometry (18.50×18.50×67.00 cm), boundary and initial conditions as applied to the 2-D device, in which the temperature was maintained at 100 ^{o}C on one of the walls. Figure 4.15 shows six snapshots, taken every 0.05 seconds, of solid volume fraction (r.h.s.) and gas temperature distributions over 0.25 seconds of numerical simulation. In order to improve the visualization of

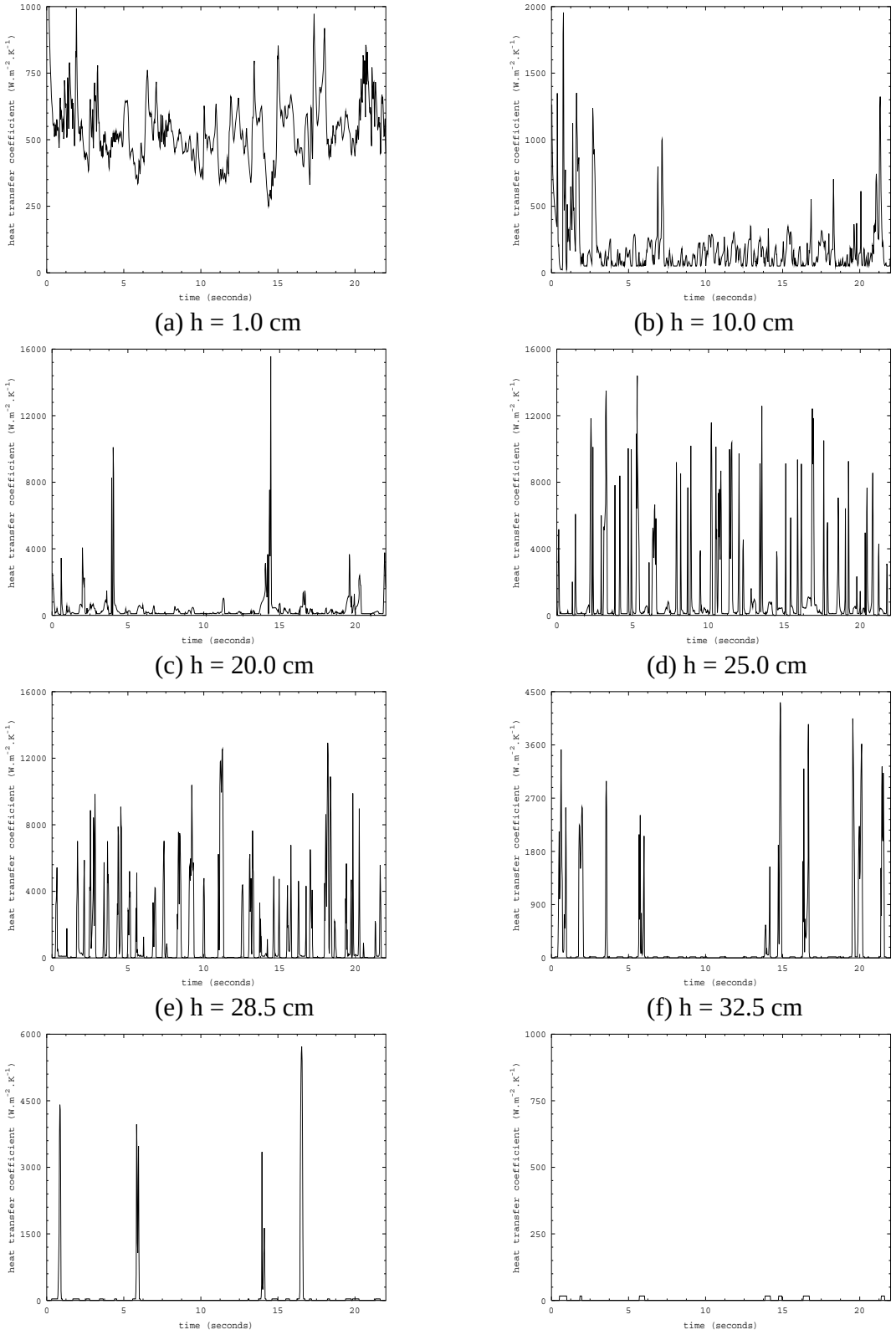

(a) h = 1.0 cm (b) h = 10.0 cm

(c) h = 20.0 cm (d) h = 25.0 cm

(e) h = 28.5 cm (f) h = 32.5 cm

(g) h = 35.0 cm (h) h = 38.0 cm (pure gas)

Figure 4.7: Flow past a heated wall: heat transfer coefficient ($W.m^{-2}.K^{-1}$) fluctuations at (a) 1.0, (b) 10.0, (c) 20.0, (d) 25.0, (e) 28.5, (f) 32.5, (g) 35.0 and (h) 38.0 cm above the distributor.

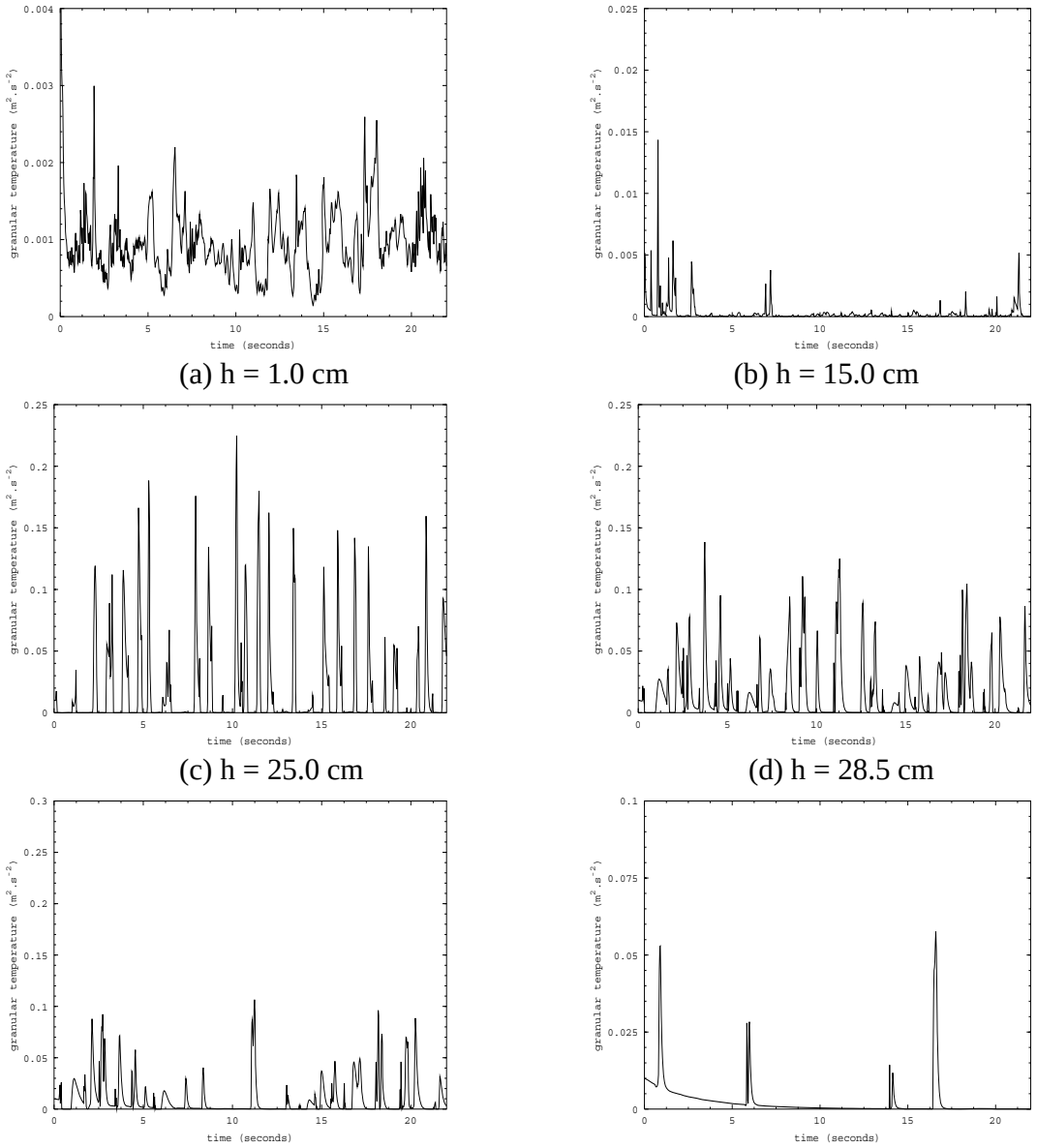

(a) h = 1.0 cm (b) h = 15.0 cm

(c) h = 25.0 cm (d) h = 28.5 cm

(e) h = 30.0 cm (f) h = 35.0 cm

Figure 4.8: Flow past a heated wall: granular temperature ($m^2.s^{-2}$) fluctuations at (a) 1.0, (b) 10.0, (c) 25.0, (d) 28.5, (e) 30.0, (f) 35.0 cm above the distributor.

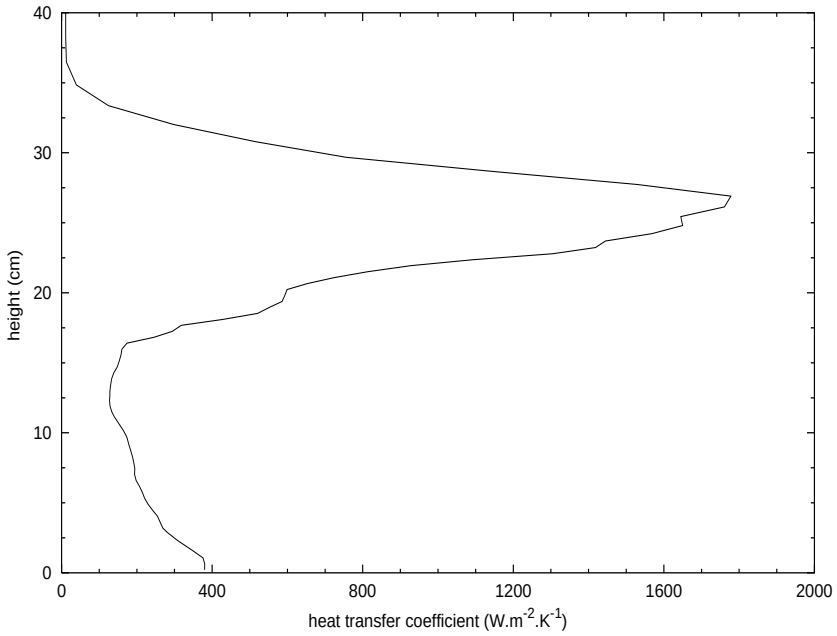

Figure 4.9: Flow past a heated wall: time-averaged heat transfer coefficient ($W.m^{-2}.K^{-1}$) against bed height.

rising bubbles, a slice 0.05 cm thick from the heated wall was removed (r.h.s. face) from Figures 4.15. As the large bubble rises in the corner of the domain, thermal energy is diffused throughout the domain and increases the average temperature. Isosurface maps of the solid volume fraction of Figure 4.15(f) were drawn and three large bubbles are shown in Figures 4.16. The two large bubbles in a restricted domain on vertical planes at distances of 3.0 and 1.5 cm from the nearest wall are shown in Figure 4.17. Usually large solid volume fractions lead to low granular temperature as the free mean path between particles decreases, however very low solid concentration does not lead to larger granular temperature, as the collision probability function is smaller. Therefore, higher granular temperatures are found around the bubbles and, in particular, in their wake (see Figures 4.17). Figure 4.16(b) shows the velocity vectors of the solid phase at a plane-cut near the wall. As there is a small number of particles inside the bubbles, random particle motion does not lead into a increasing in the number of collisions as shown in Figure 4.17(b), however in the rear region of the bubbles as vortices appear, Figure 4.16(b), larger number of collisions led to larger granular temperature, Figure 4.17(b). Indeed, a strong circula-

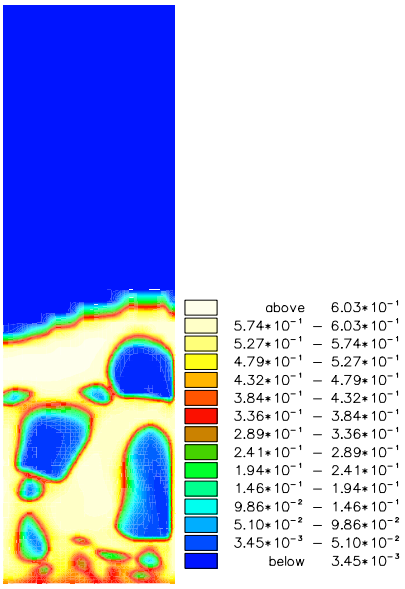

(a) solid volume fraction

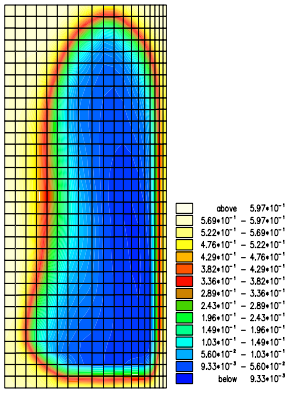

(b) solid volume fraction

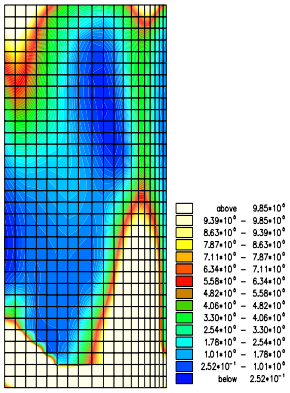

(c) granular temperature ($cm^2.s^{-2}$)

Figure 4.10: Flow past a heated wall: Snapshot of the simulated fluidized bed at 13.0 seconds (a). Detailed (b) solid volume fraction and (c) granular temperature distribution across the rising large bubble at the r.h.s. wall in detail.

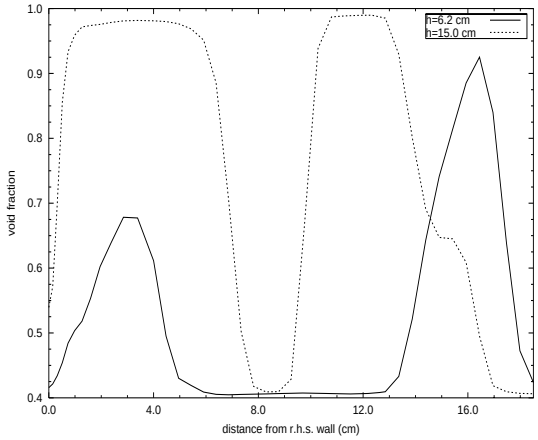

(a) void fraction

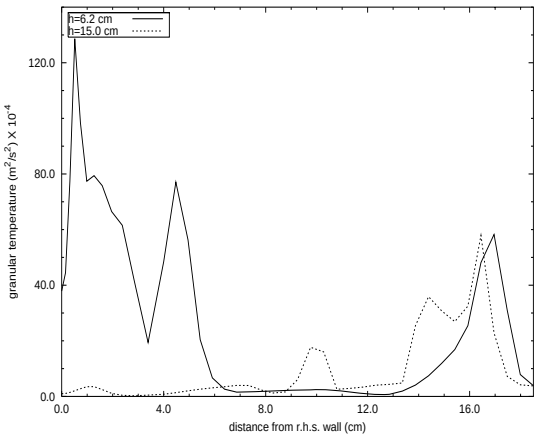

(b) granular temperature

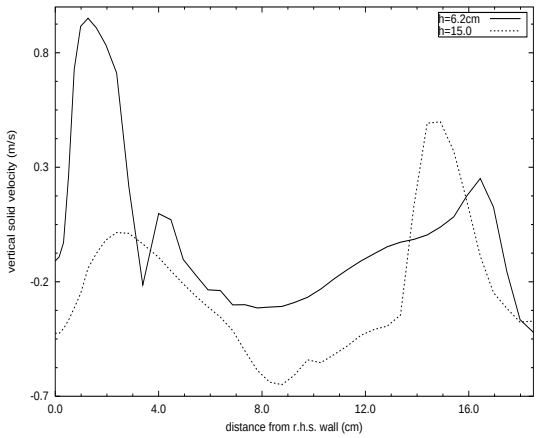

(c) vertical solid velocity

Figure 4.11: Flow past a heated wall: Void fraction, granular temperature (in $m^2.s^{-2}$) and vertical solid velocity (in $m.s^{-1}$) from the r.h.s. wall at 6.2 and 15 cm above the distributor. The data was obtained at 13.0 seconds of numerical simulation.

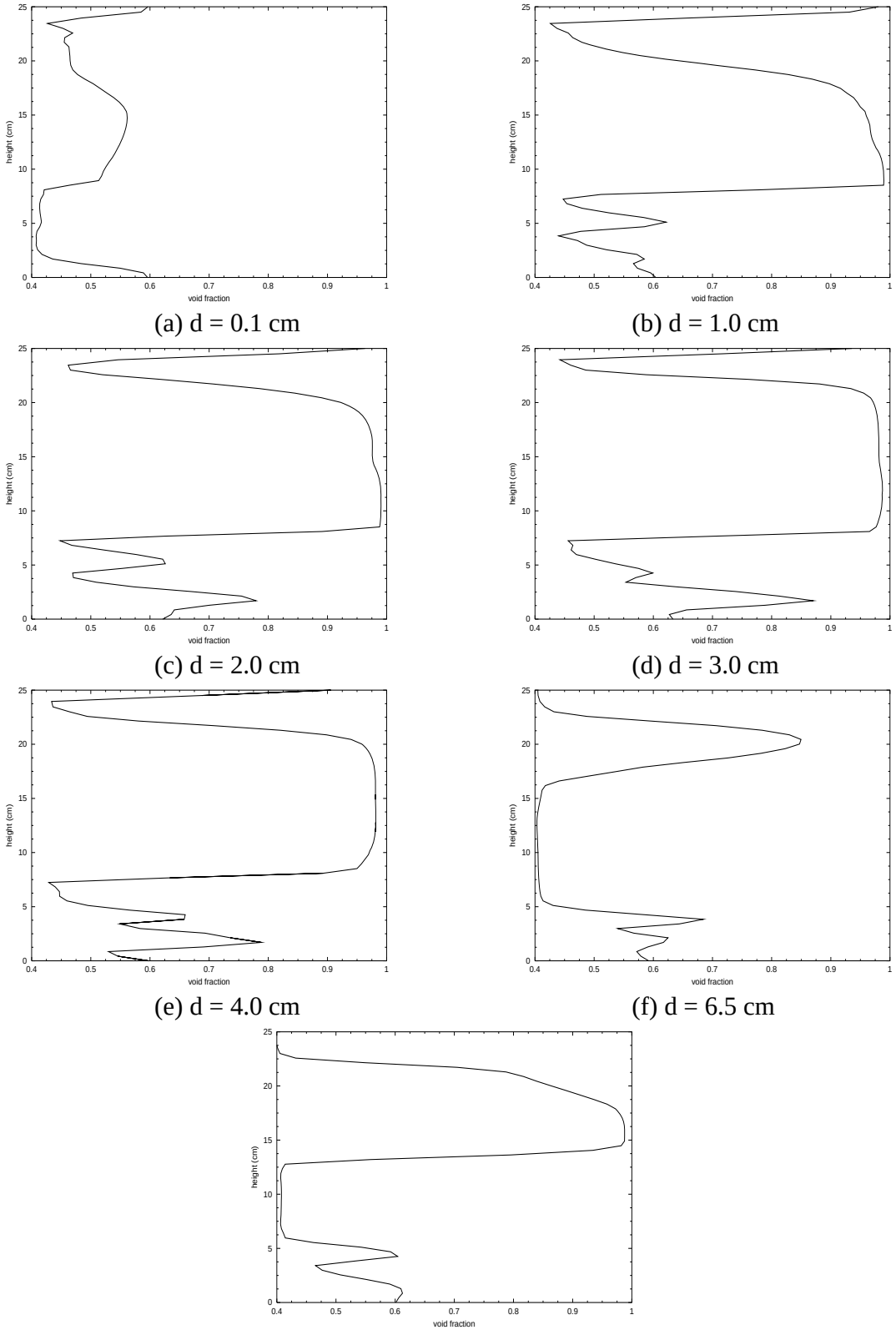

(a) d = 0.1 cm (b) d = 1.0 cm

(c) d = 2.0 cm (d) d = 3.0 cm

(e) d = 4.0 cm (f) d = 6.5 cm

(g) d = 11.0 cm

Figure 4.12: Flow past a heated wall: voidage along the y-axis at (a) 0.1 cm, (b) 1.0 cm, (c) 2.0 cm, (d) 3.0 cm, (e) 4.0 cm, (f) 6.5 cm and (g) 11.0 cm from the r.h.s wall. The data was obtained at 13.0 seconds of numerical simulation.

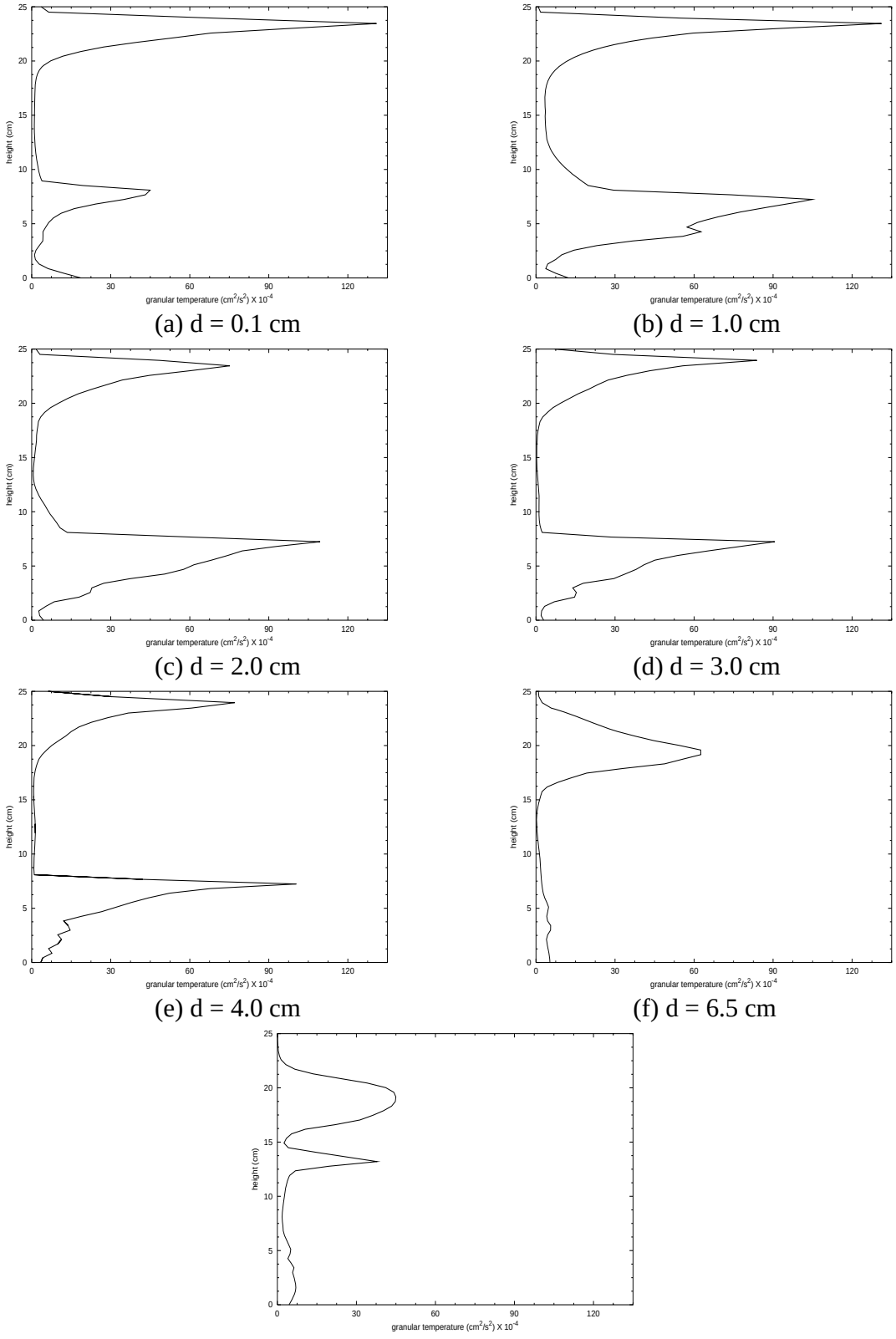

(a) d = 0.1 cm (b) d = 1.0 cm

(c) d = 2.0 cm (d) d = 3.0 cm

(e) d = 4.0 cm (f) d = 6.5 cm

(g) d = 11.0 cm

Figure 4.13: Flow past a heated wall: granular temperature ($cm^2.s^{-2}$) along the y-axis at (a) 0.1 cm, (b) 1.0 cm, (c) 2.0 cm, (d) 3.0 cm, (e) 4.0 cm, (f) 6.5 cm and (g) 11.0 cm from the r.h.s wall. The data was obtained at 13.0 seconds of numerical simulation.

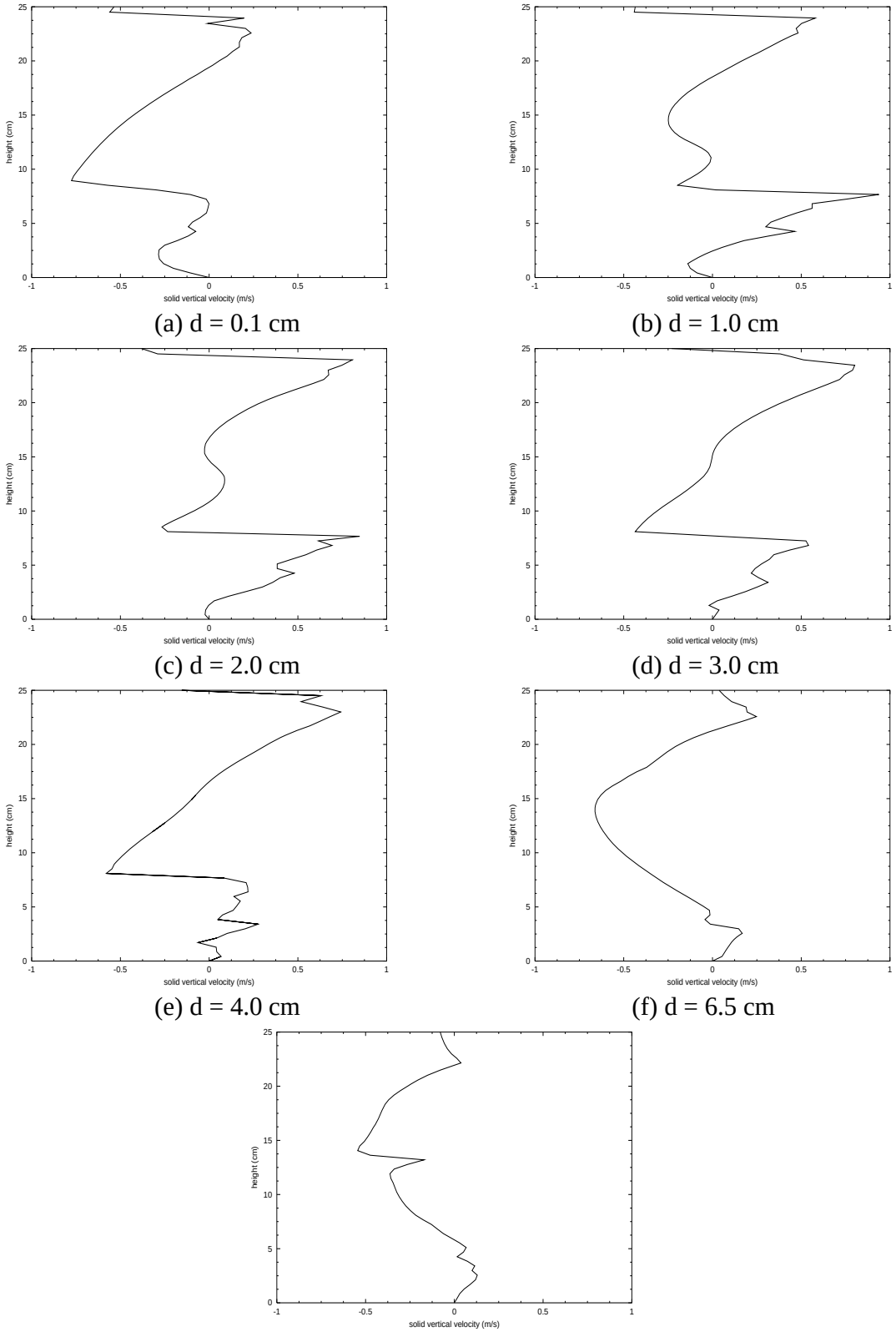

(a) d = 0.1 cm

(b) d = 1.0 cm

(c) d = 2.0 cm

(d) d = 3.0 cm

(e) d = 4.0 cm

(f) d = 6.5 cm

(g) d = 11.0 cm

Figure 4.14: Flow past a heated wall: vertical solid velocity (m/s) along the y-axis at (a) 0.1 cm, (b) 1.0 cm, (c) 2.0 cm, (d) 3.0 cm, (e) 4.0 cm, (f) 6.5 cm and (g) 11.0 cm from the r.h.s wall. The data was obtained at 13.0 seconds of numerical simulation.

tion of particles can be seen inside and in the bubbles wake, as particles move downwards in the wall region and dragged upward by the ascending gas flow.

As the bubbles rise along the heated wall, hot particles are displaced and thermal energy is diffused through the bed due to the strong mixing produced by the random motion of these bubbles. The train of rising bubbles helps making the temperature more homogeneous throughout the domain as the dynamics evolves in time. Such property can be observed in the three snap-shots shown in Figure 4.4 regarding the gas phase temperature during 20 seconds of numerical simulation. Although the gas temperature increases sharply in the vicinities of the heated wall, in the remaining of the domain, the temperature rises smoothly,as shown in the 2-D simulations (Figure 4.4). Two main reasons are responsible for such behavior: proximity of the heat source and the dynamics associated with the flow in the wall region, i.e., rising bubbles colliding with falling particles. Both reasons can be related to the packet renewal theory [54] in which fresh packets of particles replace hot packets in the emulsion phase due to the action of bubbles and gas streams in contact with the heated surface flowing through the packets. Figures 4.19 (a) and (b) show the gas temperature fluctuations in the wall region and 7.62 cm away from the wall, respectively, and at 4.31 cm above the distributor. The temperature rises rapidly in the wall region and as the dynamics evolve in time, it becomes smoother. Away from the wall, however, it took approximately 1.3 seconds for a temperature perturbance, i.e., for an abrupt rising of 18.0 ^{o}C in the gas temperature. In the central region of the bed $(5.0 \leq X \leq 13.0)$, Figures 4.4 (a) and (b), the temperature is fairly homogeneous, however it is colder than in the wall region. After approximately 20.59 seconds of numerical simulation, Figure 4.4 (c), the temperature in the whole domain is very homogeneous, oscillating from 82.0 to 95.0 ^{o}C.

By integrating the local heat transfer coefficient along the heated surface area and by averaging it over the time domain, a time-averaged heat transfer coefficient (Equation 4.2) of 449 W.m^{-2}.K^{-1} is obtained. However, using the empirical heat transfer correlation reported by Kunii & Levenspiel [4], H_T is 360 W.m^{-2}.K^{-1}. The time-averaged heat transfer coefficient obtained from 2-D (Section 4.2) and 3-D simulations are very similar suggesting that the important dynamics are captured by the numerical simulations. However long

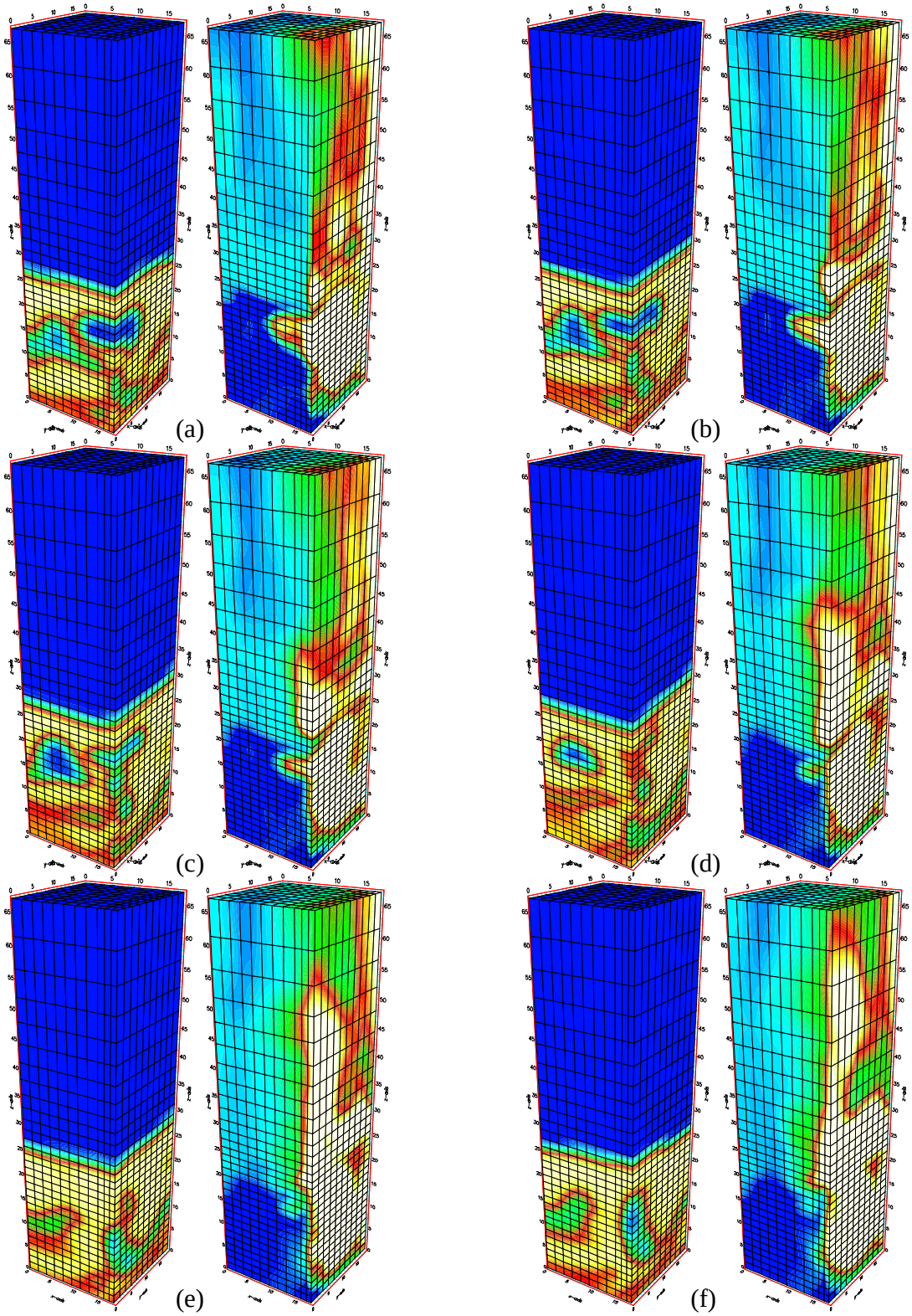

Figure 4.15: Flow past a heated wall - 3-D simulation: snapshots of solid volume fraction (r.h.s.) and gas temperature at (a) 2.36, (b) 2.41, (c) 2.46, (d) 2.51, (e) 2.56 and (f) 2.61 seconds. The r.h.s. face is at a distance of 0.05 cm from the heated wall, which has been removed. Legends for both phases are the same as those shown in Figure 4.3. There are 4576 nodes and 3720 elements.

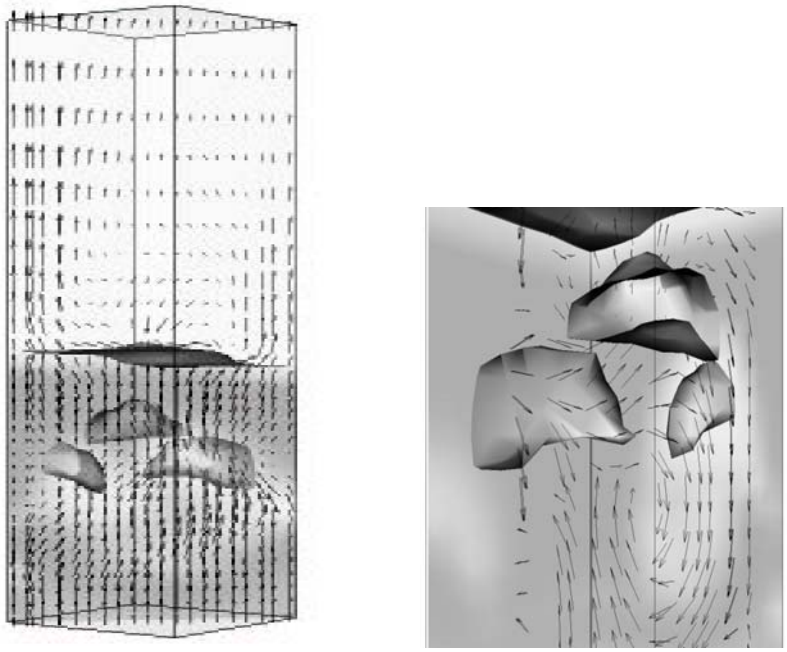

(a) (b)

Figure 4.16: Flow past a heated wall - 3-D simulation: snapshot at 2.51 seconds (Figure 4.15(d)) of particle concentration (showing three rising bubbles). Velocity vectors of the (a) gas phase and (b) a close view of the solid velocity vectors in a plane-cut near a bubble which is rising near the wall.

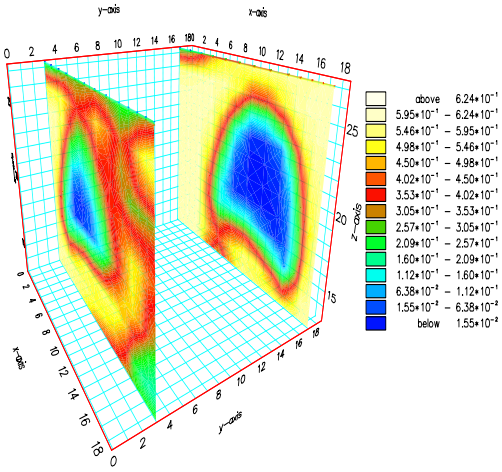

(a) solid volume fraction

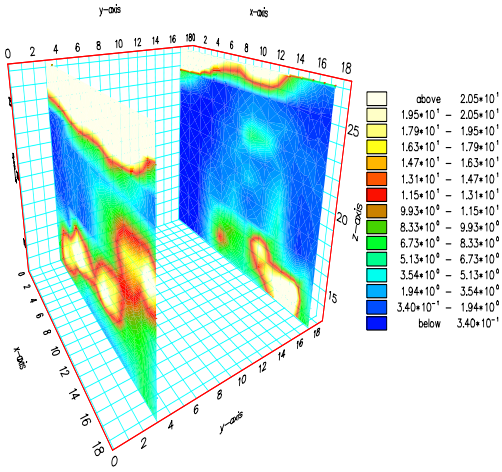

(b) granular temperature

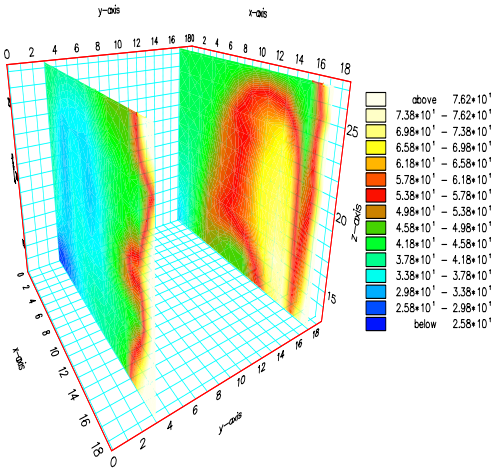

(c) gas phase temperature

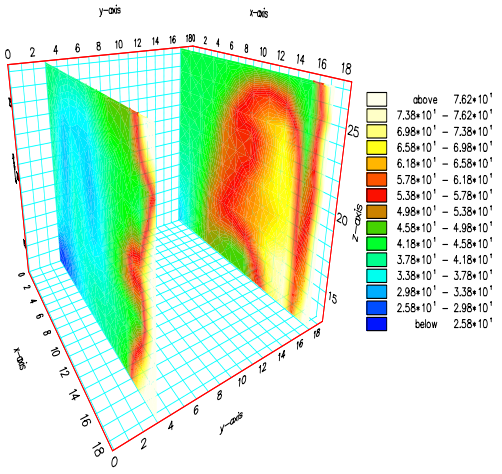

(d) solid phase temperature

Figure 4.17: Flow past a heated wall - 3-D simulation: the two large bubbles shown in Figure 4.16 are intersected and shown on vertical planes at a distance of 3.0 and 1.5 cm from the wall, respectively. The following fields are shown: (a) solid volume fraction, (b) granular temperature ($cm^2.s^{-2}$), (c) gas phase and (d) solid phase temperatures (^oC).

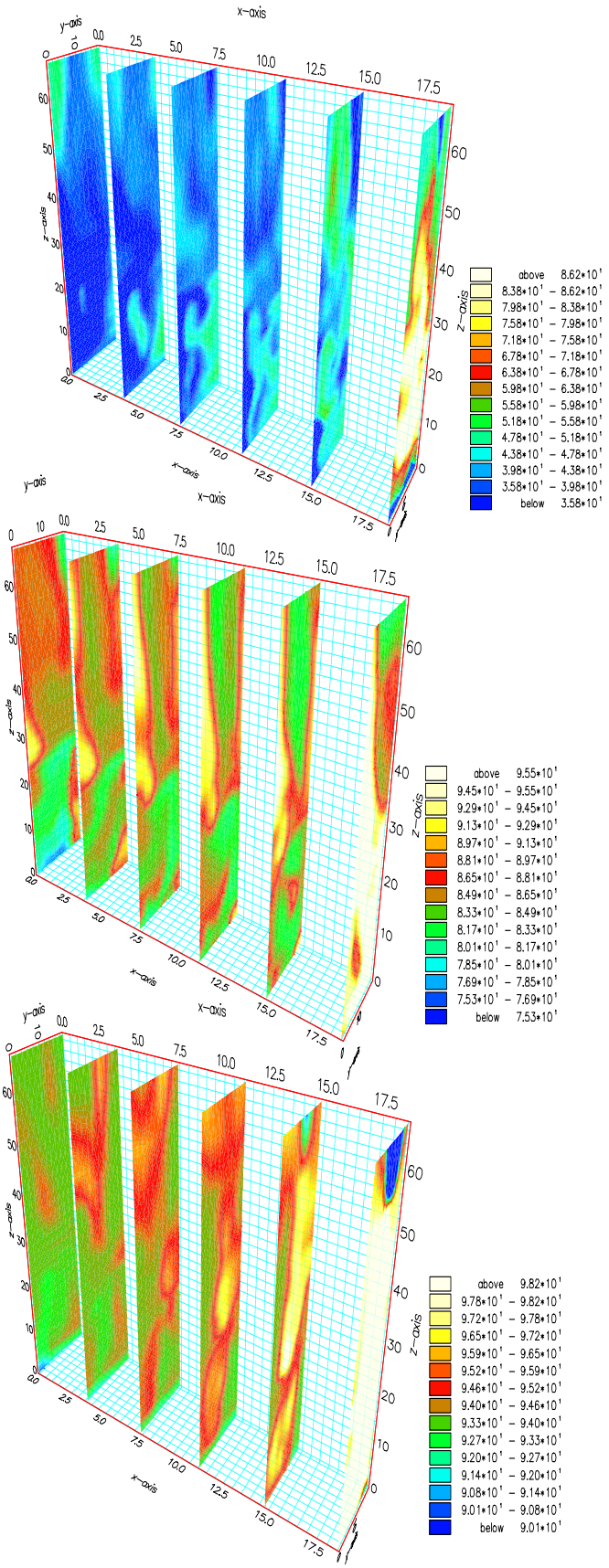

(a) t =1.96 seconds

(b) t =11.47 seconds

(c) t =20.59 seconds

Figure 4.18: Flow past a heated wall - 3-D simulation: gas phase temperature distribution at (a) 1.96, (b) 11.47 and (c) 20.59 seconds.

term simulations including further investigations during fully steady state regime should be conducted. The similarity of the overall heat transfer behavior along the wall between 2-D and 3-D can be noticed by comparing Figures 4.9 and 4.21, respectively. In the later, the surface map of four snapshots of the heat transfer coefficient along the heated surface are shown. As described in Sections 4.2 and 4.3, the thermal diffusion mainly occurs in the emulsion phase, therefore large H_T is expected in regions with relatively large solid concentration. Such behavior can be observed in the set of solid volume fraction and heat transfer coefficient snapshots presented in Figures 4.20 and 4.21.

4.5 Conclusions

In this work, the two-fluid granular temperature model was used to study the heat transfer mechanisms of fluidization of monosized particles by air. The set of governing and constitutive equations were solved by a multiphase finite element method code, FLUIDITY. The thermal effective conductivity of the solid phase was calculated using a granular temperature based correlation which makes the thermal energy analysis consistent with the overall hydrodynamics model.

In order to investigate the heat transfer in the bubbles' wake, 2-D and 3-D simulations were performed and the rising of bubbles along a heated wall was studied. Fresh particles were dragged in the rear of uprising bubbles, replacing hot particles and increasing the temperature gradient. Such replacement, which improved the solid circulation in the bubbles' wake, enhanced the heat transfer rates.

As the heat exchanged between the surface and the bed is mainly due to the solid phase, the granular temperature may play an important role in the heat transfer coefficient calculation. Indeed, in highly packed regions the heat transfer coefficient is small due to low granular temperature, however, in dilute regions, i.e., in regions where the solid volume fraction is very low, the granular temperature is also low due to the low collisional probability. In the bubbles wake, however, a large solid concentration combined with large granular temperatures and shear stresses result in large wall heat transfer coefficients. Such behavior was shown in Figures 4.6-4.9.

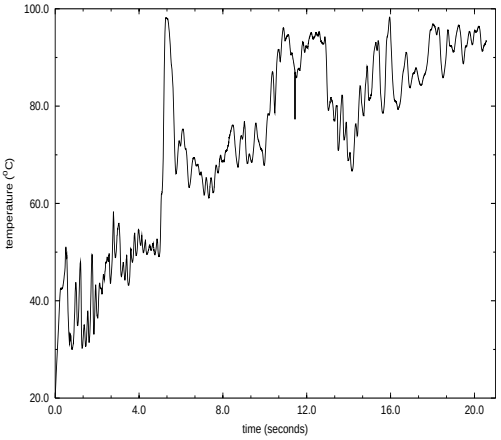

(a) (17.63;18.50;4.31)

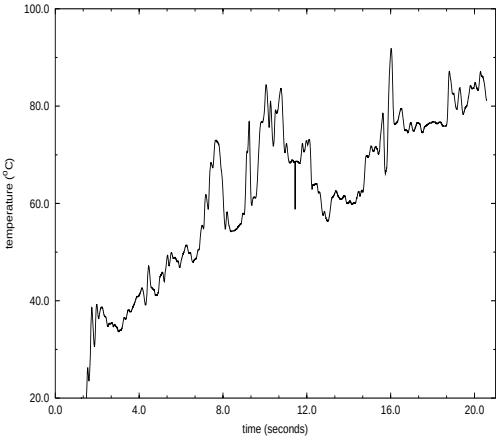

(b) (10.88;18.50;4.31)

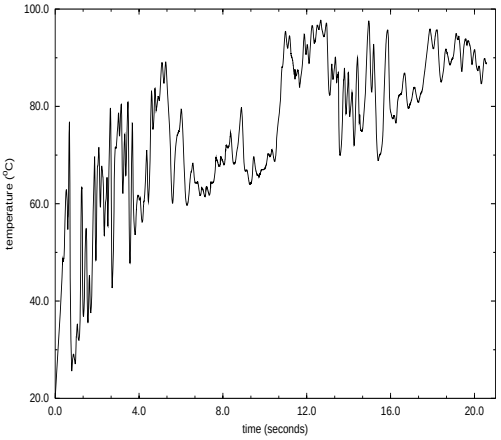

(c) (17.63;18.50;10.00)

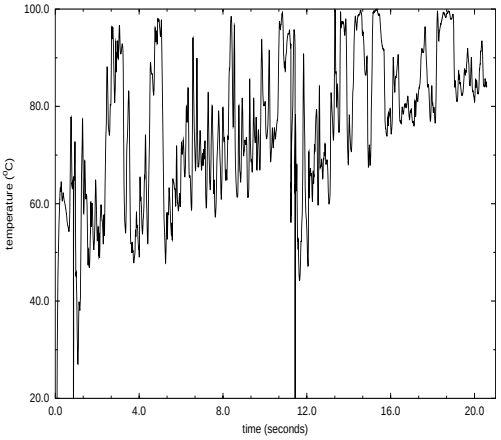

(d) (17.63;18.50;30.91)

Figure 4.19: Flow past a heated wall - 3-D simulation: gas phase temperature fluctuations from detectors placed in the following positions (*xyz* coordinates in cm): (a) (17.63;18.50;4.31), (b) (10.88;18.50;4.31), (c) (17.63;18.50;10.00) and (d) (17.63;18.50;30.91). In (a), (c) and (d), the detectors are in the bed corner along the heated wall. In (b), however, the detector is at the same height of (a), but far from the wall.

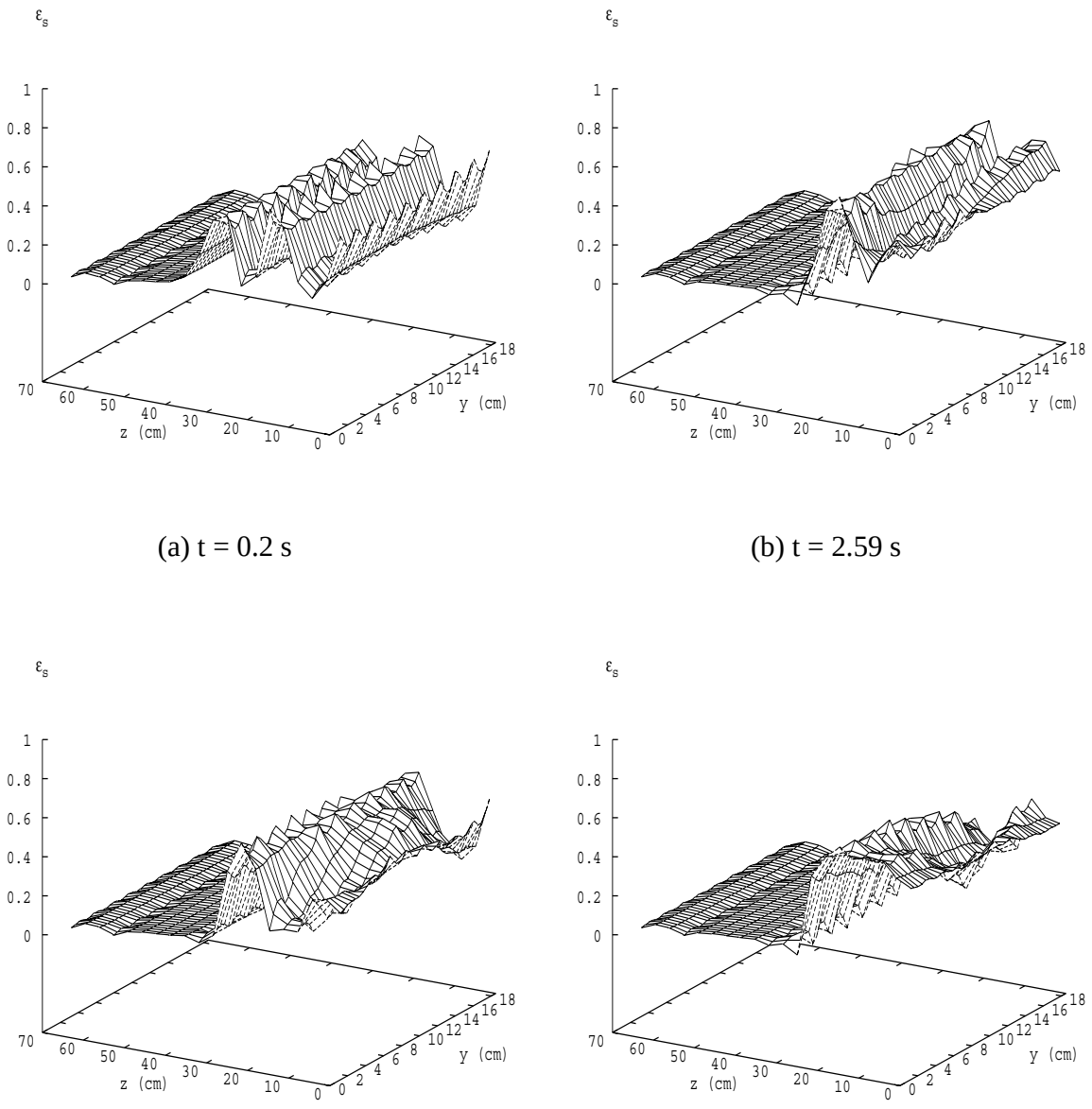

(a) t = 0.2 s

(b) t = 2.59 s

(c) t = 13.79 s

(c) t = 20.36 s

Figure 4.20: Flow past a heated wall - 3-D simulation: surface map of the solid volume fraction along the heated surface at (a) 0.20 s, (b) 2.59 s, (c) 13.79 s and (d) 20.36 s.

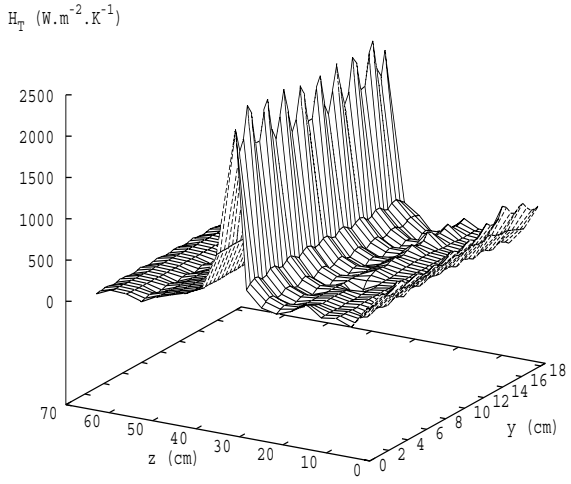

(a) t = 0.2 s

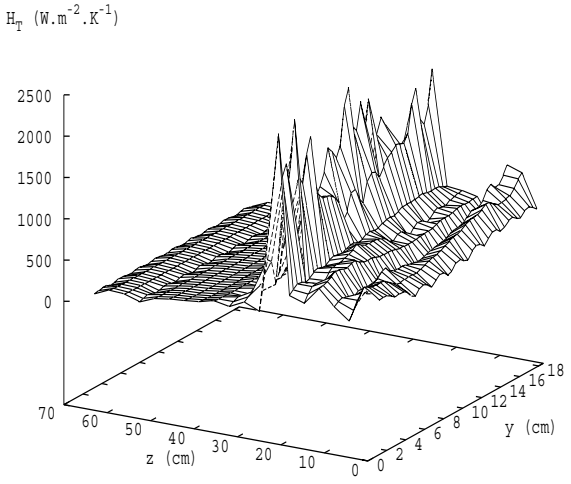

(b) t = 2.59 s

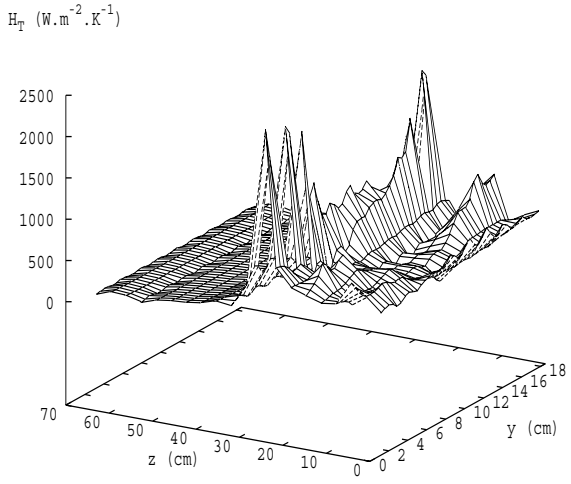

(c) t = 13.79 s

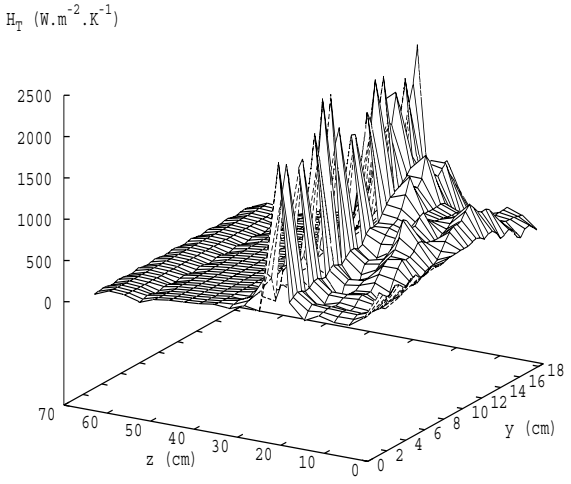

(c) t = 20.36 s

Figure 4.21: Flow past a heated wall - 3-D simulation: surface map of the heat transfer coefficient along the heated surface at (a) 0.20 s, (b) 2.59 s, (c) 13.79 s and (d) 20.36 s.

The time-averaged heat transfer coefficients obtained from 2-D and 3-D numerical simulations were in good agreement. For 2-D simulations, time-averaged heat transfer coefficient in the order of 427 W.m^{-2}.K^{-1} were found, whereas for 3-D simulations, the heat transfer coefficient was 449 W.m^{-2}.K^{-1}. Although, there was not any reliable experimental data available for further validation, the model introduced here and elsewhere [100, 111] and validated, in a 2-D framework, against experiments by Gomes *et al* [112] may confidently be used to model heat transfer in granular flows.

Chapter 5

Modelling Coupled Multiphase-Flow and Neutron-Radiation

In this chapter[1], the dynamical analysis of axisymmetric two and three dimensional simulations of a nuclear fluidized bed reactor is presented. A coupled neutron radiation (in full phase space) and high resolution multiphase gas-solid Eulerian-Eulerian model is used. The nuclear criticality of the system results in the deposition of heat energy into the nuclear fuel particles which are then cooled by the fluidizing helium gas. After exploring the spatial and angle of neutron travel convergence of the numerical solutions as well as the effect of dimensionality (2-D and 3-D solutions), the numerical model is analyzed using a statistical approach to help determine the root cause of reactor power fluctuations.

[1]This chapter was submitted for publication in the International Journal of Computational Methods in Fluids: C. C. Pain, J. L. M. A. Gomes, M. D. Eaton, C. R. E. de Oliveira, A. J. H. Goddard (2003), *A Model of Heat Transfer Dynamics of Coupled Multiphase-Flow and Neutron-Radiation: Application to a Nuclear Fluidized Bed Reactor*.

5.1 Introduction

The aim of this chapter is to investigate the numerical convergence in space and direction of angle of neutron travel of a model of a nuclear fluidized bed reactor and the effect of using 2-D and 3-D geometries on the model results, and also to investigate the route cause and sensitivity of particle concentration to fission-power variability. In the latter, a surrogate model of fission-power and reactor temperature was developed.

Nuclear reactor concepts based on gas fluidization of fine uranium fuel pellets have attracted considerable attention over the years. Reasons behind this interest lie in their excellent heat transfer capabilities [22] and the mixing ability of the fluidized bed. The latter unifies the temperature of the bed, and increases the active surface area from which heat transfer occurs. In addition, the constant mixing of the bed potentially leads to a uniform burnup of the uranium particles. A self-controlling feature is also present in that as the bed is fluidized and the gas flow increases, the power achieves a maximum at a particular bed height. At this height, the power will be that at which heat production is balanced by heat losses.

A possible disadvantage of such a reactor is the chaotic particle flow characteristics of the fluidized bed in which large bubbles and slugs propagate through it [5], changing the geometry and nuclear criticality. This will impact on the fission rate which will also be highly variable - although it is possible that the power output obtained from the heated gases may not be as variable. This variability and chaotic unpredictability requires further investigation in order that the concept can be assessed.

Deterministic chaos theory offers a powerful description of irregular behavior and anomalies in systems which do not seem to be stochastic. In such systems, small perturbations in the initial conditions lead to large discrepancies in the final solution [47]. Indeed, chaos theory applied to the output signals is a useful tool for the understanding of nonlinear systems as demonstrated by its application to the nuclear reactor investigated in this work. It is often used to quantify the regime (e.g. bubbling and slugging) that fluidized beds operate in [43, 113].

Power variability in a nuclear fluidized bed reactor has been studied by van Dam *et*

al. [114] who investigated the sensitivity of the reactor to voidage fluctuations. This reactor concept adopts aspects of the pebble bed reactor [115] and the fuel particles are of a design as reported by Gulden & Nickel [116] (see also [117]). Other reactor designs of this type are described by Sefidvash [118].

The modelling approach shown here (see also [100, 78, 111] applies detailed spatial/temporal modelling so that the reactor dynamics evolve naturally. This is in contrast to point kinetics models [119] which, although often having adequate accuracy, require correlation with existing data when the material evolves within the transient, such as in fissile liquid transients [120, 121] and nuclear fluidized beds. Others have used space-dependent kinetics to model transients in fissile liquids, see [122, 123, 124]. Some point kinetics models for powders are reported by Rozain and Basoglu *et al.* [125], and for the nuclear fluidized bed models [126, 127, 128].

An integrated neutrons/fluids/heat transfer method embodied in the Finite Element Transient Criticality (FETCH) model [129], is used here. The neutronics model in FETCH solves the neutron Boltzmann transport equation in full phase-space (space, time, angle and speed travel) using a variational finite element approach based on the second order even parity equations (see [130]). The fluids algorithm is a high-resolution multi-phase compressible flow model which solves the conservation equations for both gas and solid particle phases. This unique fundamentally based combined methodology is able to model the complex non-linear reactivity feedback mechanisms which occur in nuclear reactor designs such as the one studied in this paper. The FETCH model has been compared against solution transient criticality experiments [129, 131, 132, 133] and fluidized bed experiments [134, 78, 11].

The two-fluid granular temperature method was chosen to model the gas-solid flow in the nuclear fluidized bed. Within the solid phase, particle modelling is based on an analogy between the kinetic theory of gases and binary particle-particle collisions [85, 135, 72, 83, 84]. These models are proving to be accurate for a wide range of gas-solid fluidization scenarios (see [136, 41]).

In sections 5.2 and 5.3, the Boltzmann neutron transport equations and the two-fluid granular temperature equations are presented. The model used to solve this coupled sys-

tem is summarized. The dynamics of 2-D nuclear fluidized bed reactors are explained and the grid dependence investigated in section 5.4. Numerical simulations conducted in 3-D geometry are then shown. And finally, dynamic analysis is applied to fission-power and voidage time series to investigate the bubbles dynamics and the relationship between bubble production and fission power. In addition, a surrogate method is proposed to predict both fission-power and reactor temperature over a short time interval. Conclusions are drawn in the final section.

5.2 Neutronics

The Boltzmann neutron transport equation (Table 5.1) is solved using finite elements in space, spherical harmonics (P_N) in angle, multigroup in energy and implicit two level time discretization methods. Such methods were applied using the second-order even-parity variational principle as described by [130]. This equation is solved in full 7 dimension phase space. Six energy groups were used and obtained by collapsing the original WIMS 69 group library taking into account resonant self shielding and particle spatial effects into 6 energy groups [137]. A set of cross-sections is generated for various temperatures and these are used to obtain (with a temperature interpolation procedure) the local cross-section set for each element of the finite element mesh. Six delayed neutron precursor concentration groups [138] are used in these simulations.

5.3 Two-Fluid Granular Temperature Model

In the two-fluid models (TFM) both phases are continuous and fully interpenetrating, and are described by separated conservative equations with interaction terms representing the coupling between the phases. The TFM requires additional closure laws to describe the rheology of the particulate phase. These closure laws are based on the assumptions of kinetic theory for granular flows (reviews can be found in [38]). As the rheology of the granular phase was based on empirical correlations, Jenkins *et al.* [72] and Ding & Gidaspow [41] proposed a model in which the solid viscosity and the normal stress are

Continuity equation	$\frac{\partial}{\partial t}\left(\varepsilon_k \rho_k\right) + \frac{\partial}{\partial x_i}\left(\varepsilon_k \rho_k v_{ki}\right) = 0$
Momentum equation	$\frac{\partial}{\partial t}\left(\varepsilon_k \rho_k v_{ki}\right) + \frac{\partial}{\partial x_j}\left(\varepsilon_k \rho_k v_{ki} v_{kj}\right) = -\varepsilon_k \frac{\partial p_g}{\partial x_i} + \varepsilon_k \rho_k g_i + \beta\left(v_{k'i} - v_{ki}\right) - \frac{\partial}{\partial x_i}\left(\tau_{kij}\right) - \Gamma_k v_{ki}$
Thermal energy equations	$C_{p_g} \rho_g \epsilon_g \frac{DT_g}{Dt} = -p_g\left(\frac{\partial}{\partial x_i}\varepsilon_g v_{g_i} + \frac{\partial}{\partial x_i}\varepsilon_s v_{s_i}\right) + \frac{\partial}{\partial x_i}\left(\varepsilon_g \kappa_g \frac{\partial T_g}{\partial x_i}\right) + \alpha\left(T_s - T_g\right) + \widehat{\Gamma}_{wg}$ $C_{p_s} \rho_s \epsilon_s \frac{DT_s}{Dt} = \frac{\partial}{\partial x_i}\left(\varepsilon_s \kappa_s \frac{\partial T_s}{\partial x_i}\right) + \alpha\left(T_g - T_s\right) + \widehat{\Gamma}_{ws} + S_f$
Granular energy equation	$\frac{3}{2}\left[\frac{\partial\left(\varepsilon_s \rho_s \Theta\right)}{\partial t} + \frac{\partial}{\partial x_j}\left(\varepsilon_s \rho_s v_{s_j} \Theta\right)\right] = \tau_{s_{ij}} \frac{\partial v_{s_i}}{\partial x_j} - \frac{\partial q_j}{\partial x_j} - \gamma - 3\beta\Theta$
Equation for *d*-th delayed neutron group precursor concentration	$\frac{\partial C_d(\mathbf{r},t)}{\partial t} + \frac{\partial v_{s_j} C_d(\mathbf{r},t)}{\partial x_j} = -\lambda_d C_d(\mathbf{r},t) + \beta_d \int_0^\infty \nu\Sigma_f \phi(\mathbf{r},E,t)\, dE$
Neutron Transport Equation	$\frac{1}{v}\frac{\partial \psi\left(\mathbf{r},\mathbf{\Omega},E,t\right)}{\partial t} + \mathbf{\Omega}\cdot\boldsymbol{\nabla}\psi\left(\mathbf{r},\mathbf{\Omega},E,t\right) + \mathcal{H}\psi\left(\mathbf{r},\mathbf{\Omega},E,t\right) = S\left(\mathbf{r},\mathbf{\Omega},E,t\right)$

Table 5.1: Conservation equations used in the simulations.

derived using an analogy between the particle-collision during granular flows and the gas kinetic theory. Hence, the concept of granular temperature as a measure of the agitation of particles was introduced. The granular temperature is, therefore, a link between kinetic theory and traditional fluid mechanics. The set of TFM conservative equations that describes the gas-solid flow and the additional closure laws are summarized in [134, 78] (see also [38]).

The following sections provide an overview of the discretisation and solution methods used to solve the granular temperature two-fluid equations. The full description can be found in [100, 78].

5.3.1 High Resolution Method

A high resolution method is used in this work to achieve bounded physical meaningful solutions that are also highly accurate. The method used to limit the spatial derivatives is based on the NVD approach [139] in which face variables are calculated from the element centred values of the field being solved. The variation of these face variables over each face is then limited using the NVD approach so that, if a local extrema is found, then the method switches to a first order spatial discretisation. This switching is performed in a smooth manner and smoothly depends on a extrema-detecting variable.

A second order temporarily limited time stepping method (based on the Crank Nicholson method) is used in this work to help achieve bounded solutions, e. g., positive volume fraction.

5.3.2 Momentum Discretization

To maintain consistency with the discretized continuity equation, pressure as well as volume fractions have a piecewise constant variation across each hexahedral element. For similar reasons the granular temperature equations are also discretized using the high resolution method described above. The velocities have a tri-linear variation across each element and are thus centred on the nodes of the finite element mesh. The momentum equations are discretized using a Bubnov-Petrov-Galerkin method by multiplying each of

the momentum equations for the three velocity components by finite element basis functions and integrating the resulting pressure term by parts. A non-linear Petrov-Galerkin method is used to suppress velocity oscillations normal to the flow direction. The momentum equations are discretized in time using implicit Crank-Nicholson time stepping, see [78] for further details.

A semi-implicit projection method is used to solve the coupled multiphase continuity and momentum equations. This method treats the coupling between the phases implicitly in pressure. A mixed finite element method with a constant variation of pressure throughout each element and a bi-linear variation of velocity is used here to avoid singularities in the discretized equations.

5.4 2-D Numerical Simulations

5.4.1 Geometry

The fluidized bed nuclear reactor comprises of an internal cavity 6m tall and 1.25m in diameter in which the fluidized fuel particles are free to move (Figure 5.1(a)). The particles are 1mm in diameter TRISO coated spheres with a uranium kernel and have a moderator to fuel (uranium) content by volume of 300 to 1. The particles are described in [111]. The internal cavity of the reactor is surrounded by graphite moderator which slows down the neutrons and reflects them back into the reactor. These slow neutrons are particularly effective at producing subsequent neutrons from fission reactions and thus the largest power density of the reactor tends to be situated near the walls of the reactor. It also means that as a large mass of particles approaches a wall of the reactor the reactor responds with positive reactivity feedback. This provides the root source for the fission-power fluctuations in the reactor. The graphite side, top and bottom walls of the reactor are 1m in thickness. The graphite at the top and bottom of the reactor is porous. This porous graphite is a new design feature over previous design [111] which enables the reactor to be more sub-critical in the collapsed bed state and also provides a flatter reactivity (K_{eff}) curve versus uniformly expanded bed height. The reactivity of the system, measured by the eigenvalue K_{eff}, is the ratio of the number of neutrons generated from one

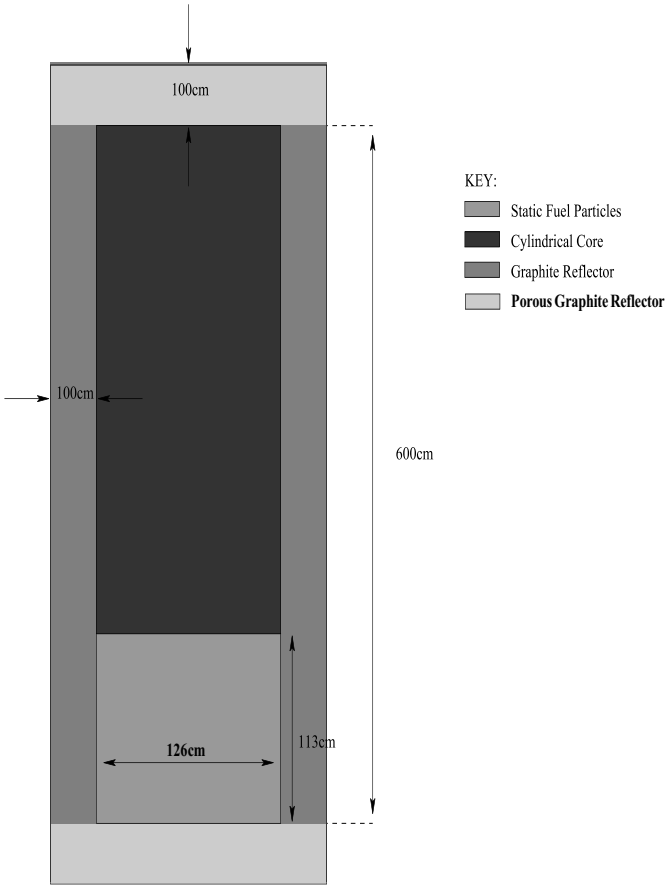

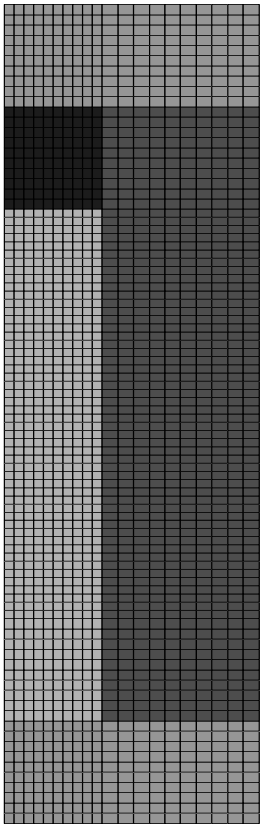

(a) 2-D schematic of the FLUBER reactor (b) 2-D finite element mesh

Figure 5.1: FLUBER reactor: (a) Schematic and (b) finite element mesh. The coarse mesh is shown here, the corresponding fine mesh has twice the resolution in each direction.

	Solid Phase	**Gas Phase**
Density ($kg.m^{-3}$)	1.92×10^{3}	ideal gas law
Thermal Conductivity ($W.m^{-1}.K^{-1}$)	1.0	2.15×10^{-1}
Heat Capacity ($J.kg^{-1}.K^{-1}$)	1.40×10^{3}	5.24×10^{3}
Particle Diameter (m)	1.00×10^{-3}	–
Dynamic Viscosity ($kg.m^{-1}.s^{-1}$)	–	2.70×10^{-5}

Table 5.2: Physical properties of the solid (TRISO coated fuels spheres) and the gas (helium) phases.

neutron generation to the next. Thus a flatter reactivity curve is safer, since if the system goes supercritical and deposits heat energy which expands the bed there is not a positive reactivity feedback associated with this expansion which could make the reactor dangerous. Curves showing the reactivity of the reactor system versus uniformly expanded bed height are shown in Figure 5.2(a) for differing porosities. K_{eff} in these figures is a measure of the criticality of the system of the neutron multiplication and from one neutron generation to the next. The initial bed porosity used in the simulations conducted here is 0.4. The simulations were conducted in r-z geometry and the physical properties of both phases used in this work are outlined in Table 5.2. In addition, the initial and boundary conditions are summarized in Table 5.3. Several fields were obtained by solving the set of fluid and neutron transport equations, among them, the following will be directly used to demonstrate the robustness of the numerical methods advocated here: delayed neutrons concentration, solid volume fraction, temperature of both phases, granular temperature and the velocity components of the gas and solid phases. In order to investigate the time series of these fields, several detectors were placed within the bed as shown in Table 5.4.

In the simulations presented in the following sections (see Figure 5.1(b)), the domain

Initial ε_s	0.40
Inlet gas velocity	$\mathrm{v}_f\,(r, z=0, t)$=1.20 m.s^{-1}
Inlet gas temperature	$\mathrm{T}_f\,(r, z=0, t)$=226.85^{o}C
Initial gas and solid phase velocities	$\mathrm{v}_s\,(r, z, t=0)$=0.0 m.s^{-1} $\mathrm{v}_f\,(r, z\neq 0, t=0)$=0.0 m.s^{-1}
Initial gas and solid temperatures	$\mathrm{T}_f\,(x, y, t=0)$=226.85 ^{o}C $\mathrm{T}_s\,(x, y, t=0)$=226.85 ^{o}C
Solid flow at top boundary	$\mathrm{v}_s\,(r, z=L, t)$=0.0 m.s^{-1}
Solid stress at top boundary	$\tau_s\,(r, z=L, t)$=0.0 N.m^{-2}
Particle-particle restitution coefficient	e_{pp}=0.97
Wall-particle restitution coefficient	e_{wp}=0.90
Friction coefficient	$\overline{\mu}$=0.3

Table 5.3: Initial and boundary conditions applied into the numerical simulations.

had (unless otherwise stated) 2000 volume elements and 2121 nodes, and the fluids occupied domain had 750 volume elements and 836 nodes.

5.4.2 Physics of the Reactor

As the uranium particles are fluidized and the bed expands, the system becomes supercritical and so the fission heat source increases exponentially. The reactivity (measured by the eigenvalue and which determines the magnitude of the exponent) of the system increases on uniform bed expansion (bed height) as shown in Figure 5.2. This shows that during the bed expansion, the reactivity reaches a maximum and on further expansion of the bed the reactivity decreases due to the increase in neutron leakage out of the system. The reactivity of the system is enhanced due to the increase in moderated and reflected neutrons back into the fluidized bed on its expansion. This reactor has been re-designed so that it is more subcritical in collapsed bed or fully expanded state. In particular the solid graphite walls surrounding the fluidized bed cavity have been replaced at the top and bottom of the reactor, see Figure 5.1(a), by porous graphite with a volume fraction of

Detector	z(cm)	r(cm)
01	100.00	62.00
02	150.00	62.00
03	200.00	62.00
04	100.00	31.00
05	150.00	31.00
06	100.00	0.00

Table 5.4: Position of the six detectors within the bed.

60 %. The effect on the reactivity, gauged by the eigenvalue, on the reactivity is seen in Figure 5.2(a). The porous graphite provides for a flatter curve which is desirable on safety grounds. The response to void fluctuations near the bottom of the reactor is reduced with this modification - due to the neutrons not being reflected back, as readily, into the regions of high particle volume fraction near the bottom wall.

As helium gas at 60 bars pressure is pumped through the reactor and the bed expands and becomes supercritical, it heats up due to fission heat sources from neutrons. As the temperature of the particles increases the reactivity of the system decreases and eventually stabilizes in a time averaged sense, such that heat loses to the fluidizing helium balances the fission power. However, voidage oscillations in the reactor will provide a noisy fission-power.

5.4.3 Temperature feedback and mixing

The reactor has been designed to have an overall negative temperature coefficient. Which means that as the temperature increases the reactivity of the system decreases as shown in Figure 5.2(b). This provides a passive control of reactivity. This negative feedback effect makes the power respond very quickly to temperature changes in the reactor and enables this reactor concept to work (at least in the simulations) despite the rapid changes in reactivity of the system due to redistributions of the fuel particles in the reactor.

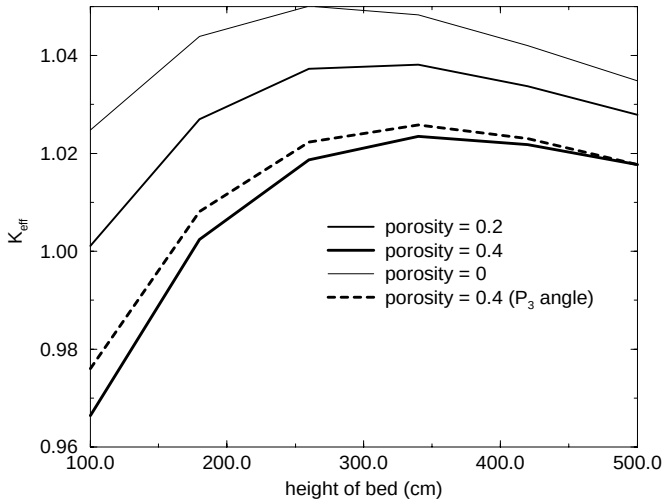

(a) K_{eff} *versus* uniformly expanded height

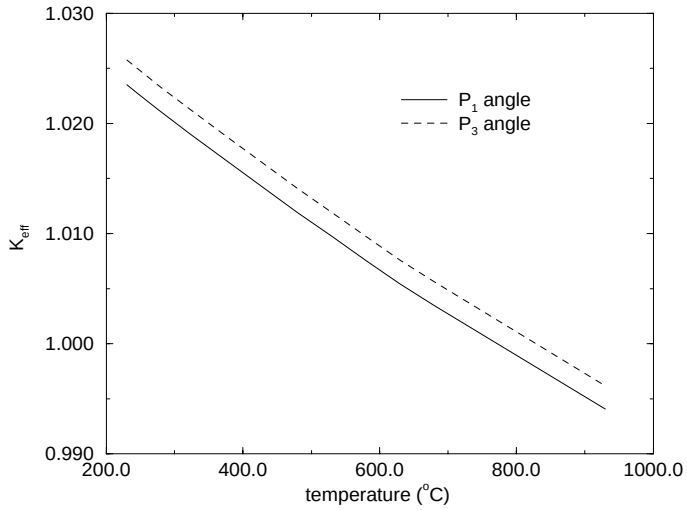

(b) K_{eff} *versus* temperature

Figure 5.2: The reactivity of the system (K_{eff}) versus uniformly expanded bed height. Graph shows reactivity for differing porosities of the graphite at the top and bottom of the reactor. In addition (b) shows the variation of K_{eff} with temperature for a uniform bed height of 340 cm.

It has been shown, in a previous study [111], that this mixing allows the particles to be exposed to the same fission-heat source over relatively small time scales (6 seconds of reactor operation at quasi steady-state). This means that the fuel will be uniformly burnt in the reactor. In that study it was also shown that despite the rapid variations in fission rate by an order of magnitude over as little as 1 second, the temperature of the reactor was remarkably steady and uniform. All these features have been observed also in this reactor and are thus not investigated in detail here.

5.4.4 The central transport theory simulation explained

An axi-symmetric transient simulation was conducted using the mesh shown in Figure 5.1(a) and a P_3 (transport theory) angular expansion (3 angular moments). As with all simulations conducted here, adaptative time stepping method was used. A total fuel particle mass of 8429.28 g was used. Figures 5.3 (a) and (b) show the fission rate and maximum temperature respectively of the reactor. The fission rate has a long term oscillation associated with it as well as short term oscillations. The long term oscillations occur because the reactor is initially cool and thus the negative reactivity feedback effects associated with temperature take some time to take effect. This allows a large fission spike to develop which deposits a great deal of heat energy mostly in the bottom corner of the reactor and heats the system to a maximum temperature of 730^{o}C, see Figure 5.3 (b).

This rapid increase in temperature dissipates through the reactor, due to solids mixing and heat transfer through the gas phase. The result is a sharp initial pulse in maximum temperature, Figure 5.3 (b), after which the bed temperature becomes quite homogeneous. However, it takes about 200 seconds for the fluidizing helium to extract enough heat energy from the particles for the system to become supercritical again and the fission rate to rise, see Figure 5.3 (a). This is then followed by smaller but similarly produced subsequent oscillations.

It is well known that delayed neutrons in other nuclear reactors and critical systems [132] combined with heat losses also provide a mechanism for producing fission oscillations. A similar mechanism is believed to cause the longer fission power oscillations in this reactor. Graphs of the maximum longest lived delayed neutron precursor concentra-

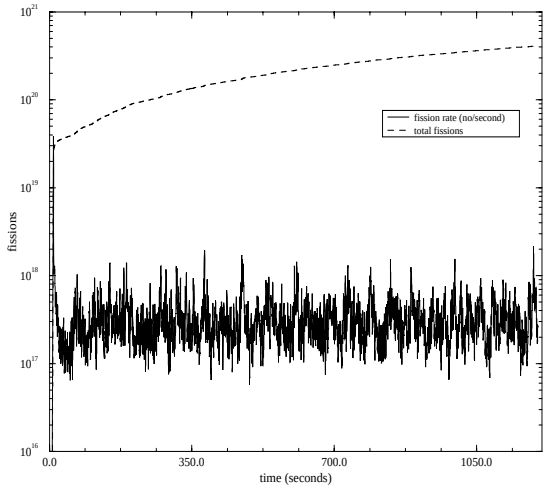

(a) fission rate and accumulative fission

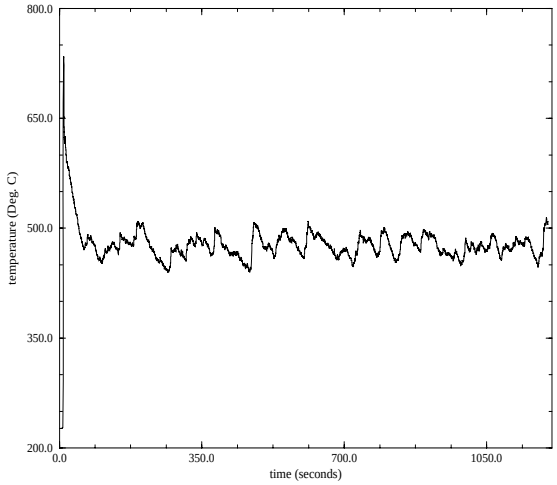

(b) maximum gas temperature

Figure 5.3: The fission rate (a) and maximum gas temperature (b) versus time for the P_3 simulation conducted in $r-z$ geometry.

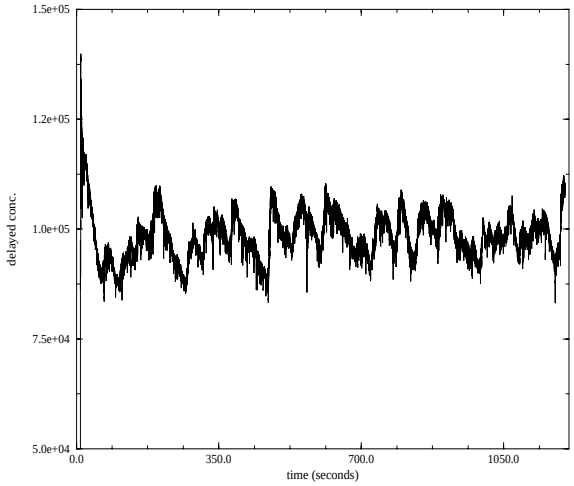

(a) maximum longest lived delayed concentration

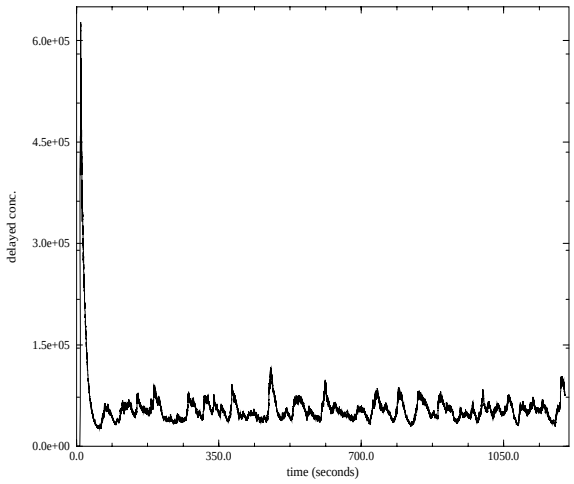

(b) maximum 3^{rd} longest lived concentration

Figure 5.4: (a) Maximum longest delayed neutron precursor concentration against time and (b) maximum third longest delayed neutron concentration versus time for the P_3 simulation conducted in $r-z$ geometry.

tion, half life of 55 seconds, and the third longest lived delayed concentration, half life of 5 seconds, respectively are shown in Figure 5.4. Figure 5.4(a) also effectively shows the time averaged, over time scale of 55 seconds, heat source from fissions. Figure 5.4 (b) shows the maximum delayed neutron concentration of the third longest lived group. The fission rate, solids volume fraction and gas temperature at the bottom corner (detector 1) of the reactor core are shown over a relatively short time period in Figure 5.5. Detector 1 is the detector at which the temperature varies most rapidly and thus this temperature gives an indication of the temperature range in the reactor.

5.4.5 Fine mesh simulation

In this section, the convergence in space of the simulated fluidized bed reactor is examined by dividing all elements in half in each direction. Therefore, there are four times the number of elements shown in Figure 5.1(a), i.e., there are 8000 volume elements and 8241 nodes. The fluids occupied domain of 3000 volume elements and 3171 nodes. In addition, a total fuel particle mass of 9046.06 g was used.

This simulation was performed over 194 seconds using a P_1 neutron angle approximation and the fission rate and maximum gas phase temperature versus time for this short simulation (due to the computation expense) are shown in Figures 5.6. This does not have the large fission spike that most of the other simulations have. This highlights the rather unpredictable starting characteristics of this reactor with these extreme start up conditions. In addition, the solids temperature and particle volume fraction at detector 1 (bottom corner of reactor cavity) are shown in Figure 5.7. This figure is included to highlight the correlation between particle volume fraction at the bottom corner and power and therefore temperature of the reactor.

The volume fraction, solids temperature, 2^{nd} longest lived delayed group and shortest lived delayed group fields are shown in Figure 5.8 at 80 seconds into this simulation. The similarity of the volume fraction and 2^{nd} delayed groups has been noticed before, and is attributed to the fission heat source for each particle being the same when time averaged over the time scale of the half life of the 2^{nd} delayed group which is 22 seconds. In addition, the shortest lived delayed group, with a half life of 0.2 seconds, reflects the

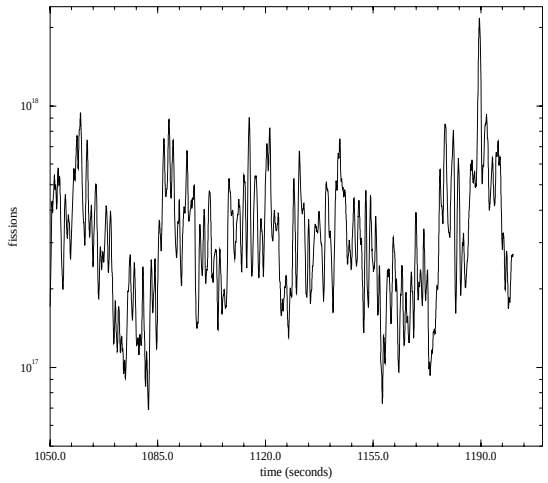

(a) fission rate

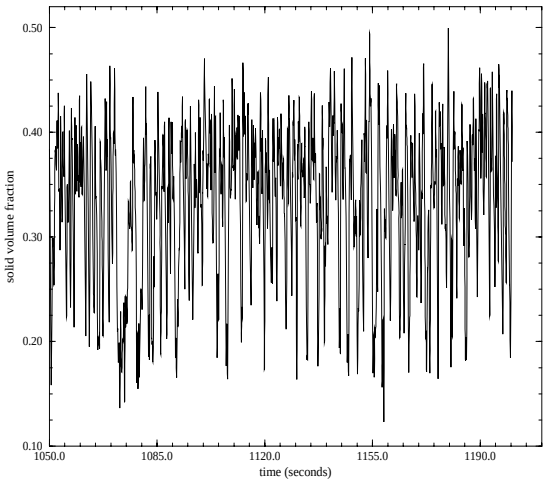

(b) solid volume fraction at detector 1

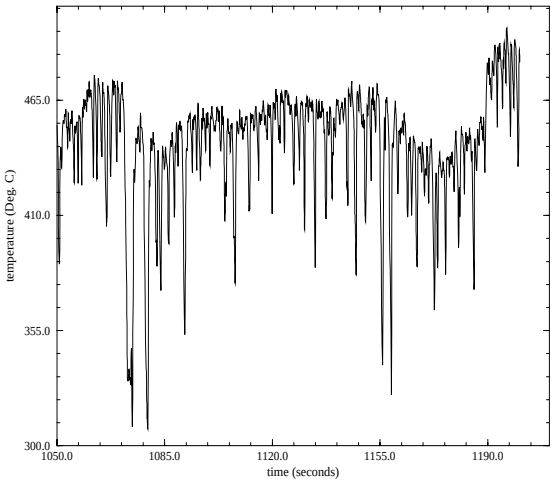

(c) solid temperature at detector 1

Figure 5.5: (a) Fission rate, (b) solid volume fraction and (c) solid temperature at detector 1 (bottom corner of the reactor) versus time for the P_3 simulation conducted in $r - z$ geometry.

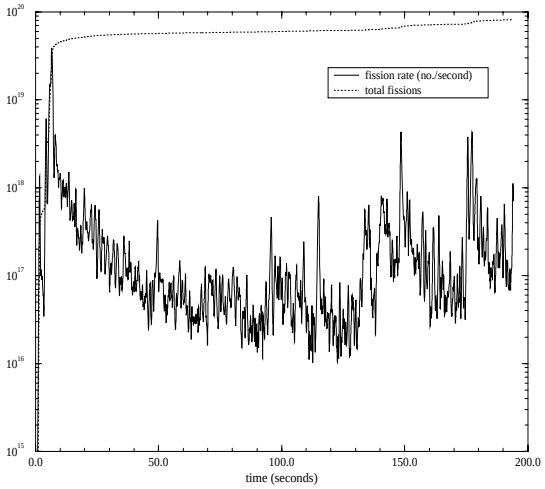

(a) fission rate and accumulative fission

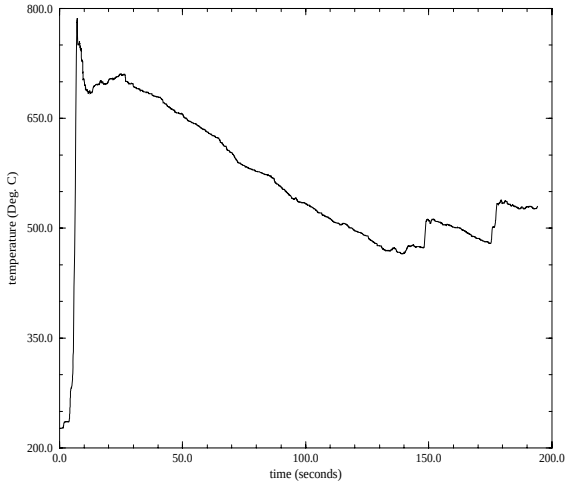

(b) maximum gas temperature

Figure 5.6: The fission rate (a) and maximum gas temperature (b) versus time for the fine mesh simulation conducted in $r - z$ geometry.

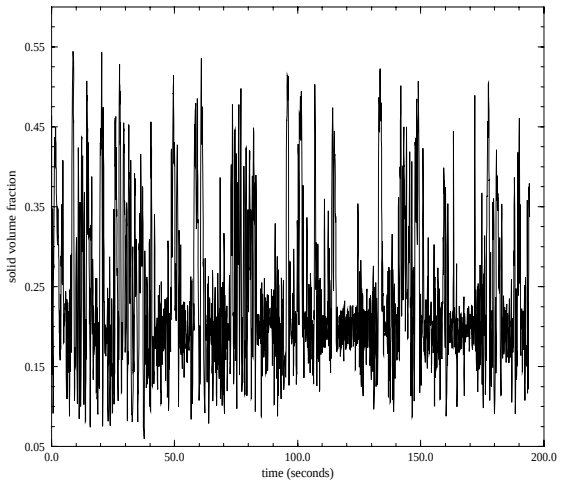

(a) solid volume fraction

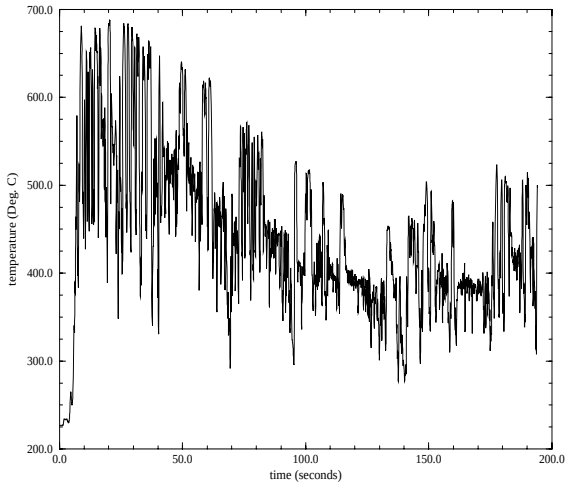

(b) solid phase temperature

Figure 5.7: (a) Solid volume fraction and (b) solid phase temperature at detector 1 (bottom corner) versus time for the fine mesh simulation conducted in $r - z$ geometry.

power distribution in the reactor at a given instant in time. As seen in Figure 5.8 (d) the power is largest near the bottom corner of the internal cavity and next to the vertical walls. The walls are made from graphite which moderates and reflects the neutrons back into the reactor and coarsens subsequent fissions. Making the bottom of the reactor from porous graphite has reduced the local effectiveness to reactivity of this area. Since the focus from this area of the reactivity is reduced and in some sense spread out, this has the effect of reducing the response to voidage fluctuations and is one of the main advantages of this new design. The solid volume fraction distribution at equally spaced time intervals between 80 and 82.5 seconds into the simulation, is shown in Figure 5.9. This is included to give an insight into the dynamics of this reactor. Correlations for bubble size and height at which slugs occur [5] suggest that the slugs would appear at about a 1.5m height above the cavity floor. This is reflected in the results shown in Figure 5.9.

5.4.6 The effect of varying the gas fluidization velocity

To investigate the effect of using a different inlet velocity, simulations with inlet superficial gas velocity of 60 and 120 cm/s were performed (the last was used in all the other simulations). Figure 5.10 shows the fission rate and maximum solids temperature versus time of the simulation with the lower inlet gas velocity. This simulation was performed over a particularly long time of about 25 minutes because as can be seen in the fission rate curve this simulation was prone to producing large peaks in the fission rate, even after the initial conditions are no longer felt. The large peaks in the fission rate increase the temperature and makes the temperature vary by as much as 100^{o}C. Notice that the temperature of this reactor is nearly as large (in a time average sense after the initial pulse) as the temperature of the same simulation but with a larger inlet velocity. This is due to the flatness of the K_{eff} versus expanded height curve. The fluidized bed has expanded to about a height of 2.25 m, see Figure 5.11 (a), and thus will produce a temperature near that of the bed with 120 cm/s inlet velocity which expanded the bed to approximately 4 m in height. The solids temperature, which is fairly uniform, is shown in Figure 5.11 (b) and the second longest lived delayed neutron concentration and shortest lived concentration fields are shown in Figures 5.11 (c) and (d) respectively.

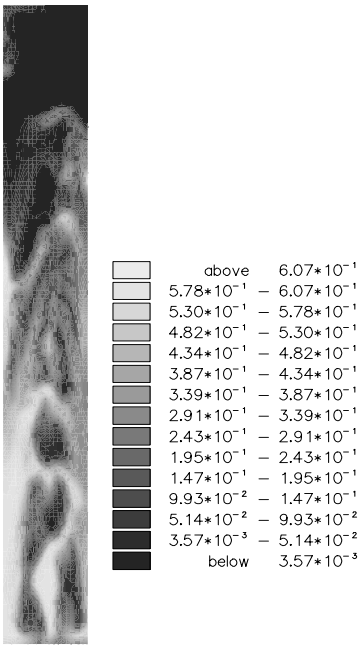

(a) solid volume fraction

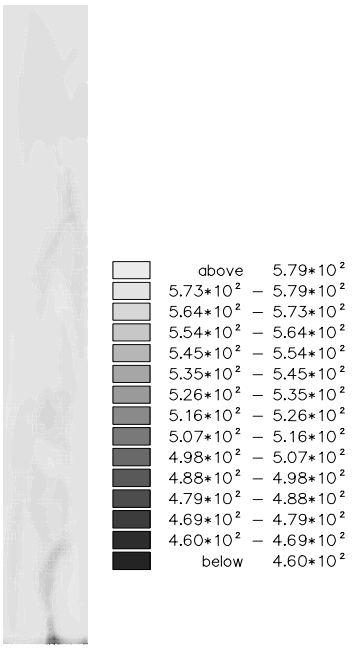

(b) gas temperature (^{o}C)

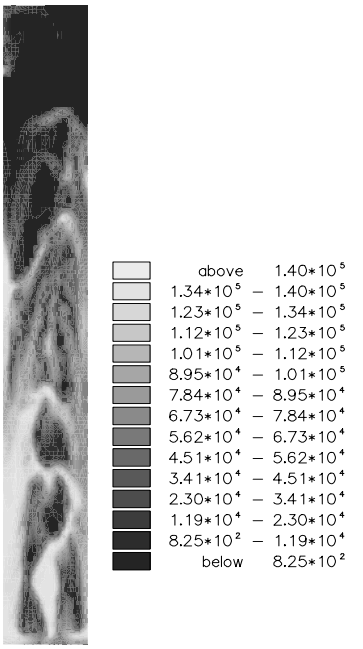

(c) 3^{rd} longest lived delayed concentration (cm^{-3})

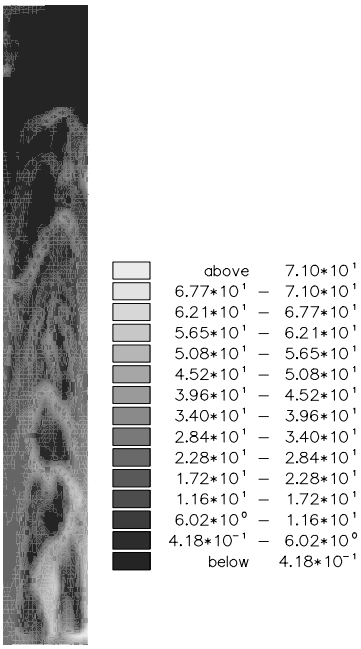

(d) shortest lived delayed concentration (cm^{-3})

Figure 5.8: Various fields at 80 seconds into the simulation with a fine mesh.

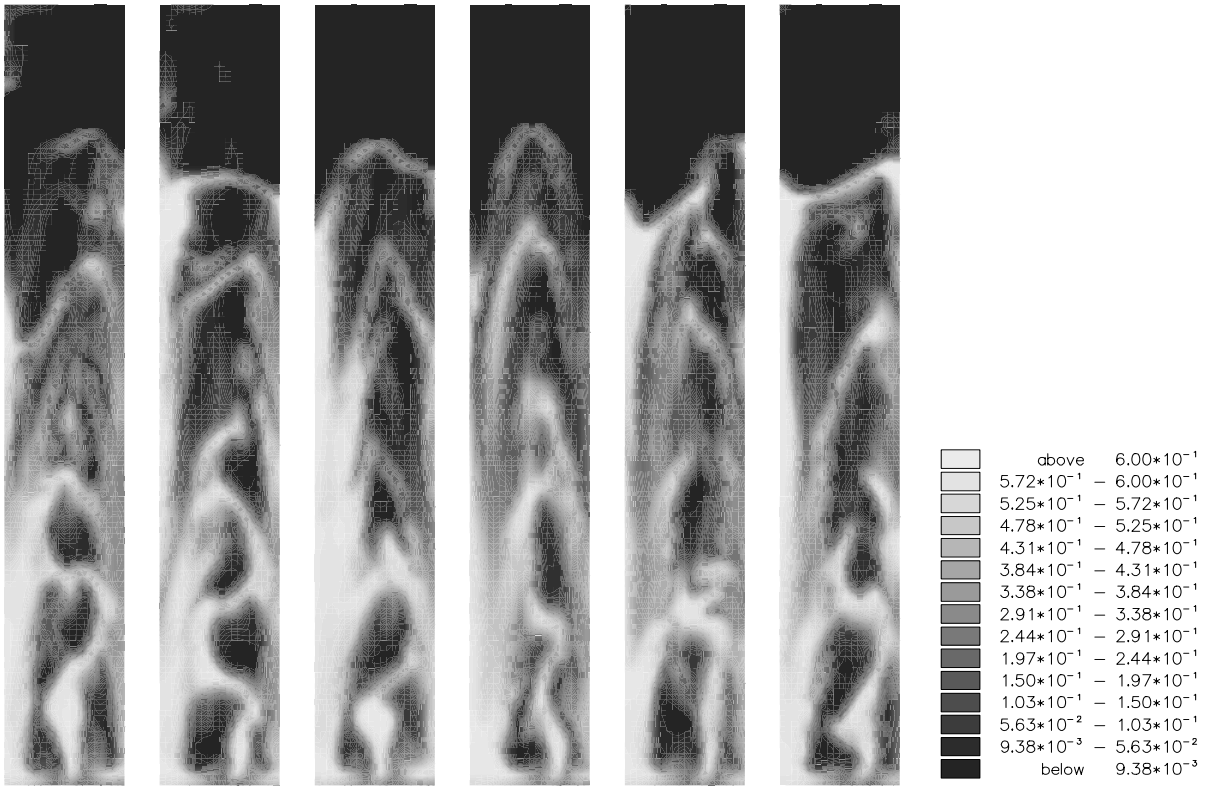

(a)80.0 sec (b)80.5 sec (c)81.0 sec (d)81.5 sec (e)82.0 sec (f)82.5 sec

Figure 5.9: The solid volume fraction at various time levels for the simulation with a fine mesh.

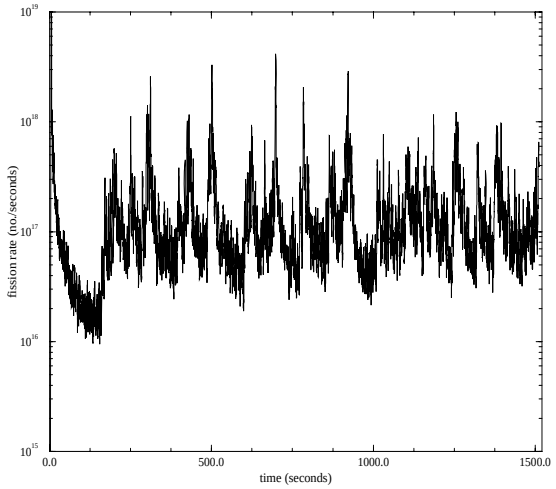

(a) fission rate

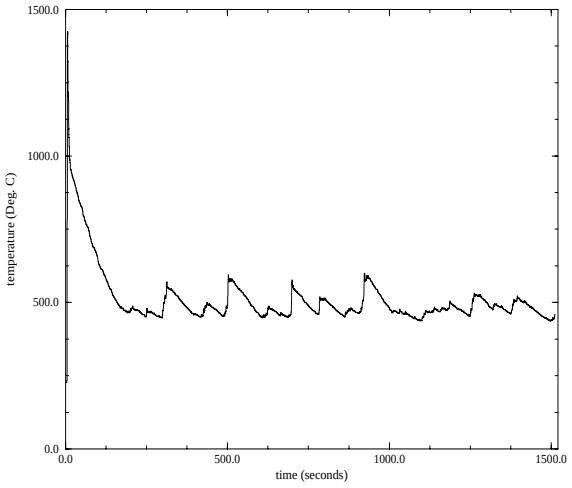

(b) maximum solid temperature

Figure 5.10: The fission rate (a) and maximum solid temperature (b) versus time for the P_1 simulation conducted with a relatively low inlet velocity and in $r - z$ geometry.

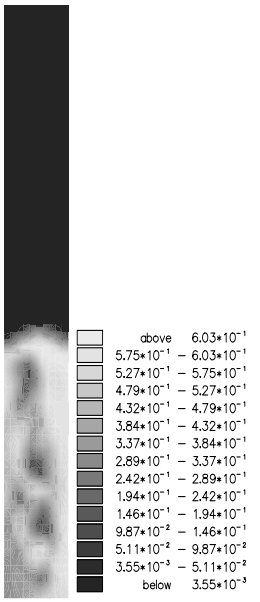

(a) volume fraction

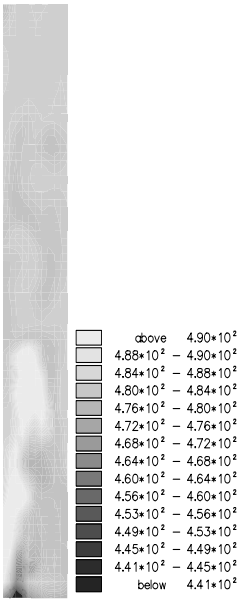

(b) gas Temperature (^{o}C)

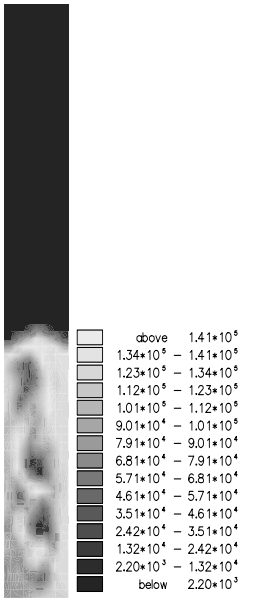

(c) 2^{nd} longest lived delayed concentration (cm^{-3})

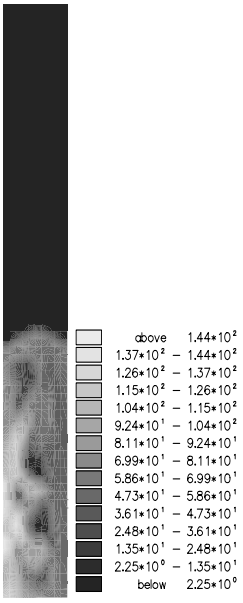

(d) shortest lived delayed concentration (cm^{-3})

Figure 5.11: Various fields at 1260 seconds into the P_1 simulation with a low inlet velocity of 60 $cm.s^{-1}$.

There are some similarities in temperature between this simulation and the simulation conducted at 120 cm/s gas inlet velocity. This means that the quantity of gas heated is half of the simulation conducted with an inlet gas velocity of 120 cm/s. Therefore, the fission rate produced from the simulation with lower inlet gas velocity is approximately half of the simulation performed with a larger inlet gas velocity as shown in Figures 5.10 (a) and 5.12 (a).

To investigate the reactor response to variable inlet velocity and also the reproducibility of this response, a simulation was performed with a sinusoidal varying gas inlet velocity. The period of this oscillation is 720 seconds and has a minimum and maximum velocity of -120 cm/s (outgoing velocity) and 120 cm/s, respectively. The velocity starts from zero and increases to its maximum which occurs at 180 seconds. Figure 5.13 shows the resulting fission rate and maximum temperature versus time for this simulation. Notice that the fission rate starts to increase rapidly at about 50 seconds into the simulation and reaches a peak shortly after this when the inlet gas velocity is about 51 cm/s. Much of the next 150 seconds are taken up by draining the large quantity of heat energy thus deposited out of the system. The fluidizing gas velocity starts to decreases at 180 seconds into the simulation and eventually reaches the stage when it no-longer fluidized the particles. This is seen in the smoothness of the fission rate variation. The fission rate starts to decrease because of the combined effectivity of the negative temperature coefficient and the collapsed bed start (geometry of smallest reactivity). It continues decreasing despite the fact that the negative gas velocity eventually brings cool helium at 220 ^{o} C from above to cool the particles. The particles are sufficiently cooled by this gas that once the gas velocity at the distributor become positive again and the particles fluidized, the fission rate repeats the large peak and in fact will carry on repeating this whole cycle. The 2^{nd} fission peak occurs again at about 50 seconds into the second cycle.

The time averaged solid volume fraction for the four simulations with constant gas inlet velocity is shown in Figure 5.14. Notice that as well as the particle concentration being relatively large at the vertical walls it is also large near the central axis. However, this is not consistent with experimental results observed in similar geometries and with similar particle sizes and densities (see [5]). This discrepancy is probably due to super-

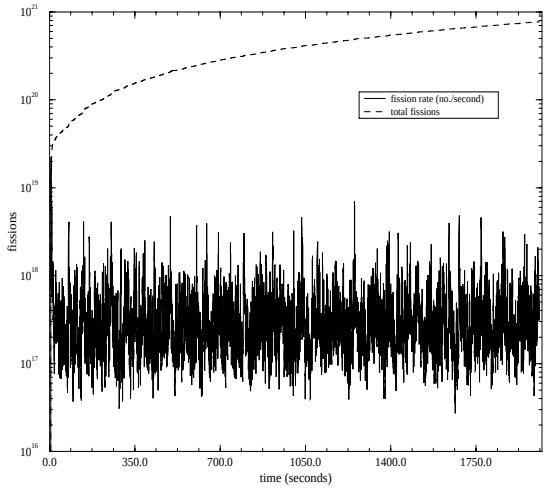

(a) fission rate and accumulative fission

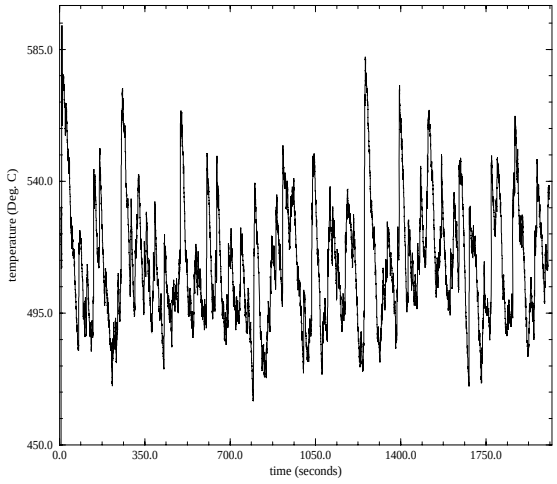

(b) maximum gas temperature

Figure 5.12: The fission rate (a) and maximum gas temperature (b) versus time for the P_1 simulation conducted in $r-z$ geometry with an inlet gas velocity of 120.0 cm.s^{-1}.

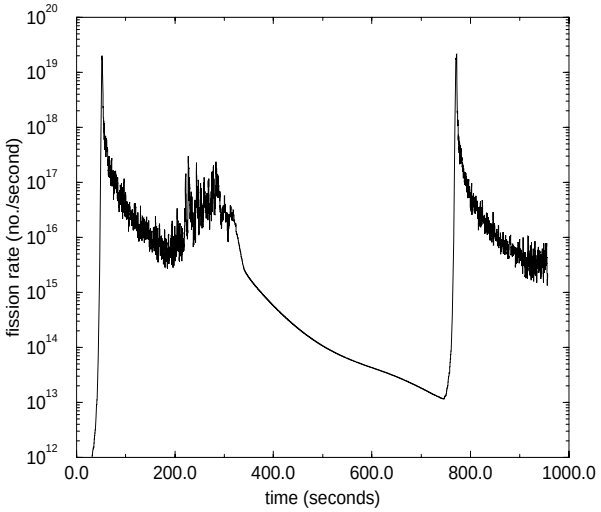

(a) fission rate

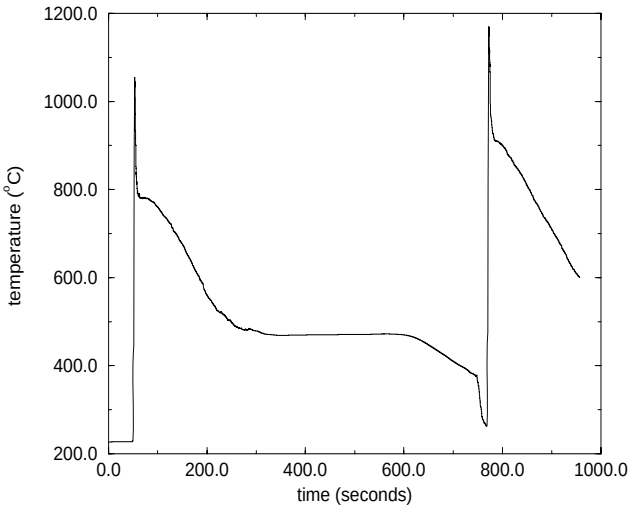

(b) maximum particle temperature

Figure 5.13: Fission rate (a) and maximum particle temperature (b) versus time for the simulation conducted with a sinusoidal inlet velocity and in $r - z$ geometry.